

## ABSTRACT

Title of thesis:      **MECHANISMS OF SEDIMENT  
ENTRAINMENT AND TRANSPORT  
IN ROTORCRAFT BROWNOUT**

Bradley Johnson, Master of Science, 2009

Thesis directed by:   Professor J. Gordon Leishman  
Department of Aerospace Engineering

To advance the understanding of the phenomenon of rotorcraft brownout, a dual-phase flow environment induced by a small-scale rotor hovering above a sediment bed was studied using high-speed flow visualization and particle image velocimetry (PIV). The high frame rate of the camera, combined with advanced particle recognition and tracking software, permitted an understanding of the temporal evolution of the rotor wake in ground effect simultaneously with the processes of sediment entrainment and transport by the rotor flow.

High-resolution near-wall PIV measurements showed that large excursions in the surface boundary layer were produced by the convecting rotor wake vortices. These excursions acted to suppress an equilibrium state in the boundary layer within the zone of vortex impingement on the ground. The highest sediment entrainment levels were observed to occur within this impingement zone, which can be attributed to the increase in groundwash and wall shear produced beneath the vortices. Once entrained, significant quantities of sediment were then trapped and locally suspended by the vortex-induced up-

wash field. This effect resulted in a noticeable level of intermittency in the initial vertical transport of sediment from the ground.

The ground and upwash flow velocities were shown to strengthen significantly during the viscous merging of adjacent wake vortices. This mechanism proved fundamental in defining the concentration of suspended sediment, as well as the maximum height to which sediment could be transported. Sediment particles reaching sufficient heights were observed to recirculate into the rotor wake, and convect back towards the ground at a high speed. This process caused sediment ejection by means of bombardment or “splash.” The classical process of saltation bombardment was also visualized for larger particles whose inertia prevented them from being suspended in the vortical flow. While providing new insight into the time- and length-scales associated with sediment transport by a rotor wake, the observations made here also bring into question the validity of equilibrium particle flux models currently being used for brownout simulations.



Mechanisms of Sediment Entrainment and Transport  
in Rotorcraft Brownout

by

Bradley Johnson

Thesis submitted to the Faculty of the Graduate School of the  
University of Maryland, College Park in partial fulfillment  
of the requirements for the degree of  
Master of Science  
2009

Advisory Committee:  
Professor J. Gordon Leishman, Chair/Advisor  
Associate Professor James Baeder  
Associate Professor Kenneth Kiger

## Acknowledgments

Firstly, I would like to thank my advisor, and thesis committee chairman, Professor J. Gordon Leishman. His passion for research, competitive drive, and work ethic is something I've always admired. I would also like to thank Dr. Manikandan Ramasamy, my friend, and former co-advisor. Without his mentorship, this thesis would not be possible. All of the other great faculty, staff, and students at the University of Maryland have been a joy to work with as well, and I will always cherish my six years worth of memories at Maryland. Special thanks to Anish Sydney, who contributed to the work presented here.

I would also like to acknowledge the contributions of Dr. Tyson Strand of TSI, Inc. for assisting with the experiments and methodology presented in this thesis. The technical comments and suggestions offered by Dr. Kenneth Kiger and Dr. Brian Dade (Dartmouth College) are also much appreciated. I would additionally like to thank the U.S. Air Force Office of Scientific Research, who supported this work under a Multi-Disciplinary University Research Initiative, Grant No. FA9550-08-1-0406. Dr. John Schmisser was the technical monitor. Additional support for my salary was supplied by the National Defense Science and Engineering Graduate (NDSEG) Fellowship Program, sponsored by the Department of Defense (DoD).

Finally, I would like to offer my most sincerest thanks to my parents, Ronald and Vicki, my sisters, Erica and Lindsay, my beautiful girlfriend Jen, and our curious cat, Bruce. Their unconditional love and devotion to me have kept me afloat throughout this entire experience.

# Table of Contents

List of Figures	v
Nomenclature	viii
<b>1 Introduction</b>	<b>1</b>
1.1 Background to the Problem of Brownout . . . . .	1
1.2 Possibilities for Brownout Mitigation . . . . .	3
1.3 Fluid Dynamics of Brownout . . . . .	5
1.4 Principles of Sediment Transport . . . . .	7
1.4.1 Threshold Velocity Criterion . . . . .	8
1.4.2 Sediment Particle Dynamics . . . . .	11
1.4.3 Saltation and Bedload Transport . . . . .	14
1.4.4 Suspension . . . . .	16
1.5 Considerations for Rotor Flows . . . . .	18
1.6 Objective of Thesis . . . . .	21
1.7 Organization of Thesis . . . . .	22
<b>2 Description of the Experiments</b>	<b>23</b>
2.1 Rotor System and Ground Plane . . . . .	23
2.2 Particle Image Velocimetry (PIV) . . . . .	25
2.2.1 Operating Principle of PIV . . . . .	25
2.2.2 Phase-Resolved PIV (PR-PIV) . . . . .	27
2.2.3 PIV Measurements Near Interfaces . . . . .	28
2.2.4 Time-Resolved PIV (TR-PIV) . . . . .	30
2.3 Dual-Phase Experiments . . . . .	31
2.3.1 Dual-Phase PIV . . . . .	34
2.3.2 Particle Recognition and Tracking . . . . .	36
2.3.3 Particle Tracking Uncertainties . . . . .	38
2.4 Summary . . . . .	40
<b>3 Single Phase Flow Measurements</b>	<b>41</b>
3.1 Near-Ground Flow Characteristics . . . . .	41
3.2 Challenges in the Measurement of Wall Shear . . . . .	48
3.3 Vortex Merging . . . . .	54
3.4 Summary . . . . .	57

<b>4</b>	<b>Dual-Phase Flow Measurements</b>	<b>58</b>
4.1	Sediment Entrainment . . . . .	58
4.2	Saltation and Bombardment . . . . .	59
4.3	Sediment Transport in the Rotor Flow . . . . .	63
4.3.1	Sediment Trapping in Vortices . . . . .	64
4.3.2	Sediment Transport by Merging Vortices . . . . .	68
4.4	Consequences for Modeling . . . . .	74
4.5	Summary . . . . .	76
<b>5</b>	<b>Conclusions</b>	<b>78</b>
5.1	Mechanisms of Sediment Entrainment . . . . .	78
5.2	Sediment Transport and Suspension . . . . .	80
5.3	Suggestions for Future Work . . . . .	81
5.3.1	Controlling Flow Aperiodicity . . . . .	81
5.3.2	Improved Dual-Phase Techniques . . . . .	83
5.3.3	Scaling Issues . . . . .	84
<b>A</b>	<b>PIV Measurements Near Interfaces</b>	<b>86</b>
A.1	Techniques to Reduce Laser Reflections . . . . .	86
A.2	Image Processing . . . . .	89
<b>B</b>	<b>Deformation Grid Algorithm</b>	<b>94</b>
	<b>Bibliography</b>	<b>96</b>

## List of Figures

1.1	A helicopter encountering brownout conditions during landing. . . . .	1
1.2	Schematic of the mechanisms of rotorcraft brownout. . . . .	2
1.3	The presence of suspended dust particles around the rotorcraft can obscure the pilots vision. (Courtesy of Dr. Roberto Celi). . . . .	3
1.4	A brownout cloud produced by an EH-101 helicopter. (Courtesy of AWI). . . . .	5
1.5	Forces acting on sediment particles at rest beneath a boundary layer flow. . . . .	9
1.6	Spectrum of forces acting on an airborne sediment particle. . . . .	12
1.7	Schematic showing the fundamental process of the transport of sediment particles through saltation. . . . .	14
1.8	Schematic and smoke flow visualization of a rotor flow during out-of-ground-effect operations. . . . .	19
1.9	Schematic and smoke flow visualization of a rotor flow during in-ground-effect operations. . . . .	20
2.1	Schematic of the experimental setup used in present work. . . . .	24
2.2	Schematic of PIV methodology . . . . .	26
2.3	High-intensity reflections from an interface can mask the flow at the surface and in the boundary layer. . . . .	29
2.4	Microscope images of the particles used for the experiments. (Scale is in units of millimeters.) . . . . .	33
2.5	Phase-discrimination is required to make independent velocity measurements of both the carrier flow and of the sediment. . . . .	35
2.6	Particle objects were identified by connecting neighboring pixels that met the intensity threshold . . . . .	37

3.1	The region of primary interest was focused in a small region at the periphery of the rotor wake as it came into proximity to the ground. . . . .	42
3.2	Measurements of the mean velocity profiles at the ground surface as obtained using PR-PIV. . . . .	43
3.3	High-resolution PR-PIV measurements showed localized regions of boundary layer flow separation on the ground plane ( $\zeta = 600^\circ$ ). . . . .	44
3.4	Schematic of the process of vortex-induced flow separation. . . . .	45
3.5	Time-averaged groundwash profiles compared to instantaneous groundwash profiles produced by a blade tip vortex at $\zeta = 600^\circ$ : (a) profiles below the vortex center, (b) profiles downstream of the vortex center. . . .	46
3.6	Aperiodicity in the flow leads to movements in the spatial locations of the tip vortex cores from rotor revolution to rotor revolution. . . . .	50
3.7	Instantaneous velocity fields produced by the rotor flow, showing significant aperiodicity in the flow. . . . .	51
3.8	Mean flow field obtained through phase-averaging at $\psi = 140^\circ$ . . . . .	52
3.9	Maximum bed erosion occurred in the zone of vortex wake impingement on the ground. . . . .	53
3.10	Sequence of TR-PIV images showing the roll-up of two adjacent vortices	55
3.11	TR-PIV image showing the strong upwash field generated by the merging of adjacent tip vortices: $\psi = 139^\circ$ . . . . .	56
4.1	Schematic of representative saltation paths below the rotor. . . . .	59
4.2	Time-sequence of images showing the process of saltation and saltation bombardment. . . . .	60
4.3	Schematic of representative reingestion paths taken by suspended particles	61
4.4	Time-sequence of images showing the process of reingestion bombardment.	62

4.5	The upwash induced by convecting wake vortices is an important a mechanism for trapping sediment and uplifting it into the rotor flow. . . . .	65
4.6	The upwash induced by the wake vorticity is an important mechanism for vertically transporting and suspending sediment. . . . .	67
4.7	Two adjacent blade tip vortices begin to roll-up . . . . .	70
4.7	(Continued): Roll-up of adjacent vortices, causing sediment trapping . . .	71
4.7	(Concluded): Vertical transport of trapped sediment. . . . .	72
4.8	Larger particles were incapable of reaching equilibrium with the unsteady, vortical flow, causing them to spin out of the vortices. . . . .	73
5.1	One-bladed rotor setup proposed for future work. . . . .	82
5.2	Comparison of masking techniques for carrier phase image processing. . .	84
A.1	Improvement in near-ground PIV interrogation through experimental and image pre-processing techniques. . . . .	87
A.2	Example of a normal correlation map, and one contaminated by laser reflections. . . . .	88
A.3	Improved experimental technique and refined image processing allowed the flow to be successfully measured well into the boundary layer region.	89
A.4	Increasing the aspect ratio of the PIV interrogation window reduces velocity gradient bias errors in the wall-normal direction. . . . .	91
A.5	Vector relocation is required whenever the interrogation windows overlap the interface. . . . .	92
B.1	Schematic showing the basis of the deformation grid technique. . . . .	94

## NOMENCLATURE

$C_D$	drag coefficient
$C_T$	rotor thrust coefficient, $= T / \rho \pi \Omega^2 R^4$
$D$	aerodynamic drag, $kgms^{-2}$
$D_{\text{misc}}$	miscellaneous drag, $kgms^{-2}$
$D_p$	sediment particle diameter, $m$
$D_{\text{Stokes}}$	Stokes drag, $kgms^{-2}$
$f$	empirical function
$F$	dust flux, $kg s^{-1} m^{-1}$
$g$	gravitational constant, $ms^{-2}$
$h_s$	characteristic saltation height, $m$
$i, j, m, n$	integer counters
$I$	pixel greyscale intensity value
$I_d$	dispersed phase image pixel intensities
$I_{\text{thresh}}$	threshold intensity value
$I_p$	inter-particle cohesion forces, $kgms^{-2}$
$k$	von Kármán's constant ( $= 0.4$ )
$K_L, K_D, K_M$	lift, drag, moment coefficients, respectively
$L$	aerodynamic lift, $kgms^{-2}$
$L_M$	Magnus lift, $kgms^{-2}$
$L_s$	characteristic saltation length, $m$
$M$	image magnification
$M_a$	aerodynamic moment, $kgm^2 s^{-2}$
$N$	number of pixels
$Q$	saltation flux, $kg s^{-1} m^{-1}$
$R$	radius of blade, $m$
$T$	rotor thrust, $N$
$U, V, W$	Cartesian flow velocities, $ms^{-1}$



$U_p, V_p, W_p$	Cartesian sediment velocities, $ms^{-1}$
$U_r, V_r, W_r$	relative sediment velocities, $ms^{-1}$
$u_*$	friction velocity, $ms^{-1}$
$u_{*t}$	threshold friction velocity, $ms^{-1}$
$\overline{U'V'}$	Reynolds stress, $m^2s^{-2}$
$V_\theta$	maximum swirl velocity, $ms^{-1}$
$V_{rms}$	root mean squared velocity, $ms^{-1}$
$V_s$	settling velocity, $ms^{-1}$
$V_{tip}$	tip speed of blade, $ms^{-1}$
$W$	sediment particle immersed weight, $N$
$x, y, z$	Cartesian coordinate system, $m, m, m$
$X_c, Y_c$	centroid of sediment particle object, $m, m$
$y_0$	characteristic height, $m$

## Greek Symbols

$\alpha$	empirical function
$\Delta t$	pulse separation time, $s$
$\Delta x, \Delta y$	pixel displacements
$\mu$	dynamic viscosity, $kgm^{-1}s^{-1}$
$\nu$	kinematic viscosity, $m^2s^{-1}$
$\Omega$	rotational frequency of rotor, $radians\ s^{-1}$
$\phi$	cross-correlation coefficient
$\rho$	density, $kgm^{-3}$
$\rho_p$	sediment particle density, $kgm^{-3}$
$\tau_p$	particle time constant, $s$
$\tau_w$	wall shear, $Nm^{-2}$
$\Psi$	Blade azimuth angle, <i>degrees</i>
$\zeta$	vortex wake age, <i>degrees</i>

## **List of Abbreviations**

CCD	charged couple device
CMOS	complementary metal oxide semiconductor
FFT	Fast Fourier Transform
PIV	particle image velocimetry
PR-PIV	phase-resolved particle image velocimetry
TR-PIV	time-resolved particle image velocimetry

## Chapter 1

### Introduction

#### 1.1 Background to the Problem of Brownout

In recent years, the phenomenon of “brownout” has become an increasingly significant problem in rotorcraft flight operations. Brownout is characterized by the formation of a large, and sometimes blinding, dust cloud that is stirred up by a rotorcraft when it tries to land or take off from terrain covered with sand or other loose sediment material; see, for example, Fig. 1.1. The intensity of this dust cloud can result in a severe visual obscuration that can cause the pilot to rapidly lose situational awareness, this phenomenon having contributed to many rotorcraft accidents (Ref. 1).

Brownout is a direct consequence of the rotor aerodynamics near the ground, in that



**Fig. 1.1: A helicopter encountering brownout conditions during landing.**

the pickup, or *entrainment*, of loose sediment particles results from aerodynamic forces imparted on the particles by the induced rotor flow. Once entrained, many of the finer dust particles are uplifted and suspended in the air around the rotorcraft under the action of fluid dynamic forces (see Fig. 1.2). From a pilot's perspective, a sufficiently high concentration of suspended dust around the rotorcraft serves to attenuate the light passing through to the pilot's eyes (see Fig. 1.3). This phenomenon hinders the pilot's ability to identify visual cues on the ground, which can make it hard for the pilot to safely fly the helicopter. Specifically, a significant number of helicopter accidents have occurred during take off and landing maneuvers in the Middle East as a direct result of the pilots suddenly losing situational awareness during encounters with brownout. Many of these mishaps have been reported to occur at night, where the pilot's visibility is inherently restricted further because of the lack of ambient light (Ref. 1).

Brownout also poses several other operational problems other than those directly related to the pilot's visibility. Dust and fine sediment particles can be deposited within various parts in the rotorcraft, including the the swashplate bearings, the engine transmis-

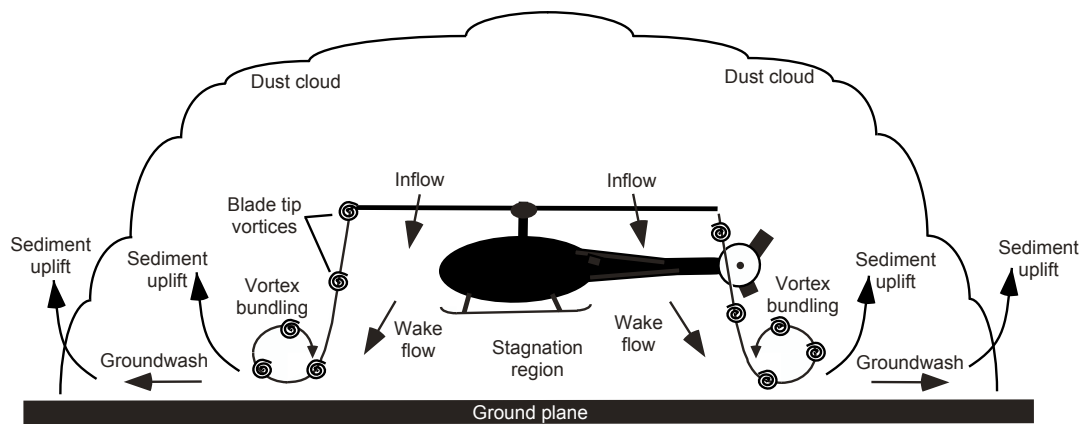


**Fig. 1.2: Schematic of the mechanisms of rotorcraft brownout.**



(a) A pilot's ideal view



(b) Simulated effect of brownout

**Fig. 1.3: The presence of suspended dust particles around the rotorcraft can obscure the pilots vision. (Courtesy of Dr. Roberto Celi).**

sion, and the avionics system. Erosion of the blades by the dust is a very serious problem that can necessitate the replacement of an entire blade set, at considerable cost.

## 1.2 Possibilities for Brownout Mitigation

Within the past few years, new technical efforts have begun to help reduce the piloting risks posed by brownout occurrences. Much work has been focused on the development of avionics systems for the pilot by using sensors and advanced cockpit display technologies. Examples include DARPA's *Sandblaster*, Lockheed Martin's *Pathfinder*, and *PhLASH* by the U.S. Air Force Research Laboratory (Ref. 2). While the mitigation techniques employed by each set of devices vary, the overarching goal of these new systems is to increase the pilot's situational awareness during an encounter with brownout, and so to improve flight safety.

In addition to the use of advanced avionics systems, the development of piloting tactics may also be useful in reducing the severity of brownout, and in controlling the

rapidity at which the dust cloud develops. However, these piloting tactics may not be unique (or even safe), and will depend at least partly on the type of sediment and non-erodible surface elements that are present on the ground. The needed tactics to mitigate brownout occurrences may also differ considerably between different rotorcraft types, i.e., they may be different for single rotor helicopters versus tandem rotor helicopters, helicopters versus tiltrotors, etc.

While advanced avionics systems and piloting techniques may serve as short-term solutions to the brownout problem, ultimately a more permanent solution is desired. This goal may require actual design changes to the rotorcraft itself. Based on anecdotal evidence, it is known that intensity and spatial extent of a developing dust cloud can be very different for different rotorcraft. Figure 1.4, for example, shows an a dust cloud produced by a landing EH-101 helicopter. While there is a significant amount of dust suspension, the largest dust concentrations can be observed to form in a toroidal region on the periphery of the rotor disk, with little dust suspension near the actual landing zone of the helicopter.

Evidence that the brownout signature of some rotorcraft are less severe than others suggests that there may be certain (perhaps unique) rotor design variables that influence the severity and extent of brownout. Because the entrainment and suspension of dust is a consequence of the aerodynamics of the rotorcraft when in ground effect, it can be expected that any design feature that alters the nature of the induced flow below the rotor will play some role in determining the brownout signature. These aerodynamic design features may include (but are not limited to): rotor disk loading, blade loading, tip speed, blade twist, number of blades, tip shape, number of rotors, etc.



**Fig. 1.4: A brownout cloud produced by an EH-101 helicopter. (Courtesy of AWI).**

### 1.3 Fluid Dynamics of Brownout

Assessing the potential of certain design parameters for brownout mitigation requires an ability to understand and predict how such parameters may contribute to the development of the brownout dust cloud itself. Achieving this understanding requires addressing the true causes of brownout, which have their source in the field of multiphase fluid dynamics. This is because two separate phases of matter contribute to the problem of brownout: 1) *The carrier phase*, which is represented by the three-dimensional, unsteady flow induced by a rotorcraft operating in ground effect; 2) *The dispersed phase*, which is represented by the non-uniform concentrations of sediment particles lofted into the rotor flow. This multiphase aspect drastically increases the complexity of measuring, understanding, and modeling brownout because the sediment and carrier fluid are intrinsically coupled and are capable of transferring momentum and energy to and from each other.

From a fluid mechanics measurements perspective, there are clearly many challenging issues involved in understanding such problems, some of which are discussed in the present thesis. From a modeling perspective, the issues are equally daunting in that computing the uplift of the sediment and the subsequent motion of each and every residual dust particle dispersed in the flow is far beyond present computing capabilities (Ref. 3).

Despite this hurdle, attempts at simulating brownout cloud formations have already been undertaken (Refs. 4–7), each simulation invoking various simplifications and assumptions for calculating the development of the dust clouds. The most common approach up until this point has been to solve for the induced velocity field at the ground with some combination of a rotor wake and boundary layer model, and then to use semi-empirical particle flux models to represent the initial mass fluxes of sediment being entrained into the rotor flow field (see Section 1.4). This approach generally requires three types of assumptions: Type 1: Those made to simplify the modeling of the rotor flow field during ground effect operations; Type 2: Those made to simplify the modeling of the sediment entrainment into the rotor flow field; and Type 3: Those made to simplify the modeling of the momentum exchange between the multiple phases of the combined flow (i.e., dilute or one-way coupling)

While most of the assumptions used for rotor wake models (i.e., those of Type 1) have been well studied and validated, the models being used for the entrainment and transport of sediment (i.e., Types 2 and 3) are inadequately validated for brownout problems. This is because the majority of models used for airborne sediment entrainment and transport are empirical in nature, and are derived from experiments of sediment transport in simple flows (i.e., steady, one-dimensional flows). The use of these models is question-



able for the non-uniform, unsteady, three-dimensional flows generated by rotors operating near the ground. Consequently, current brownout models must be considered only on a conditional basis, and must be subject to much further examination as more detailed measurements of the problem begin to be obtained. Such data must be collected from several sources, including laboratory tests on sub-scale rotors and from field measurements made on actual helicopters encountering brownout conditions.

## 1.4 Principles of Sediment Transport

Understanding (and eventually predicting) the characteristics of the dust clouds formed during brownout conditions first requires a knowledge of sediment transport physics. Sediment transport is a large research area in itself, with two main focuses being wind-driven particle transport (i.e., wind-erosion) and hydrodynamic particle transport, which focuses on sediment entrainment and transport in coastal environments. On one hand, *entrainment* specifically describes the process(es) associated with the actual pickup of stationary sediment particles from a sediment bed by a carrier flow. *Transport*, on the other hand, describes the dynamics of the dispersed particles after they are entrained into the flow.

Sediment entrainment and transport inherently have different time- and length-scales of interest. *Micro-scale* studies, which focus on individual particle dynamics in a multiphase flow (including collisions), have been carried out (Ref. 9). However, these are extremely computationally expensive, and are unrealistic to use for an entire brownout simulation at this point. Because of the difficulty and expense of modeling particle dy-

namics at the micro-scale, classical sediment transport mechanisms tend to be represented by *meso-scale* models. In this case, the dispersed phase of particles in the flow is treated in a continuous manner, such that the overall evolution of the dispersed phase is modeled as an ensemble-average of the individual particle dynamics.

Most classical meso-scale models of sediment entrainment and transport are based on the extraction of correlation coefficients from experiments of specific flows passing over sand and/or soil beds of certain known (or estimated) characteristics (Refs. 10–25). Of specific interest is the mass flux and concentration of sediment that can be entrained into the external flow, and how to model such processes as a function of the shearing action exerted by the flow on the sediment bed.

#### 1.4.1 Threshold Velocity Criterion

The entrainment of sediment into a flow from an underlying sediment bed depends upon the fluid dynamic forces exerted on the bed by the carrier flow. Once these forces become sufficiently high, particles can be entrained into the flow itself. Bagnold (Ref. 10) observed that the significant mobilization of loose sand particles on a sediment bed only occurs when the surface flow velocity reaches a critical or a “threshold” value. At this point, particles begin jumping along the ground in the direction of the flow in a phenomenon called *saltation*. Below this threshold velocity, no particle flux occurs unless an auxiliary force other than the steady wind disturbs the sediment bed. Therefore, the mass flux of particles entrained from a sediment bed tends to be a non-linear discontinuous function of flow velocity, the discontinuity existing at the threshold velocity at which

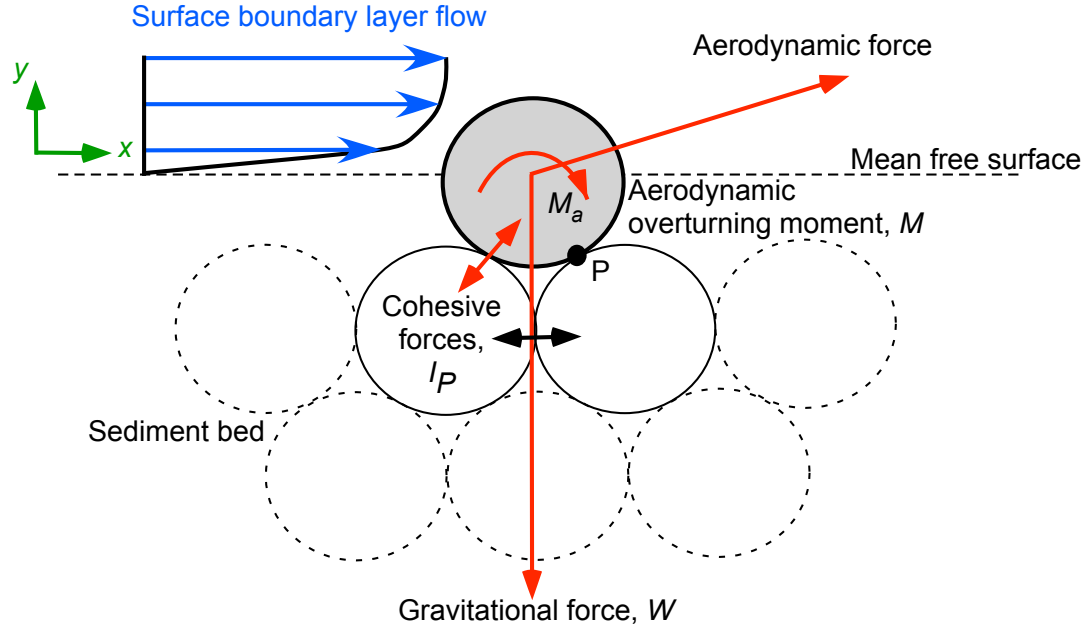


**Fig. 1.5: Forces acting on sediment particles at rest beneath a boundary layer flow.**

the particle flux originates. The correct identification of the threshold conditions at which particles are mobilized, therefore, plays a critical role in correctly predicting the onset of any flow-driven particle mobilization process, including the problem of brownout.

Understanding the physics behind this threshold condition requires an examination of the forces acting upon free particles lying on a flat bed below an external flow. This situation is shown in Fig. 1.5, which is adapted from Refs. 11 and 12. Acting downward through the center of gravity is the immersed weight of the particle  $W$  (true weight minus buoyancy), while the aerodynamic force (which can be resolved into a lift and drag force) is produced by the action of the boundary layer flow. An aerodynamic moment,  $M$ , may also exist if the center of pressure of the particle does not align with its geometric center, such as would be typical of using non-spherical particles. The inter-particle cohesive forces,  $I_P$ , are more difficult to define, and comprise a combination of electrostatic charge, humidity, surface shape, particle size, and van der Waals forces (Refs. 11–13).

Because the sediment bed lies in and/or below a surface boundary layer, the normal approach in modeling the aerodynamic forces is by using an equivalent wall shear,  $\tau_w$ . For airborne wind-erosion studies (which have formed the basis for early brownout cloud simulations), a fully-turbulent equilibrium boundary layer model is usually implemented to calculate the wall shear from the external wind velocity. In this case, the boundary layer is characterized by a roughness height  $y_0$  (associated with the roughness effects of the sediment bed), and a mean velocity  $U(y)$  that can be expressed as

$$U(y) = \frac{u_*}{k} \ln \left( \frac{y}{y_0} \right) \quad (1.1)$$

where  $k$  is von Kármán's constant. The  $u_*$  term is called the friction velocity, which is proportional to the velocity gradient, and is defined by

$$u_* = \sqrt{\frac{\tau_w}{\rho}} \quad (1.2)$$

where  $\tau_w$  is the surface, or wall, shear and  $\rho$  is the density of the flow. The aerodynamic forces (lift and drag) and the overturning moment can then be correlated empirically to the size (diameter) of the particle and to the friction velocity (Refs.11 and 12), i.e.,

$$D = K_D \rho u_*^2 D_p^2 = K_d \tau_w D_p^2 \quad (1.3)$$

$$L = K_L \rho u_*^2 D_p^2 = K_d \tau_w D_p^2 \quad (1.4)$$

$$M_a = K_M \rho u_*^2 D_p^3 = K_d \tau_w D_p^3 \quad (1.5)$$

where  $D_p$  is the particle diameter and  $K_L$ ,  $K_D$ , and  $K_M$  are dimensionless lift, drag, and moment coefficients. Therefore, the higher the friction velocity  $u_*$  (or equivalently, the larger  $\tau_w$  is) for a given distribution of bed particles, the larger the aerodynamic forces and moments acting on the particles.

Referring back to Fig. 1.5, it is apparent that the resultant aerodynamic forces will tend to roll the particles about point P in the direction of the flow, so causing their movement along the sediment bed. There will exist some threshold friction velocity  $u_{*f}$  at which the aerodynamic forces are exactly in balance with the combined gravitational and cohesive forces. Any increase in the friction velocity  $u_*$  beyond  $u_{*f}$  will cause the particles to become mobilized. Notice that an increase in  $u_*$  can result from either an increase in the external flow velocity above the boundary layer or by a change in the boundary layer profile itself. As an outcome of experimental observations of these initiation processes, several semi-empirical threshold models have been developed for different types of sediment (Refs. 11-19). These models, however, may not be entirely applicable for modeling the problems of brownout. This is because they were not derived to account for the complex non-equilibrium conditions developed in the boundary layer that are produced by the vortical, unsteady nature of the rotor flow (as discussed in Chapter 3).

#### 1.4.2 Sediment Particle Dynamics

Once the threshold condition has been met, the sediment particles follow trajectories based upon the relative magnitude of the forces acting upon them. This effect is shown in Fig. 1.6, which shows a representative set of forces acting on an immersed particle in an inertial frame of reference. Two significant parameters are the immersed weight,  $W$ , and the fluid dynamic drag,  $D$ , the latter which can be modeled as a combination of a Stokes drag,  $D_{\text{Stokes}}$ , plus a miscellaneous drag,  $D_{\text{misc}}$ . The latter force results from the (typically) non-spherical shape of the sediment particles. While the miscellaneous drag

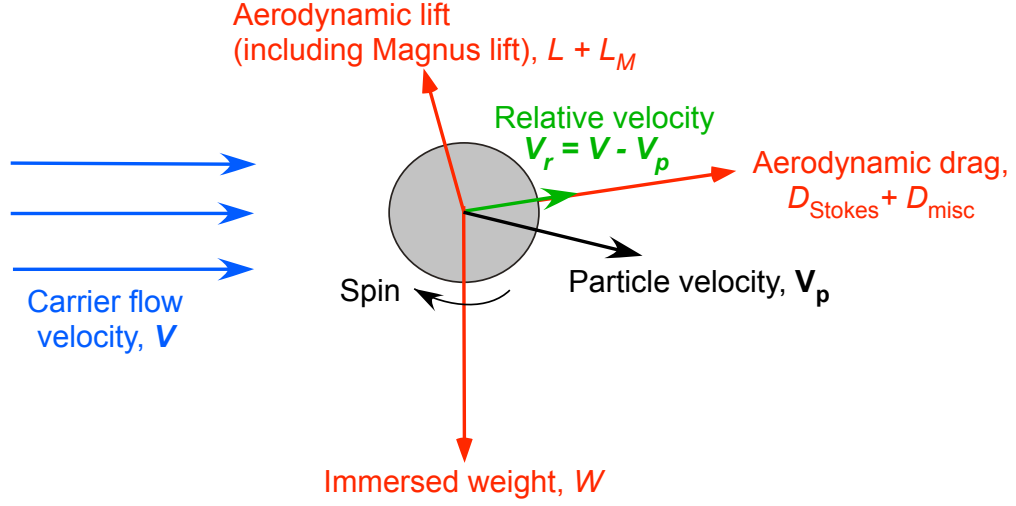


**Fig. 1.6: Spectrum of forces acting on an airborne sediment particle.**

will vary for different particle geometries, the Stokes drag of a small spherical particle is well established. In this case, the drag coefficient,  $C_D$ , is given by

$$C_D = \frac{24}{Re_p} \quad (1.6)$$

where the particle Reynolds number  $Re_p$  is given as a function of the kinematic viscosity of the fluid,  $\nu$ , the particle diameter  $D_p$ , and the magnitude of the relative velocity (or *slip velocity*) of the particle with respect to the carrier flow,  $|\mathbf{V}_r|$ , i.e.,

$$Re_p = \frac{D_p |\mathbf{V}_r|}{\nu} = \frac{D_p |\mathbf{V} - \mathbf{V}_p|}{\nu} \quad (1.7)$$

where

$$|\mathbf{V} - \mathbf{V}_p| = \sqrt{(U - U_p)^2 + (V - V_p)^2 + (W - W_p)^2} \quad (1.8)$$

with  $(U, V, W)$  being the carrier flow velocity, and  $(U_p, V_p, W_p)$  being the sediment particle velocity. It should be noted that the Stokes drag (i.e., Eq. 1.6) is valid for  $Re_p \ll 1$  (i.e.,

creeping flow). For  $Re_p \geq 1$ , an empirical correction to Eq. 1.6 can be used (Ref. 9), i.e.,

$$C_D = \frac{24}{Re_p} \left( 1 + 0.15 Re_p^{0.687} \right) \quad (1.9)$$

In addition to particle weight and drag, other possible forces acting on an isolated particle in a carrier flow include a lift force, which acts in a direction normal to the slip velocity  $\mathbf{V}_r$  of the particle. Lift forces can originate from non-spherical shape profile of the particles, or from high shear in the flow (i.e., the Saffman lift force—see Ref. 20). An additional Magnus lift force,  $L_M$ , can be created if the particle has acquired any angular spin. Other (but smaller) forces may be present, including apparent mass and Basset forces (i.e., viscous lag), and external forces and moments arising from pressure and shear stress gradients in the flow acting over the particle surface (Ref. 21).

For spherical particles which possess a sufficiently high density compared to the carrier flow (i.e.,  $\rho_p/\rho > 1000$ ), most of the preceding forces are of smaller importance than the particle's weight and drag (Ref. 21), and a dispersed particles equation of motion can be simplified to

$$\frac{d\mathbf{V}_p}{dt} = \frac{1}{\tau_p} \mathbf{V}_r + g \quad (1.10)$$

where  $\tau_p$  is a the particle's response time as given by

$$\tau_p = \frac{\rho_p}{\rho} \frac{D_p^2}{18\nu} \quad (1.11)$$

Equation 1.11 is derived for Stokes drag assumptions (i.e., using Eq. 1.6). Physically,  $\tau_p$  is the characteristic time scale needed for a given particle to adjust to a change in the carrier flow velocity.

### 1.4.3 Saltation and Bedload Transport

For airborne transport by atmospheric winds in arid or desert environments (the environment in which brownouts occur), the gravitational force (right term in Eq. 1.10) is the dominant force for most particles over  $50\ \mu\text{m}$  in diameter (Ref. 11). This class of particles can generally be referred to as *sand*. Because of the weight of these large particles, they typically cannot remain airborne for much time, nor can they reach substantial heights above the sediment bed. Because of this behavior, such particles are described as *bedload*.

For airborne transport, the characteristic transport mechanism of bedload particles is saltation, in which sediment particles follow smooth, ballistic-like trajectories in a layer just above the sediment bed (see Fig. 1.7). This layer is known as the saltation layer (Refs. 10 and 22). Many of the uplifted particles quickly fall back to the ground under gravity, and so collide with the bed and cause other particles to be set into motion and so forth. Therefore, saltation can be viewed as a cascading process, with a perpetual transfer of energy between the fluid and the particles and between the free particles and the sediment bed.

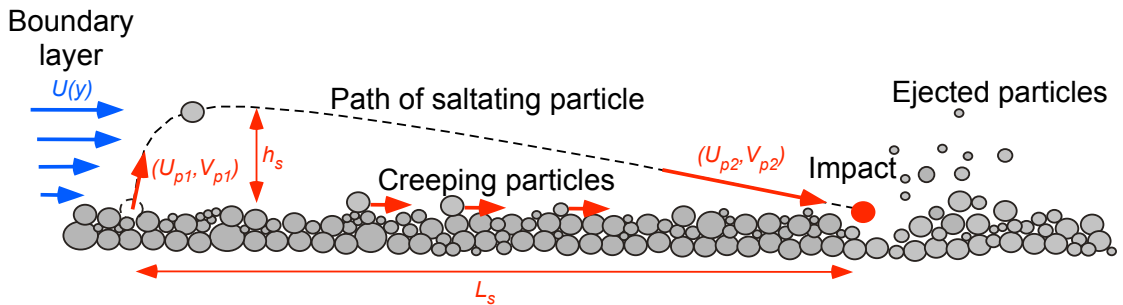


**Fig. 1.7: Schematic showing the fundamental process of the transport of sediment particles through saltation.**



The dynamics of sediment particles within the saltation layer have several dependencies, which will involve stochastic collision dynamics. Generally, saltating particles are known to rise up nearly vertically from the bed after the threshold conditions are reached, acquiring a vertical velocity  $V_{p1}$  and streamwise velocity  $U_{p1}$ —see Fig. 1.7. The particles then follow ballistic-like parabolic trajectories with maximum height  $h_s$  and characteristic length  $L_s$ , which in practice may range between a few millimeters to over a meter. Because the particles gain momentum from the external flow during the saltation process, the resultant velocity at impact is larger than the initial velocity, meaning that the particles impact the bed at a higher energy state compared to when they were first entrained. Particles too heavy to be lofted into the flow in saltation simply roll along the surface in a state called *surface creep* (Ref. 10).

For uniform flows with boundary layers in an equilibrium state (i.e., Eq. 1.1), there eventually also exists an equilibrium between the mass flux of particles in saltation above the bed  $Q$  and the mean shear stress (or friction velocity  $u_*$ ) acting on the bed. Therefore, models for  $Q$  are generally derived as a function of the friction velocity  $u_*$  and the ratio  $u_*/u_{*t}$ , i.e., using an equation of the form

$$Q = f\left(u_*^m, \left(\frac{u_*}{u_{*t}}\right)^n\right) \quad (1.12)$$

where  $m$  and  $n$  are empirical correlation coefficients derived from fitting experimental measurements of  $Q$  with measurements of  $u_{*t}$  and  $u_*$ —see Greeley & Iversen (Ref. 11).

#### 1.4.4 Suspension

Although particles in saltation will not reach sufficient heights to directly impede the pilot's vision in a brownout condition, one consequence of saltation is the emission of finer particles or *dust*, which are capable of being carried to sufficient heights by the flow. Like all types of particulates, both aerodynamic forces and the impact forces produced by saltating particles can eject dust. However, because of their smaller size, dust particles possess stronger cohesive forces, making the aerodynamic threshold friction velocities for dust relatively higher compared to bigger particulate materials (Refs. 11, 15, 23). Therefore, in addition to the aerodynamic forces, dust production depends in part on the forces supplied by impacting sediment in saltation to break the cohesive bonds between them, a process known as saltation bombardment (Refs. 23 and 24).

Unlike larger sediment particles, which generally possess sufficient mass to fall back to the ground under gravity during the process of saltation, the smaller dust particles are more prone to suspension given their smaller mass and relatively higher viscous drag (see Eq. 1.6). Suspension specifically occurs if the vertical drag on the particle is greater than its immersed weight, allowing the particle to be suspended even under gravitational forces. Particles capable of being suspended once entrained have sometimes been referred to as *wash load* (Ref. 25).

For uniform one-dimensional flows (similar to atmospheric winds), the primary form of vertical velocity transmitted to airborne particles results from turbulent eddies. Therefore, particle suspension through atmospheric winds occurs whenever the vertical component of turbulent velocity  $V_{\text{rms}}$  is greater than or equal to the settling velocity  $V_s$  of

the particle, i.e., when

$$V_{\text{rms}} > V_s = \sqrt{\frac{4\rho_p g D_p}{3\rho C_D}} \quad (1.13)$$

where the settling velocity is simply the vertical descent velocity of the particle needed for its vertical drag to balance its immersed weight (Refs. 10 and 11).

The concept of sediment suspension is fundamental to the development of the brownout dust cloud. If a particle is small enough to be suspended in a coherent structure in the rotor flow (such as in a blade tip vortex), then it can be convected with the flow structure, and it may possibly reach substantial heights above the ground and loiter there for a significant time. The spatial concentration of these suspended particles is an important parameter governing the problem of brownout because it has direct consequences on optical transmissibility, and so in the resulting visibility through the dust cloud from the pilot's perspective (i.e, as shown previously in Fig. 1.3).

Concentration levels of dust depend greatly upon the mass flux of particles entrained from the surface, which vary with both the characteristics of the flow and with the particles themselves. For airborne sediment transport, the majority of flux models were derived to model the long-distance transport of tiny dust particles by atmospheric winds, and as such were measurements of particle flux in steady one-dimensional winds (much like the classic threshold models). Because the suspension of dust particles depends upon saltation bombardment as an intermediate process (at least for natural winds), the dust emission,  $F$ , for these simple flows have been derived as a function of the mass flux of particles in saltation, i.e., by using an equation of the form

$$F = \alpha Q \quad (1.14)$$

where  $\alpha$  is an empirically derived function (Ref. 23). Several attempts have been made to derive expressions for  $F$  in relatively simple terms for appropriate ranges of particle sizes (Refs. 23–30). However, the process is highly empirical, and depends on the ability to perform certain types of idealized experiments with dual-phase flows.

## 1.5 Considerations for Rotor Flows

Although the foregoing processes govern the behavior of several types of sediment transport, they are not all inclusive. Entrainment and suspension occur in a wide variety of flows. The spatial and temporal concentrations of entrained and suspended sediment additionally will vary, depending on the nature of the carrier flow itself. Thus, sediment entrainment and transport in brownout inherently requires a knowledge of the flow field produced by the rotor in proximity to the ground. Currently, however, many brownout simulations have employed rather simplistic sediment entrainment and transport models, which have been derived mainly from wind-erosion theory (i.e., Eqs. 1.1, 1.12, and 1.14). These models are geared towards sediment transport in steady, uniform flows.

The flow induced by a rotor near the ground, however, is much more complex. This is predominately because of the presence of the helicoidal blade tip vortex filaments, which are formed around the rotor blade tips, and convect with the induced flow of the rotor wake. For hovering conditions well above the ground (out-of-ground-effect), the induced flow below the rotor contacts, and the vortices eventually diffuse into a turbulent jet further below the rotor disk (see schematic and smoke flow visualization image in Fig. 1.8).

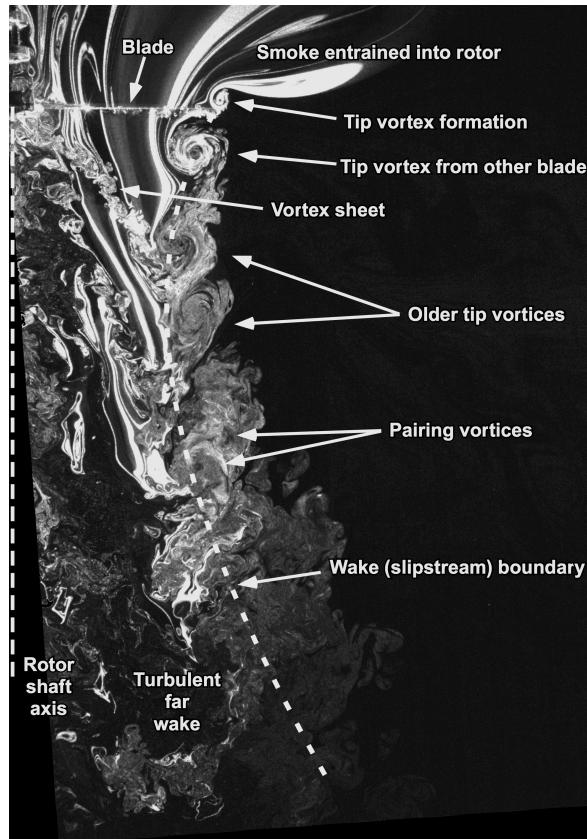
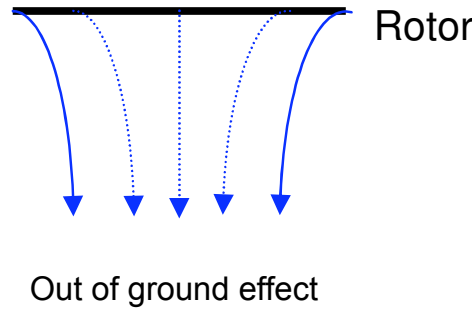


**Fig. 1.8: Schematic and smoke flow visualization of a rotor flow during out-of-ground-effect operations.**

When the rotor is operating in-ground-effect, which corresponds to an operating state where the rotor is less than four rotor diameters above the ground (Ref. 31), the flow state is very different. Because the ground must be a streamline of the flow, the rotor flow expands radially, which results in the vortices impinging upon the ground and convecting

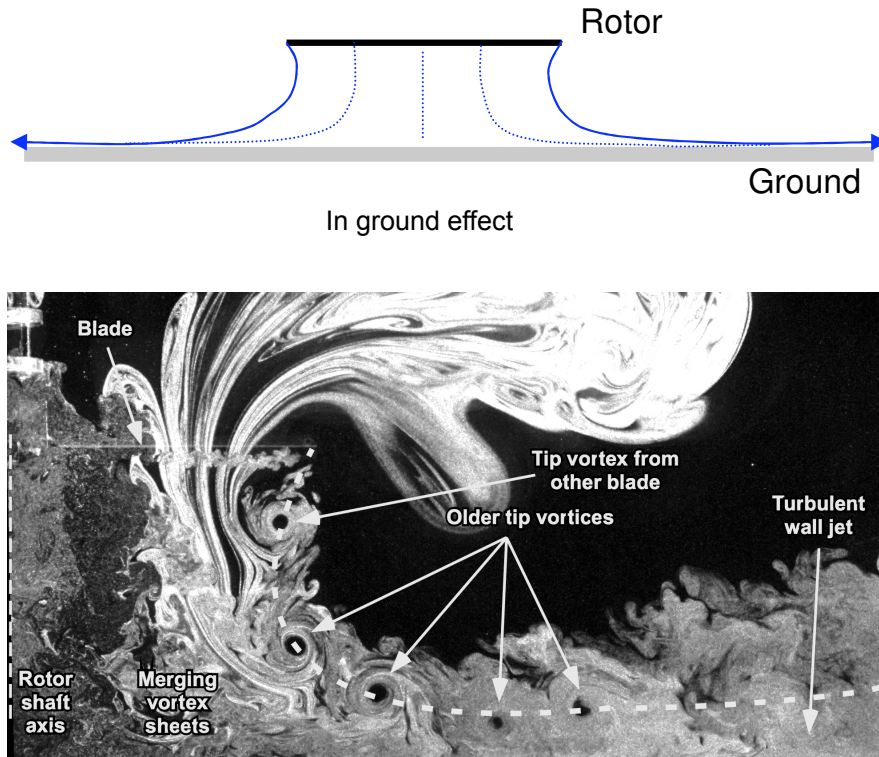


**Fig. 1.9: Schematic and smoke flow visualization of a rotor flow during in-ground-effect operations.**

roughly parallel to the surface (see Fig. 1.9, adapted from Ref. 32). During this process, the filaments themselves undergo a stretching process (Ref. 33 and 34), which results in vorticity intensification that counters the normal diffusive spin down of the vortices under the action of viscosity and turbulence. Because the vortices are persistent near the ground, the flow is highly unsteady, and three-dimensional.

Unsteady effects like these are known to play a substantial role in sediment transport processes, especially in the development of the boundary layer. Such effects have been studied in coastal sediment transport by oscillatory ocean wave patterns (Ref. 25). Unlike in a steady uniform flow, where an equilibrium exists between the shear stress on the ground and the resultant mass flux and concentration of particles entrained above the

surface (i.e.,  $Q$  and  $F$ ), no such local equilibrium exists in an unsteady or non-uniform flow (Ref. 25). This result has important consequences for the modeling of sediment entrainment in brownout conditions, bearing in mind that the flow field of a rotor operating in ground effect is not only three-dimensional, but also highly unsteady and non-uniform with embedded vortical flows.

## 1.6 Objective of Thesis

The goal of the present work was to help improve the fundamental understanding of the physics governing the entrainment and transport of sediment in non-uniform, unsteady flows, characteristic of those produced by rotors in ground effect and encountering brownout conditions. In fact, apart from one previous laboratory experiment (Ref. 8), very little physical understanding has been obtained about the mechanisms that govern sediment entrainment and transport by rotor flows. Therefore, the foundational understanding of the fluid dynamics of brownout currently relies heavily on experimental measurements and empirical observations.

To provide a first principles understanding of the physics of sediment entrainment and transport in brownout, a series of detailed experiments were performed with a small two-bladed rotor system that was operated in hover above a ground plane. Different particle species were distributed on the ground plane to simulate a sediment bed below the rotor. Laser sheet illumination and imaging of the flow using a high-speed digital camera allowed for both dual-phase flow visualization and time-resolved dual-phase particle image velocimetry (PIV) measurements of the rotor wake flow and the processes of sediment

entrainment. The use of advanced particle recognition and tracking algorithms allowed for separate measurements of the flow and sediment velocities. High-resolution phase-resolved PIV additionally allowed for a study of the developing wall jet and unsteady boundary layer formed by the rotor flow. The results obtained contribute to the understanding of the fluid dynamics and sediment transport mechanisms that are responsible for the development of brownout conditions.

## 1.7 Organization of Thesis

The work presented in the present thesis is a synthesis of two separate fields of research: 1) Sediment transport, 2) Rotor aerodynamics in-ground-effect. A fundamental understanding of both fields is required for any brownout mitigation strategy to be successfully implemented. A background to the brownout problem has been presented in the present chapter, along with a review of the principles of sediment transport and the challenges of understanding sediment transport in rotor flows. Chapter 2 provides a detailed explanation of the experimental techniques that were used to investigate the rotor flow field in-ground-effect, simultaneously with the process of sediment entrainment and transport by the rotor flow. These techniques were centered around the application of various forms of particle image velocimetry (PIV) and flow visualization. Chapters 3 and 4 discuss the results in terms of single-phase flow velocity measurements of just the rotor flow, and dual-phase flow visualization and velocity measurements of the combined air-sediment environment near the ground, respectively. Finally, Chapter 5 discusses the conclusion of the present work, and suggests directions for future experimental research.



## Chapter 2

### Description of the Experiments

To better understand the sediment entrainment and transport processes below a rotor, multiple experiments were carried out to explore the both the single-phase (i.e., no sediment), and the dual-phase (i.e., carrier and sediment) flow environment induced by a rotor hovering near the ground. This chapter gives an overview of the experimental setup, along with the flow interrogation techniques used in the present study. The experiments allowed for both qualitative and quantitative understanding of the nature of sediment entrainment and transport below a hovering rotor.

#### 2.1 Rotor System and Ground Plane

A small, two-bladed rotor with a radius of 86 mm was used in the present study. The rotor was set up in hover, centered at one rotor-radius above a horizontal ground plane (see Fig. 2.1). The plane extended twelve rotor radii radially outwards from the extended centerline of the rotor. The reference coordinate system was placed at the center of the ground plane, directly below the rotor.

The rotor was operated at a nominal rotational speed of 50 Hz, which produced a chord Reynolds number at the tip of about 35,000. The blades used a circular arc cambered airfoil, which has been proven to be more aerodynamically efficient for operations at these lower blade chord Reynolds numbers (Ref. 35). Under these conditions,

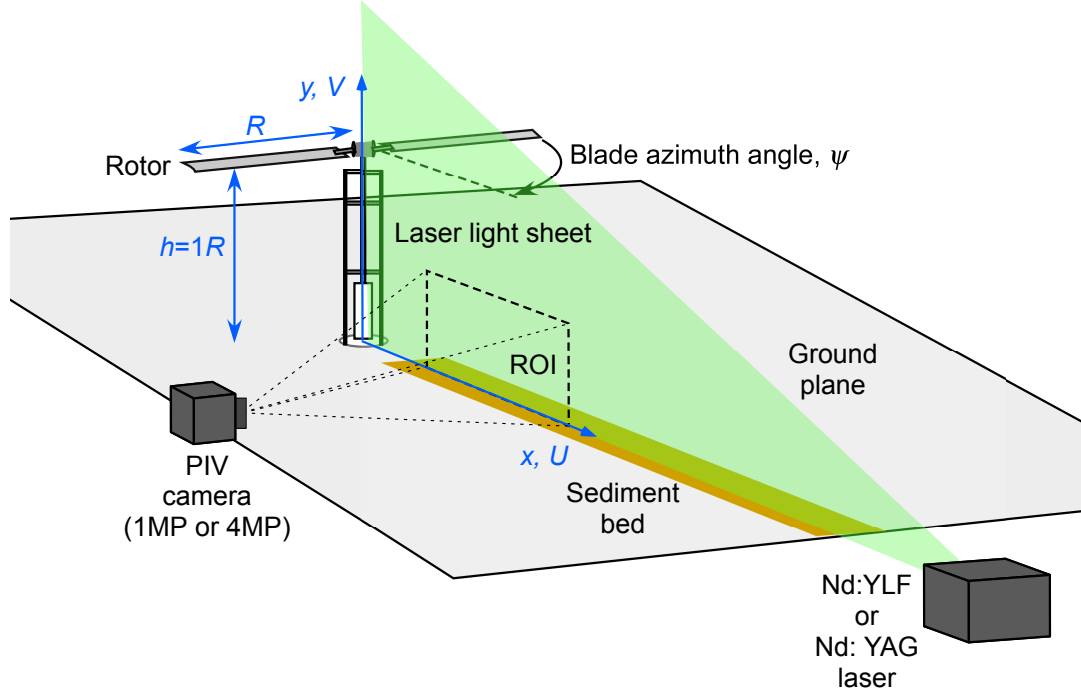


**Fig. 2.1: Schematic of the experimental setup used in present work.**

the rotor operated at a thrust coefficient  $C_T$  of  $0.016 \pm 0.001$  and a blade loading coefficient  $C_T/\sigma$  of 0.11. (in-ground-effect) when measured using a micro-balance. Despite the lower chord Reynolds numbers, the structure and temporal growth properties of the blade tip vortices at these low vortex Reynolds numbers are actually very similar to those found at higher vortex Reynolds numbers (Refs. 35 and 36).

In the two-phase experiments, a sediment bed approximately 1 cm in thickness was formed in a small quadrant on the ground plane along the centerline plane of the rotor. A laser light sheet was oriented to be co-planar with the bed, and was used for illumination of the flow for both PIV (see Section 2.2) and flow visualization. A digital camera was aligned orthogonal to the laser light sheet, and was uniformly focused to a small flow region of interest (ROI) near the ground to image the flow—see Fig. 2.1. A charged coupled device (CCD) camera was used in phase-resolved PIV experiments,

while a high-speed complementary metal oxide semiconductor (CMOS) camera was used for time-resolved PIV experiments.

## 2.2 Particle Image Velocimetry (PIV)

Variations of the particle image velocimetry (PIV) measurement technique were used to quantitatively study the flow environment below the rotor. Both phase-resolved PIV (PR-PIV) and time-resolved PIV (TR-PIV) techniques were used, both of which are detailed in the following sections. Flow visualization was also performed on the dual-phase environment beneath the rotor when using various sediment particle species. Finally, some initial dual-phase PIV measurements were performed with the help of advanced particle recognition and particle tracking software.

### 2.2.1 Operating Principle of PIV

PIV is a non-invasive flow measurement technique in which whole-field velocity measurements are made in a designated plane in the flow field. These measurements are achieved by first seeding the flow with small (usually micron or sub-micron) tracer particles, and illuminating and imaging the seeded flow field twice consecutively within a small pulse separation time,  $\Delta t$  (which is of the order of microseconds).

The resulting image pair is then typically sub-divided into thousands of smaller interrogation areas (usually of the order of  $32 \times 32$  pixels) in which the particle displacement  $(\Delta x, \Delta y)$  of a small group of particles in the window is calculated to sub-pixel precision. For two single-exposure PIV images, the particle displacements are calculated using a

cross-correlation procedure, which matches intensity patterns in each window generated by the tracer particle images. This process is typically done in the frequency domain using Fast Fourier Transform (FFT) algorithms (Refs. 37 and 38). The pixel displacement in the interrogation window  $(\Delta x, \Delta y)$  is then used to calculate the local flow velocity in the window using

$$(U, V) = \frac{(\Delta x, \Delta y)}{M \Delta t} \quad (2.1)$$

where  $M$  is the image magnification calculated through an *in situ* calibration procedure in which an object of known dimension is imaged. This cross-correlation sequence is repeated for each set of corresponding interrogation windows, which allows measurements of the entire planar velocity field being focused by the camera. This sequence is shown for a vortex flow in Fig. 2.2. Further review of the PIV methodology can be found in Refs. 39–42.

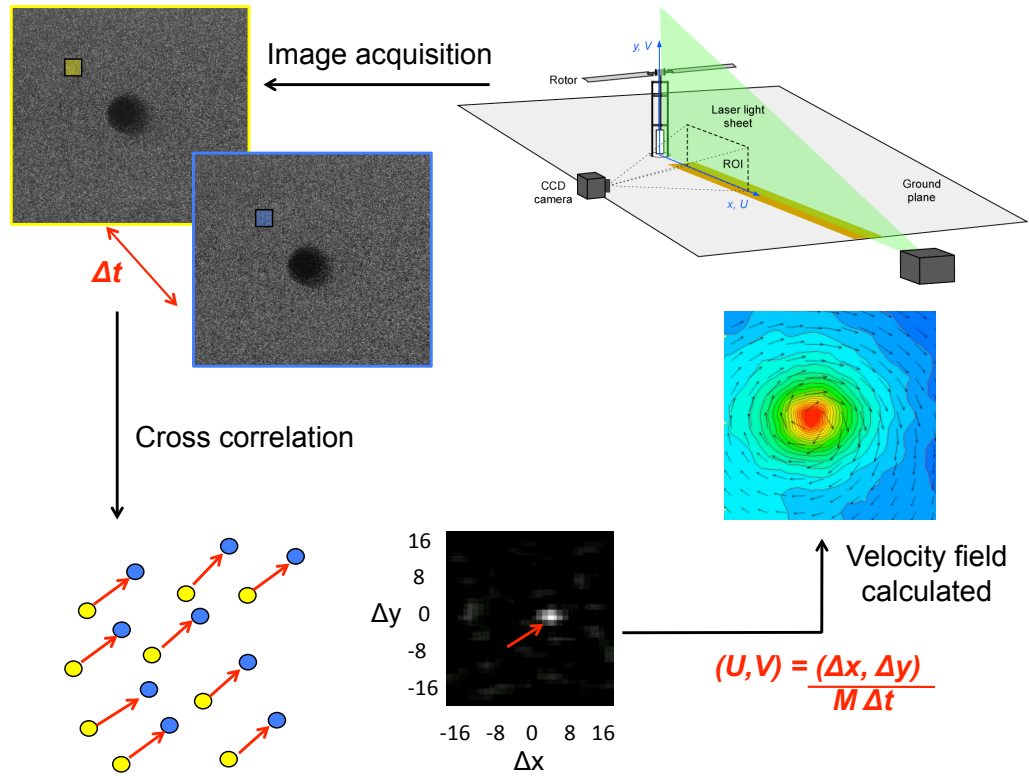


**Fig. 2.2: Schematic of PIV methodology**

In the present study, consecutive illumination and imaging of the flow was achieved through targeting a thin dual-pulsed laser light sheet in the plane of interest in the flow, and focusing the digital camera on this region (shown previously in Fig. 2.1). One digital camera was used, which allowed for the two in-plane velocity components  $U$  and  $V$  to be measured. For phase-resolved PIV, a 532 nm dual-pulse Nd:YAG laser with an optical arm and a cylindrical lens produced a thin light sheet with which to illuminate the flow. The laser was approximately 2 mm in thickness at its waist. For time-resolved PIV, a 527 nm high-speed Nd:YLF laser was used. In both cases, the air (the carrier phase) was seeded with a thermally produced mineral oil fog, which contained fine particles of nominal size  $0.2\ \mu\text{m}$ . These sub-micron particles were of the size needed to produce significant Mie scattering, but also small enough to follow the resulting vortical flows (Ref. 43).

### 2.2.2 Phase-Resolved PIV (PR-PIV)

In most PIV experiments, it is necessary to trigger the image acquisition sequence (Fig. 2.2) from a reference signal generated in the actual experiment itself. In the present work, the firing of the laser and the capture sequence of the camera was triggered by a once-per-revolution signal generated by a Hall-effect sensor mounted on the rotor shaft. This allowed velocity field measurements to be taken with the blades synchronized to a precise azimuthal position  $\psi$ , i.e., they were properly phase-resolved. This process allows the blade tip vortices to be studied as a function of wake age  $\zeta$ , which is defined as the time the vortices have spent in the wake in terms of degrees of blade rotation since they were born. A discussion of the overall uncertainties and challenges with the PR-PIV approach

for measuring rotor wake flows is given in Ref. 44.

The pulse separation time,  $\Delta t$ , between the illumination provided by two successive laser light sheets was  $10 \mu\text{s}$ , which corresponded to only  $0.18^\circ$  of blade rotation. Eighty PIV image pairs were collected for each phase-resolved measurement set, which has been shown to provide enough statistical data to ensure convergence when making both mean and time-dependent flow measurements (Ref. 45). The azimuthal location of the blades was then changed by  $20^\circ$  from one set of phase-resolved measurements to the next. The PR-PIV experiments were conducted without any sediment.

PR-PIV measurements were performed to examine the near-ground behavior of the vortical rotor wake, and the development of the boundary layer and wall jet on the ground plane. To increase the spatial resolution of the PIV measurements, a small region of interest (ROI) was chosen, which extended from  $1.15 \leq x/R \leq 1.85$  (physically corresponding to a 6-by-6 centimeter window size).

### 2.2.3 PIV Measurements Near Interfaces

Achieving high-fidelity PIV measurements near the ground (or any solid interface for that matter) poses several challenges (see, for example, Ref. 46). The most significant of these is the presence of high intensity reflections at the interface resulting from the laser illumination. Often these reflections are more intense than the Mie scattering from the seed particles themselves, and as such they can completely obfuscate the surface boundary layer flow (see Fig. 2.3).

The various types of flows found near an interface also pose several challenges for

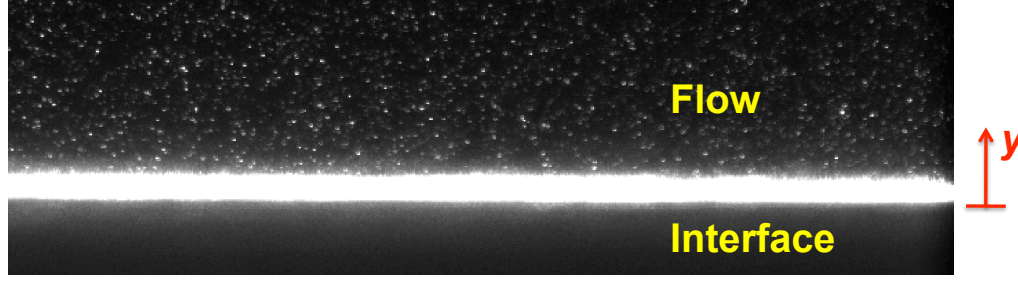


**Fig. 2.3: High-intensity reflections from an interface can mask the flow at the surface and in the boundary layer.**

PIV, mainly because of the high velocity gradients found in the wall-normal direction (i.e.,  $dU/dy$  when using the present coordinate system). This problem requires the flow in the boundary layer to be resolved with a sufficiently high spatial resolution in the wall-normal direction to reduce gradient bias errors during the cross-correlation process.

Other image processing issues include the need to account for the truncation of the signals at the interface, bearing in mind that reflections generated by tracer particles are completely absent in portions of the image that overlap the interface. A complete discussion of these issues, as well as the exact methodologies used to overcome many of these challenges, is included in Appendix A of this thesis.

Two separate processing grids were used to resolve the flow; one type of grid was used for the boundary layer region and another was used for the remainder of the flow. The recursive cross-correlation algorithm used for the boundary layer grid is discussed in Appendix A, while the deformation grid cross-correlation technique that was used for the remainder of the seeded area is discussed in Appendix B. The difference between the two grids was that the aspect ratio used for the correlation windows in the boundary layer grid was increased such that the window dimensions were greater in the direction parallel

to the interface. This technique reduced velocity gradient bias errors and increased the spatial resolution of the measurements in the wall-normal direction.

#### 2.2.4 Time-Resolved PIV (TR-PIV)

Because of the self- and mutually-induced effects on helicoidal wake vortices, the flow induced by a rotor can be aperiodic (Refs. 45–49). The levels of aperiodicity depend on several factors, including the number of blades, the vortex strengths, and the helicoidal pitch of adjacent turns of the vortices. Aperiodicity effects were particularly pronounced near the ground (see Chapter 3), which limits the ability to conduct any phase-averaging of the flow there. Therefore, time-resolved PIV (TR-PIV) measurements were also made.

The principles of TR-PIV are similar to PR-PIV, but the images are recorded as a continuous time-history at a high frame rate. This technique allows the proper temporal evolution of the flow to be examined, albeit with somewhat reduced spatial resolution. The deformation grid algorithm described in Appendix B was used to perform the cross-correlations on the PIV image pairs. The present TR-PIV system incorporated a high-speed digital camera with a double-pulsed Nd:YLF laser. This combination allowed for temporal velocity measurements to be made at a rate at up to 1,000 Hz with full pixel (1,024-by-1,024) resolution. In the present experiment, this corresponded to measurement of the velocity field once every 18 degrees of blade rotation. A total of 500 sequential images were taken for each data set, which allowed for measurements over 25 continuous rotor revolutions. In comparison, the PR-PIV system was only capable of making measurements at a rate of 15 Hz. In this latter case, because the maximum repe-



tition rate of the measurements was lower than the rotational frequency of the rotor, flow measurements could only be performed once every four rotor revolutions.

While the advantages of a TR-PIV system are obvious, there are some inherent challenges in using such a measurement technique for rotor wake studies. For example, because of the need to stream large amounts of data from the camera over a short time, the pixel resolution of the camera used for TR-PIV is not as high. In the present work, the TR-PIV images were recorded at a resolution of 1,024-by-1,024 pixels with an 8-bit dynamic range. In comparison, the PR-PIV images were recorded at a resolution of 2,048-by-2,048 pixels with a 12-bit dynamic range. Another challenge with TR-PIV originates from the extremely high repetition rate of the Nd:YLF laser, which results in the light energy per pulse being lower compared to that of the Nd:YAG laser used for the PR-PIV experiments. This problem poses some interesting experimental challenges when trying to illuminate the much smaller tracer particles.

## 2.3 Dual-Phase Experiments

In addition to the time-resolved PIV measurements, the high-speed image acquisition capabilities of the TR-PIV system allowed for time-resolved flow visualization and dual-phase PIV measurements to be carried out on the combined air/sediment flow environment. This allowed for a clear understanding of the particle transport physics at the ground under the action of the rotor wake. An especially advantageous result of time-resolved data streaming was the ability to track individual particles as they were convected through the flow.

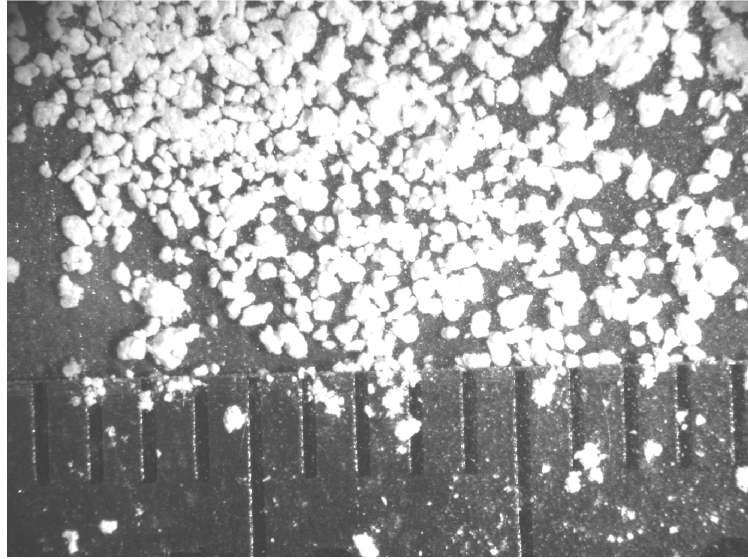
Multiple particle species were used to represent the sediment bed. Most of the present work describes results obtained using two sets of larger particle groups, which were separately used in successive experiments: Group A, which possessed aggregate sizes ranging from 40–800 microns in average diameter, and particle Group B, which possessed sizes ranging from 300–1,000 microns in average diameter. The particle sizes were estimated by imaging a small sample using a microscope with a calibration scale (Fig. 2.4).

The particles in Group A were close to spherical in shape, while Group B possessed particles that were more tetrahedral in shape, with elongated dimensions. The particle density was estimated by placing a fixed amount (10 grams) of each particle species in a liquid, and measuring the change in volume as a result of the particle deposition (both particle species were insoluble in the liquid). Using this technique, particle group A was measured to have a density of  $1,560 \pm 40 \text{ kg/m}^3$ , and particle group B was measured to have a density of  $1590 \pm 40 \text{ kg/m}^3$ . Using Eq. 1.11 and Stokes flow assumptions, the particle response time  $\tau_p$  for Group A particles ranged from 400 ms to 4,700 milliseconds, while the response time for Group B particles ranged from 7 to 3,050 milliseconds.

In the experiments, the particles were evenly distributed in a bed approximately 1 cm wide along a narrow quadrant on the ground plane that was centered on the plane illuminated by the laser sheet—see Fig. 2.1. While ongoing work is addressing the scaling issues associated with using dimensionally characteristic particle sizes, these first experiments still provided a first-principles based understanding of the mechanisms of sediment entrainment by the vortical flows produced in the rotor wake.

For all of the dual-phase experiments, the rotor was impulsively started to reach its

Particle Group A



Particle Group B

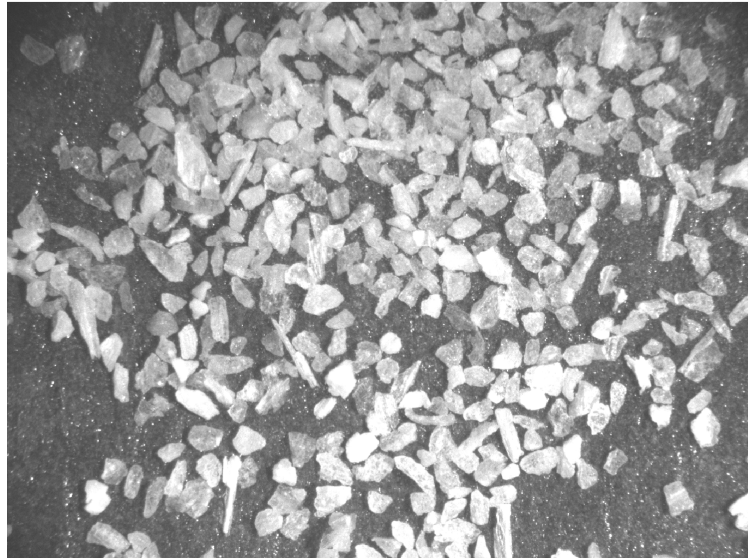


**Fig. 2.4: Microscope images of the particles used for the experiments. (Scale is in units of millimeters.)**

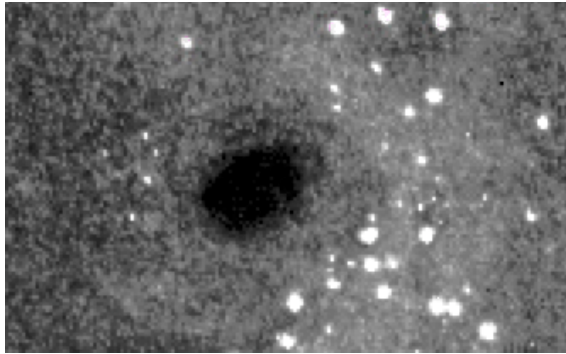
maximum operating speed of 50 Hz. This was done because the erosion of the sediment bed occurred relatively quickly as the rotor wake developed. Therefore, to capture the actual dynamics of the sediment uplift and erosion processes, images were acquired within a few revolutions after the rotor was started. Although there is still a residual flow tran-

sient in some of the measurements, the periodicity of the resulting flow was still found to be relatively good. Like the single-phase TR-PIV experiments, series of 500 images were collected during each experiment at a frame repetition rate of 1,000 Hz (i.e., over a time period corresponding to 25 rotor revolutions).

### 2.3.1 Dual-Phase PIV

An understanding of the momentum interchange between the rotor wake (the carrier phase) and the sediment particles (the dispersed phase) require simultaneous velocity measurements of both phases of flow. The main challenge in making dual-phase velocity measurements is in the proper separation of the two flow phases such that each velocity field can be measured independently of each other without any measurement interference from the other phase (i.e., without any cross-talk). For a raw PIV image containing both species of particles—see Fig. 2.5(a)—most normal PIV cross-correlation procedures will be ineffective near the particles in the dispersed phase. This is because the algorithms are incapable of discriminating between signals generated by different types of particles. In this case, phase-separation of the images must occur prior to performing the cross-correlations.

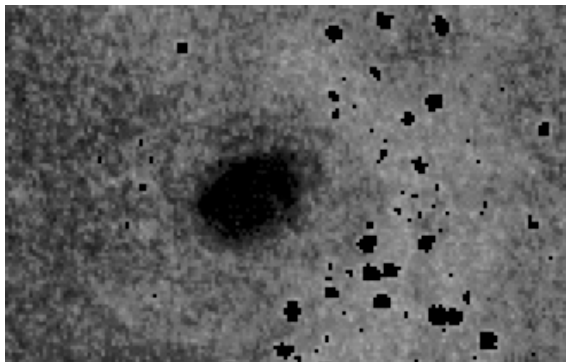
Different methods exist to discriminate between phases (Refs. 50–55). For these initial measurements, a simple technique was used to discriminate between the two particle species based on the amplitude of the scattered light between the particles. In the present experiments, the  $0.2\ \mu\text{m}$  smoke particles represented the carrier phase, while the two sediment particle groups represented the dispersed phase. Because the signal inten-



(a) Raw dual-phase PIV image



(b) PIV recording after thresholding (dispersed phase only)



(c) PIV image after masking (carrier phase only)

**Fig. 2.5: Phase-discrimination is required to make independent velocity measurements of both the carrier flow and of the sediment.**

sity produced by the large, bright particles in the dispersed phase was significantly higher than that produced by the much smaller sub-micron tracer particles, a thresholding technique was used to first separate the images of the dispersed sediment particles from the remainder of the flow—see Fig. 2.5(b). This allowed for a subset of dispersed phase image pairs to be created, which possessed pixel intensity values  $I_d(m, n)$  given by:

$$I_d(m, n) = \begin{cases} I(m, n) & \text{if } I(m, n) \geq I_{\text{thresh}} \\ 0 & \text{otherwise} \end{cases} \quad (2.2)$$

where  $I(m, n)$  is the corresponding pixel intensity values for the raw two-phase image, and  $I_{\text{thresh}}$  is the user-defined greyscale intensity threshold. The integers  $m$  and  $n$  simply represent the location of the pixel in the image and range from 1 to 1,024 in the TR-PIV images.

### 2.3.2 Particle Recognition and Tracking

After thresholding, individual sediment particle objects were recognized as series of connected pixels that met the threshold intensity. Based on Eq. 2.2, all connected pixels in the dispersed phase images with non-zero values of  $I_d$  were grouped into a given particle object, where the connectivity accounted for horizontal, vertical, and diagonal neighbors (see Fig. 2.6). For example, if pixel  $(i, j)$  possessed an intensity value  $I(i, j)$  greater than the threshold pixel intensity  $I_{\text{thresh}}$ , the algorithm would then examine the intensity values of each of its eight neighbors, above and below, left, and right, and for both sets of diagonals. Each neighboring pixel that also met the threshold was connected with the pixel  $(i, j)$ , this process being represented by the blue squares and solid red lines in Fig. 2.6. The procedure would then be repeated for all pixels until each object in the

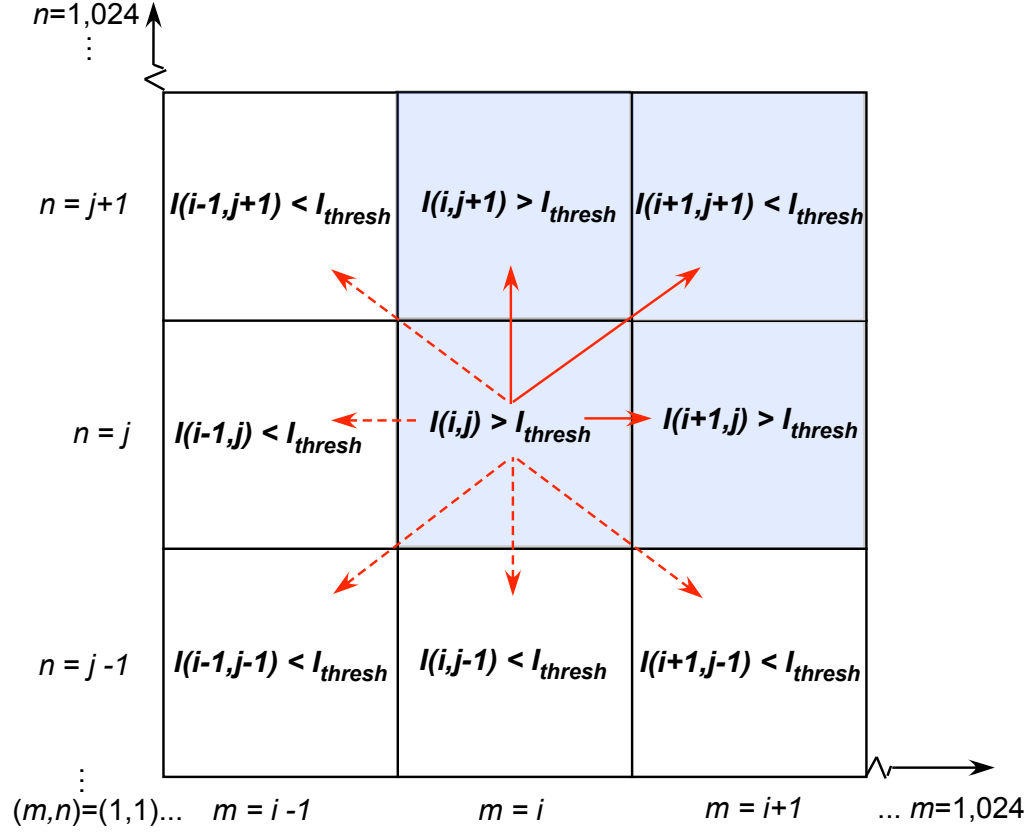


**Fig. 2.6: Particle objects were identified by connecting neighboring pixels that met the intensity threshold**

image was identified by a spatially connected pixellate array.

Once every sediment particle object was defined, the geometric center ( $X_c, Y_c$ ) of each object was determined to sub-pixel precision based on a geometric weighting of the pixels within the object, i.e.,

$$X_c = \frac{\sum X(i, j)}{N} \quad (2.3)$$

$$Y_c = \frac{\sum Y(i, j)}{N} \quad (2.4)$$

where  $N$  is the number of pixels in the object, and  $X(i, j)$  and  $Y(i, j)$  are the spatial locations of each pixel within the object. The displacement of object centroids from one PIV

frame to the next was then used for the calculation of sediment particle velocities. For the chosen pulse separation time, the displacement of the sediment particles was less than 3 pixels. Therefore, sediment particle matching was performed on the basis of matching particles in a 6-by-6 pixel search window centered on the dispersed particles in the reference image. The 6-by-6 search window proved to be small enough to limit the number of detected centroids to one per search region such that the algorithm did not confuse particles when tracking them. This technique proved effective well above the ground surface, where particle concentrations were dilute enough to discriminate between individual sediment particles. Near the surface, however, the higher particle concentration made particle recognition and matching more difficult, mainly because the edges of the particles often overlapped.

After the calculation of the sediment velocities, the raw images containing both phases of flow (Fig. 2.5(a)) were masked against the set of dispersed sediment particle images (Fig. 2.5(b)), resulting in a new subset of image pairs with just the smoke tracer particles (i.e., just the carrier phase). PIV cross-correlation using a deformation grid algorithm (as discussed in Appendix B) was then performed on the new carrier phase image pairs. This processing technique allowed for the independent flow measurements of the rotor, without interference from the signals generated by the dispersed phase particles.

### 2.3.3 Particle Tracking Uncertainties

In general, individual particle tracking is less accurate than using cross-correlations performed on a group of multiple particle images (as is done with standard PIV tech-



niques). One significant source of error is in the determination of the particle location, which is obtained by finding the geometric center of the best-fit ellipse that matches the Mie scattering profile from the particle. For a thresholding technique, like that used in the present study, the choice for the geometric center will be affected by the set threshold level because the edges of the particle typically have lower grayscale values than at the center of the particle image. Therefore, the under/over-estimate of an appropriate threshold level can noticeably affect the size and shape of the particles that are imaged by the particle tracking software. Furthermore, the present study used mainly non-spherical particles, which were also observed to acquire a spinning motion during their trajectories.

All of these foregoing effects were seen to change the scattering profiles of the particle images, sometimes leading to discrepancies in the observed particle geometries and sizes from one PIV frame to the next. Understandably, these discrepancies will introduce some uncertainties in the determination of the true geometric centers, so also leading to uncertainties in the final velocity estimates. Out-of-plane particle loss from the three-dimensional flow also served to limit the ability to track all of the sediment particles over longer periods of time. Using spherical particles with more uniform characteristics, which are being used for future experiments, could mitigate some of these issues. The sediment particles used for the present work, however, provided a good basis for initial proof of concept experiments, and the acquisition of preliminary quantitative dual-phase flow field results.

One final source of uncertainty was in the relatively small displacements in the sediment particles between image frames, which were measured to be smaller than the particle diameter. This was because a proper measurement of the high velocity gradients

in a rotor flow generally requires a relatively small pulse separation time between laser firings to minimize the acceleration and velocity gradient bias errors. This effect, in turn, reduced the particle displacements of the dispersed sediment particles. Ultimately there must be a compromise between simultaneously measuring the two phases of the flow, bearing in mind that the optimal pulse separation time needed for one phase of the flow will not necessarily be the same as that needed for the other phase.

## 2.4 Summary

A summary of the experimental methodologies used in the present work have been presented in this chapter. The work has used particle image velocimetry (PIV) and flow visualization. The operating principle of PIV has been explained, in addition to the techniques of phase-resolved and time-resolved PIV as applied to rotor flow measurements. Additional experimental procedures detailing the techniques used to make near-wall PIV measurements are provided in the appendices. Dual-phase PIV was performed to explore the interaction between the rotor flow and the entrained sediment. A thresholding technique was employed to discriminate between the carrier and dispersed phases of flow, combined with a particle tracking algorithm used to measure the velocity of the dispersed sediment particles.

## Chapter 3

### **Single Phase Flow Measurements**

This chapter presents both the phase-resolved (PR-PIV) and time-resolved PIV (TR-PIV) measurements of the rotor flow near the ground. Proper understanding of the near-wall flow is specifically needed to analyze the processes of sediment entrainment and transport by the rotor flow, which are discussed in the Chapter 4. Much effort was directed towards studying the evolution of the blade tip vortices, and their effect on the boundary layer. Additional time-resolved measurements proved fundamental to understanding the causes of aperiodicity in the flow.

#### 3.1 Near-Ground Flow Characteristics

The details of the flow in the near wall region were measured using the PR-PIV system, which provided sufficient spatial resolution to expose the detailed characteristics of the wall-jet and boundary layer flow. The region of interest (ROI) corresponded to a specific region at the boundaries of the rotor wake where the blade tip vortices were observed to impinge upon the ground plane—see Fig. 3.1. One challenge of making vortex measurements at these old vortex wake ages is the size of the seed voids at the center of the vortex. In the present experiments, the seed voids ranged anywhere from 3 to 6 mm in diameter, which made cross-correlation difficult, and sometimes impossible, within the viscous cores of the vortices. Thus, most results and analysis have been focused

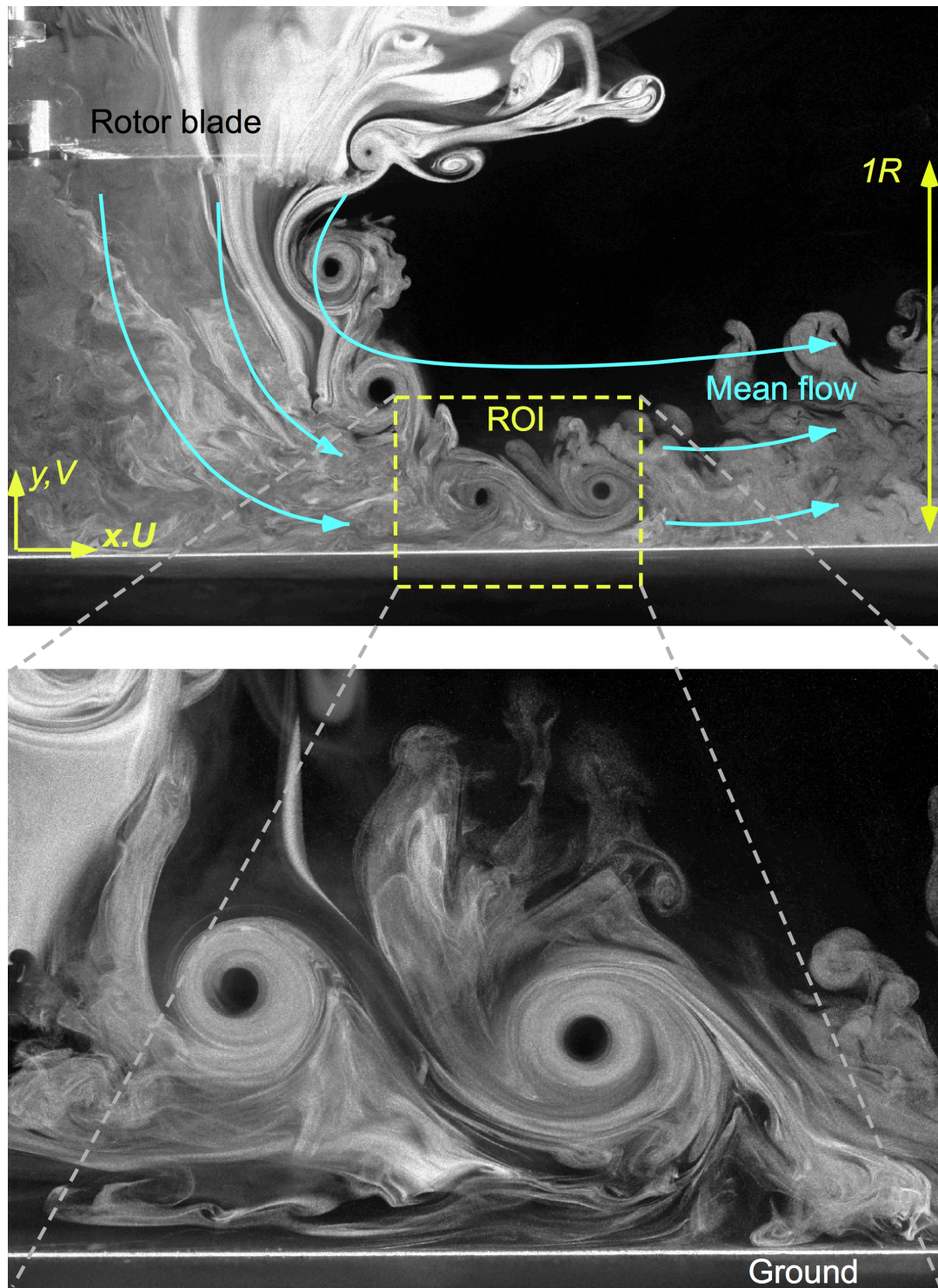


**Fig. 3.1:** The region of primary interest was focused in a small region at the periphery of the rotor wake as it came into proximity to the ground.

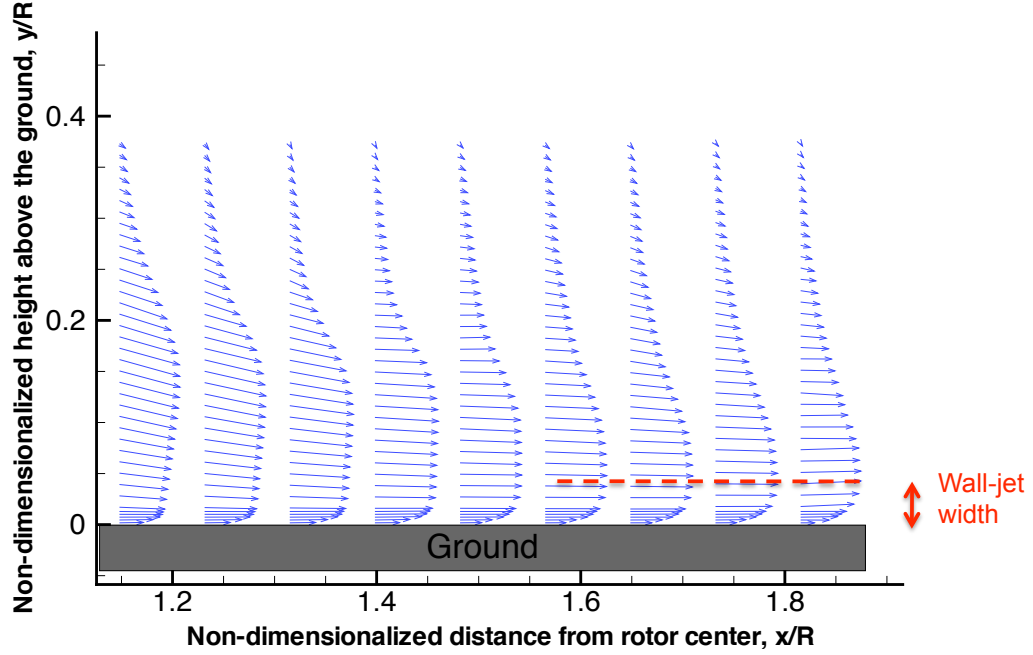


**Fig. 3.2: Measurements of the mean velocity profiles at the ground surface as obtained using PR-PIV.**

on the effects the vortices have on the flow beneath their core. For clarity, results will be discussed in terms of both the groundwash velocity profiles (i.e., the  $U$  velocity), and the upwash and downwash velocities (positive and negative  $V$  velocity, respectively).

Figure 3.2 shows the mean boundary layer velocity profiles obtained in the ROI by ensemble averaging all phase-resolved velocity fields. Only a few of the profiles are shown to avoid congestion. The width of the mean wall jet (defined as the height of the maximum mean groundwash velocity  $U$  in each velocity profile) reached a steady value of  $0.048 \pm 0.042 y/R$  (4.1 mm) in the ROI in Fig. 3.1. A trend line is plotted in Fig. 3.2 along with the velocity profiles to show the convergence of the wall-jet width in this region.

The characteristics of the near-wall flow, however, were found to be greatly affected by the convection of the wake vortices (see Fig. 3.3). In several of the instantaneous ve-

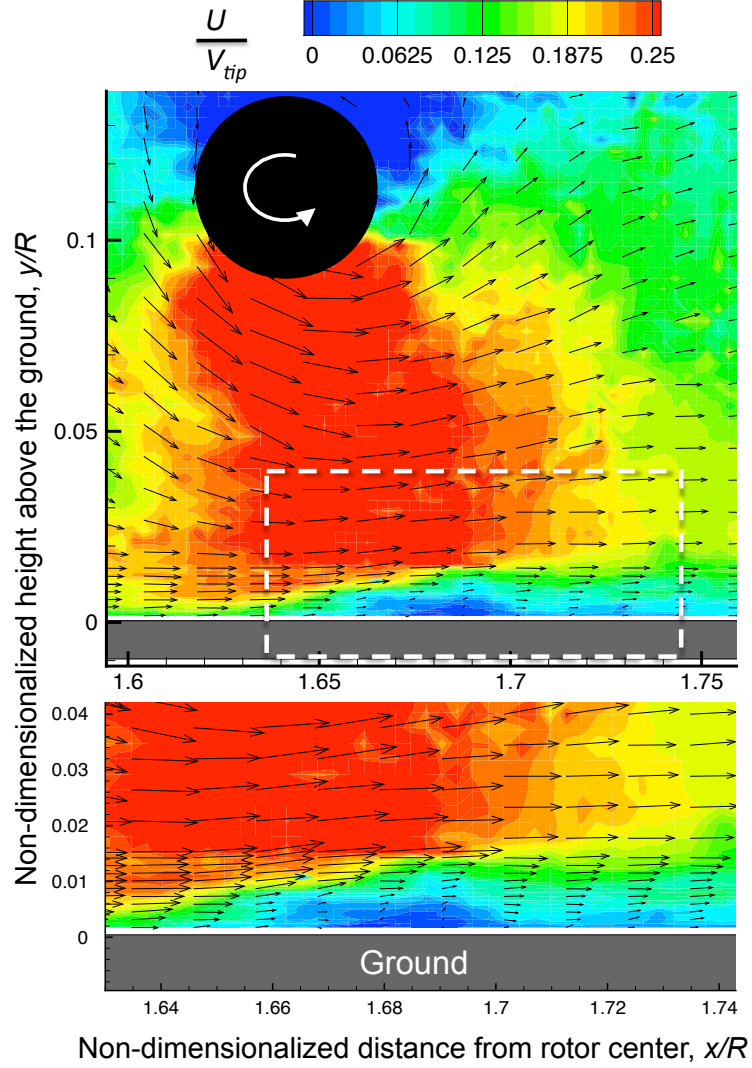


**Fig. 3.3: High-resolution PR-PIV measurements showed localized regions of boundary layer flow separation on the ground plane ( $\zeta = 600^\circ$ ).**

locity vector maps, localized regions of flow separation were observed downstream of the convecting vortices. This phenomenon is shown in Fig. 3.3, which details the instantaneous velocity field beneath a blade tip vortex at  $\zeta = 600^\circ$ . The centroid of vorticity of the vortex in this case was measured to be at  $(x/R, y/R) = (1.65, 0.11)$ . A separation bubble was observed to be present just downstream of the vortex flow, whereas the boundary layer was fully attached in the region directly below the vortex flow.

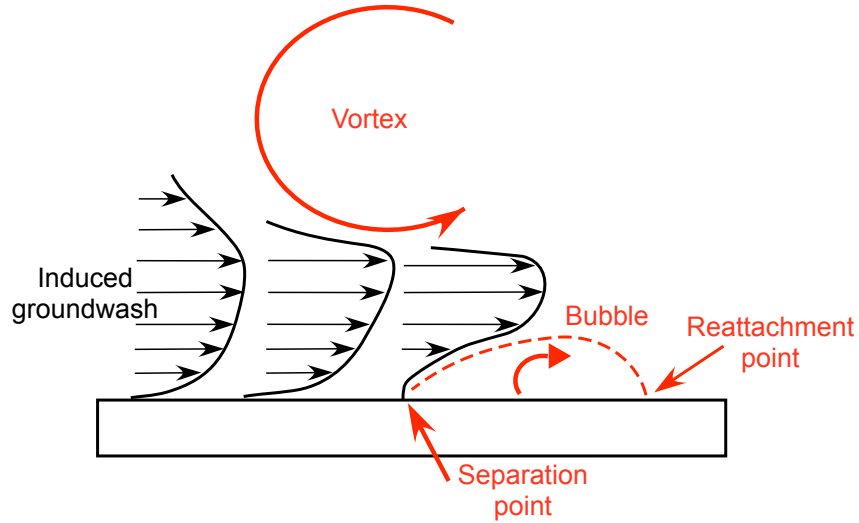


**Fig. 3.4: Schematic of the process of vortex-induced flow separation.**

A schematic of this process is shown in Fig. 3.4. This form of viscous vortex/boundary layer interaction has been described by Harvey & Perry (Ref. 56) for conditions where a tip vortex trailed from a wing came under the influence of the ground. The classic explanation is that because the static pressure reaches a minimum directly underneath the vortex flow, the developing boundary layer faces a steep adverse pressure gradient downstream of the vortex as a consequence of the slower moving fluid and higher pressures. This pressure gradient can become strong enough to produce flow separation and the formation separation bubble, which contains a region of lower velocity or even recirculating fluid with reverse flow. Clearly, this mechanism is viscous dominated, increasing the complexity of the modeling requirements for shear stress calculations and particle entrainment models in brownout simulations.

The effect of this pressure gradient in the shape of the boundary layer is further shown in Figs. 3.5(a) and 3.5(b), which each show an example of the instantaneous flow field produced by the  $\zeta=600^\circ$  vortex compared with the mean boundary layer flow.

Both plots show the variation of groundwash with height, and were obtained by making a slicing cut in the  $y$  direction. In the case of Fig. 3.5(a), the cut was made directly through the centroid of vorticity of the vortex ( $x/R = 1.65$  in this case). For Fig. 3.5(b), the cut was made slightly downstream at  $x/R = 1.69$ . In both cases, the mean groundwash profile at the same spatial location is plotted as a reference. Figure 3.5(a) shows an increase in the groundwash velocities in all portions of the boundary layer compared to the mean flow. Figure 3.5(b), however, shows an increase in the groundwash in only the upper portions of the boundary layer. The near-wall velocity profiles, however, show significantly lower levels of groundwash compared to the mean flow, and also a different profile shape.

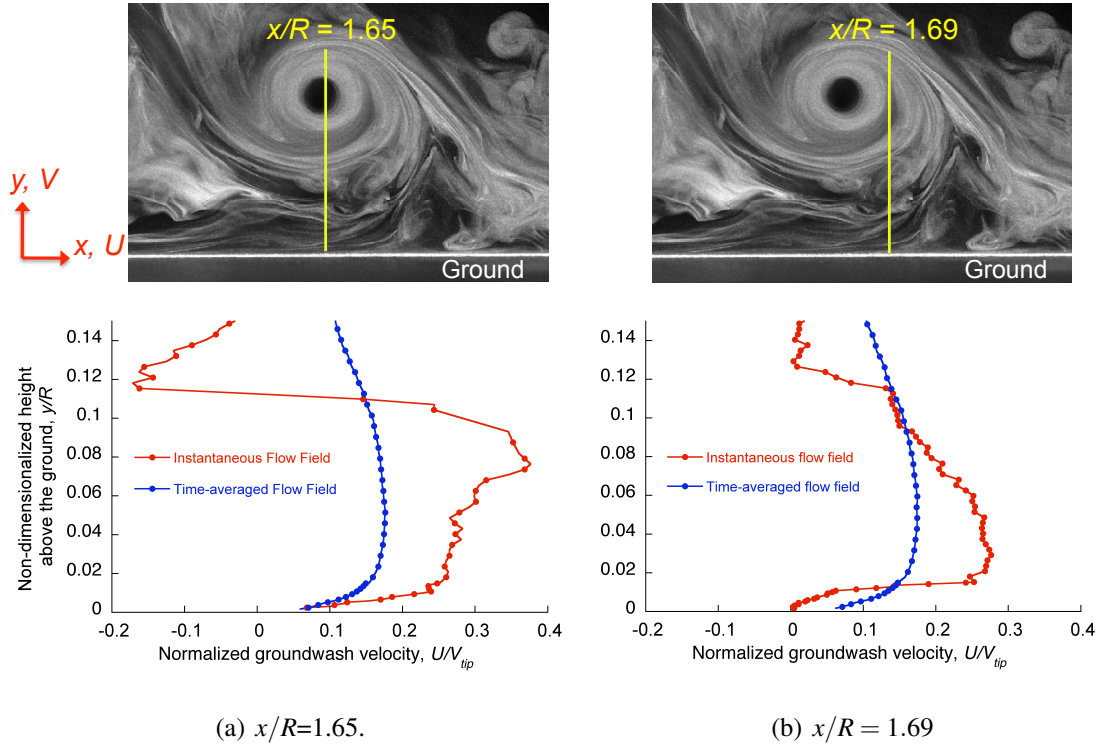


**Fig. 3.5: Time-averaged groundwash profiles compared to instantaneous groundwash profiles produced by a blade tip vortex at at  $\zeta = 600^\circ$ : (a) profiles below the vortex center, (b) profiles downstream of the vortex center.**



The characteristics of the boundary layer profiles measured in proximity to the impinging vortices have significant consequences on the wall shear  $\tau_w$ , which is typically the reference point for sediment entrainment calculations (Eq. 1.12, for example). At the point of flow separation downstream of the vortex flow, the wall shear will be zero. However, upstream of the flow separation point where the boundary layer is still fully attached, significantly higher values of shear stress will be produced. Thus, it can be expected that wall shear produced by the impinging vortical flow of the rotor will vary in both space and time, and be highly dependent upon the trajectory of the vortices.

The foregoing observations raise several questions about the direct application of equilibrium threshold and boundary layer models to represent the problem of sediment entrainment and subsequent dust cloud developments in brownout simulations. Recall from Chapter 1, that all threshold and boundary layer models are empirical, and derived for specific flow conditions. In the case of classic wind-erosion studies (which are now being used in brownout simulations—Refs. 4–7), an equilibrium fully turbulent boundary layer is produced experimentally (typically in a wind-tunnel, by tripping the flow) over the sediment bed in question. The threshold friction velocity for the sediment bed is then measured by increasing the wind-tunnel free stream velocity until significant particle mobilization is produced. Near-wall time-averaged flow measurements of the wind-tunnel velocity at different heights are then fit to an empirical boundary layer profile (usually Eq. 1.1), such that the threshold for particle mobilization is referenced to an interpolated mean wall shear (or equivalently, friction velocity).

The underlying assumption here, is that the velocity profile given by the model is representative of true flow velocity in the boundary layer. Judging from the profiles in

Figs. 3.3 and 3.5(a), and 3.5(b), however, the boundary layer formed by the wake impinging on the surface is highly unsteady, subject to local flow separations and reattachment, and so does not, in general, take the logarithmic form of Eq. 1.1. At this point, the use of this model (or any variation of an equilibrium boundary layer model) is questionable for shear stress calculations in brownout simulations.

### 3.2 Challenges in the Measurement of Wall Shear

The use of meso-scale sediment entrainment models historically require a knowledge of the wall shear, and the shear stress distribution in the boundary layer, in general. From a fluid mechanics measurement perspective, quantitative measurements of the wall shear must be interpolated from measured velocity profiles. The most reliable way to achieve this is a high sampling of the flow velocity within a laminar sub-layer region, in which the turbulent fluctuations of the flow are suppressed and the dominant stress is the viscous stress. Here, the velocity is well-known to increase linearly with height (i.e.,  $dU/dy$  is constant), and the wall shear can be estimated using Newton's law, i.e.:

$$\tau_w = \mu \left. \frac{dU}{dy} \right|_{y \rightarrow 0} \quad (3.1)$$

For the current PR-PIV experiments, the closest measurement point to the wall was 140  $\mu\text{m}$ . While extremely close, a distinct linear region with multiple flow velocity measurements was not observed, making a direct measure of the wall shear challenging. A knowledge of the shear stress produced by the rotor flow, must be obtained from the Reynolds stress (i.e.,  $\overline{U'V'}$ ), which is the dominant stress in the boundary layer outside the laminar sublayer. The Reynolds stress specifically is a quantification of the apparent stress acting

on the mean flow because of the random momentum fluxes caused by the turbulence.

For rotor flows, however, the measurement of  $\overline{U'V'}$  in the boundary layer is complicated by the fact that the flow is inherently unsteady. For example, the substantial excursions from the mean boundary layer flow shown in Figs. 3.5(a) are not random effects caused by turbulence (i.e., they are not Reynolds stresses), and they are inherent to the convection of the large-scale vortices within the flow. Therefore, for shear stress measurements within the boundary layer, the momentum fluxes from the convection of the vortices have to be separated from the random momentum fluxes caused by turbulence.

To achieve this goal, the rotor flow has to be periodic such the vortices will remain in the same spatial location in successive phase-locked measurements. This result, however, was not the case in the current experiment because the flow was observed to be significantly aperiodic. Aperiodicity is an inherent characteristic of rotor wake flows, in general, and arises because of the self- and mutually-induced effects of the strong blade tip vortices (Ref. 48). The susceptibility to instability results in three-dimensional spatial and temporal perturbations in the rotor wake as it ages. For the PR-PIV measurements, aperiodicity manifests in any given measurement plane as a “wandering” of the phase-resolved spatial locations of the vortex cores (Ref. 45).

The “wandering” effect is shown in Figs. 3.6, which in this case represents the locus of vortex core locations that were observed during one set of phase-resolved measurements near the ground plane. For these measurements, the blade azimuth angle was phase-locked at  $\psi = 140^\circ$ . Each data point represents the centroid of vorticity of each tip vortex that was present in each instantaneous measurement. For a perfectly periodic flow, the vortices would maintain the same spatial location in each successive phase-locked

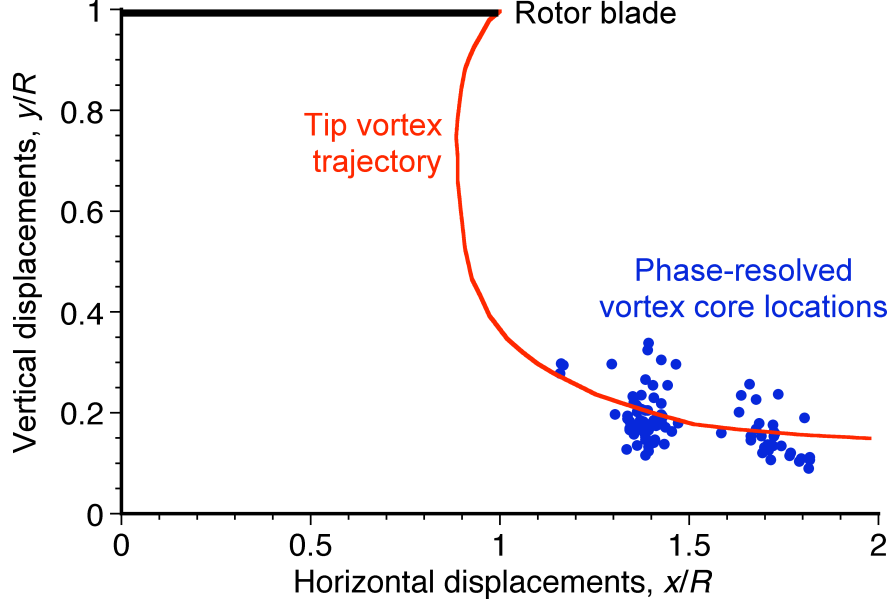
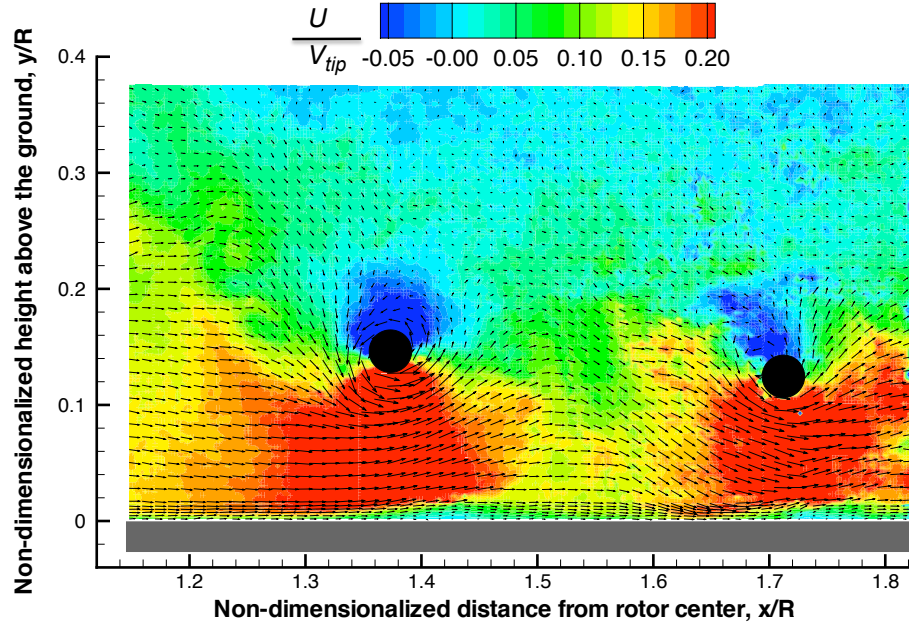


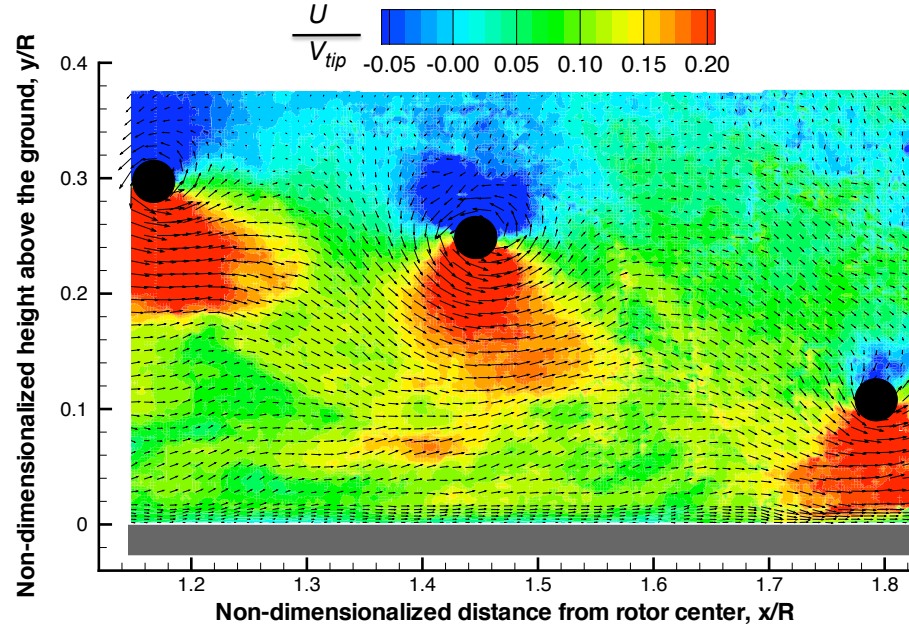
**Fig. 3.6: Aperiodicity in the flow leads to movements in the spatial locations of the tip vortex cores from rotor revolution to rotor revolution.**

measurement. This is clearly not the case judging from the results in Fig. 3.6.

Two examples of the instantaneous flow is given in Fig. 3.7, the contour representing the normalized groundwash velocity  $U/V_{\text{tip}}$ . In Fig. 3.7(a), two of the blade tip vortices are seen within the ROI (those corresponding to  $\zeta = 500^\circ$  and  $\zeta = 680^\circ$ ), and are convecting roughly parallel to the ground plane. Figure 3.7(b) also shows an instantaneous flow measurement within the same phase-locked measurement set. Here, three blade tip vortices ( $\zeta = 320^\circ$ ,  $\zeta = 500^\circ$ , and  $\zeta = 680^\circ$ ) can be seen within the ROI, each with different spacings between them compared to those in Fig. 3.7(a). The center of the vortices in this case were additionally observed to be significantly higher above the ground plane compared to those in Fig. 3.7(a). Phase-averaging an ensemble of instantaneous vector maps like these produces significant bias, and does not allow the calculation of the true mean flow that is induced by the vortices.



(a) Instantaneous phase-resolved measurement of the rotor flow near the ground for  $\psi = 140^\circ$ .



(b) Another flow measurement at  $\psi = 140^\circ$ , showing significantly different vortex locations.

**Fig. 3.7: Instantaneous velocity fields produced by the rotor flow, showing significant aperiodicity in the flow.**

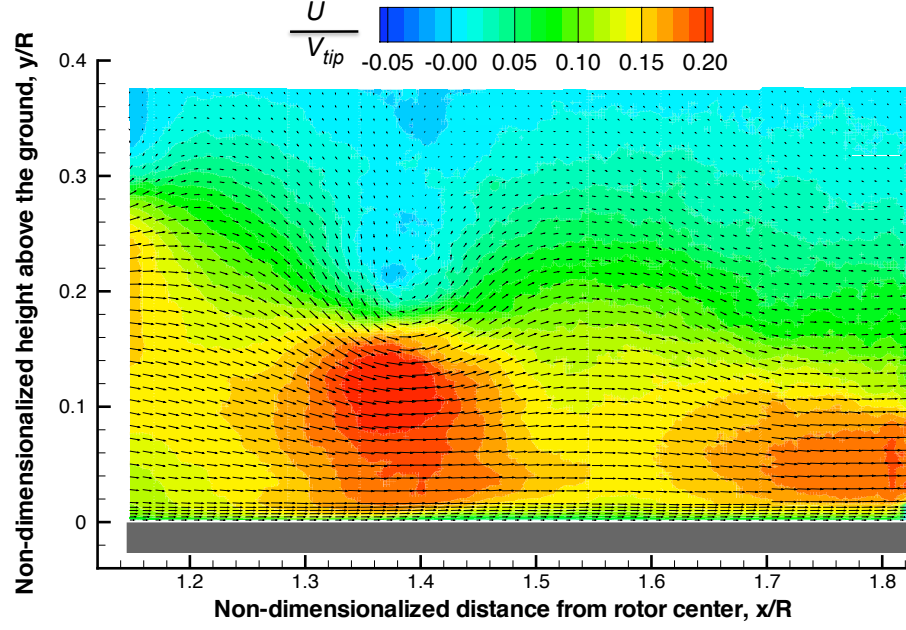


**Fig. 3.8: Mean flow field obtained through phase-averaging at  $\psi = 140^\circ$ .**

Figure 3.8 shows this effect, which is the phase-resolved mean flow field generated by ensemble-averaging each instantaneous measurement that was shown in Fig. 3.6. While some signature of a vortex flow can be seen near the center of the ROI, the signature of the individual blade tip vortices in Figs. 3.7(a) and 3.7(b) is lost because of the phase-averaging process. Thus, the calculation of the proper phase-resolved mean flow produced by the vortices could not be obtained. Future work is ongoing to produce flows in which the vortex trajectory is more periodic (see Chapter 5). Examples of the instantaneous flow (like that shown in Fig. 3.3), however, give better insight into the actual physical processes that are associated with the unsteady boundary layer formed by the rotor wake as it interacts with the ground.

Although the aperiodicity of the flow did not allow for quantitative measures of shear stress in the boundary layer, the results in Fig. 3.5(a) and many other instantaneous flow measurements taken showed a much higher groundwash and wall-normal velocity

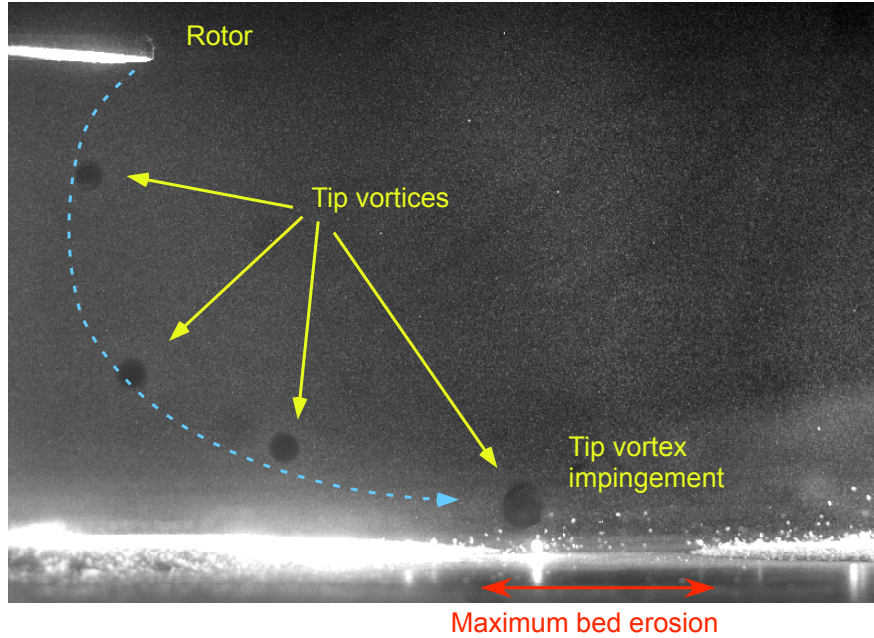


**Fig. 3.9: Maximum bed erosion occurred in the zone of vortex wake impingement on the ground.**

$dU/dy$  gradient approaching the wall beneath the vortices (at least when the boundary layer was attached). This suggested high shear was produced and a significant momentum flux was applied to the bed. Additionally, the dual-phase experiments (detailed mostly in Chapter 4) revealed that the maximum sediment entrainment rates were observed to be in the zone of vortex impingement on the ground. This result is shown in Fig. 3.9, which is a dual-phase flow visualization image of a sediment bed of particle Group B after the rotor was run long enough for significant sediment to be eroded from the bed. The most significant presence of erosion is clearly shown to be in a small annular zone where the vortices are in close proximity to the ground, suggesting their induced flow has significant impact on particle entrainment. This evidence, combined with observations like those in Fig. 3.5(a), suggests that the wall shear does in fact increase because of the impingement of the wake vortices on the ground.

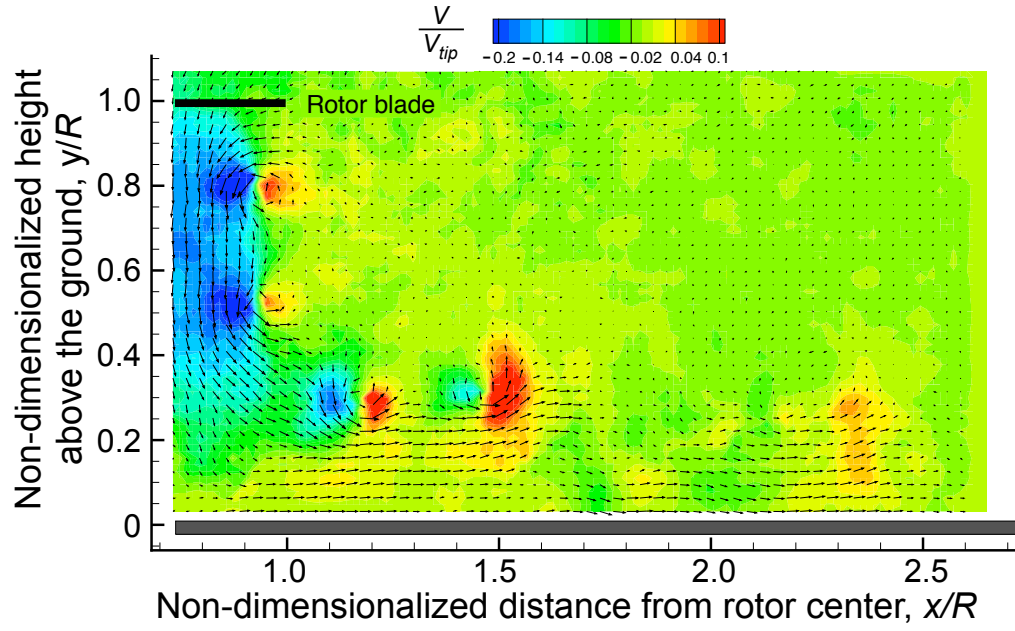
### 3.3 Vortex Merging

While the PR-PIV measurements showed significant aperiodicity in the flow, they cannot give any information as to why these effects develop. To achieve this understanding, a knowledge of the temporal evolution of the flow is needed. Time-resolved flow measurements using the TR-PIV system showed that underlying mechanism of the aperiodicity was the tendency of adjacent blade tip vortices in the rotor wake to pair with each another, and to eventually roll-up and merge into a larger vortical flow disturbance.

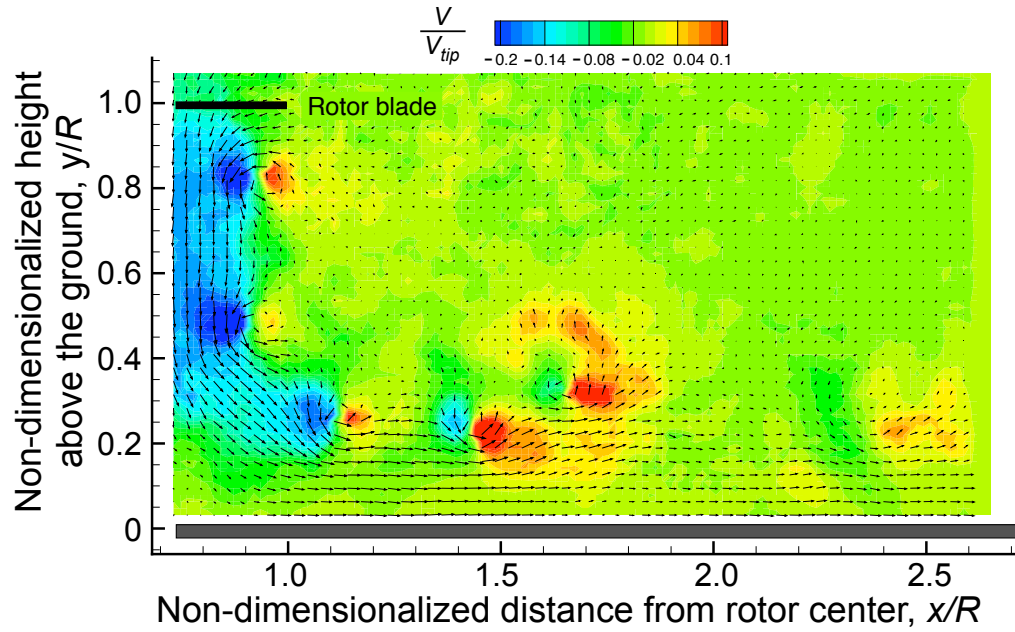
This process is detailed in Figs. 3.10 and 3.11, which depicts contours of the measured  $V$  velocity (non-dimensionalized by the rotor tip speed,  $V_{\text{tip}}$ ), blue denoting regions of downwash, and red denoting regions of upwash. The time scale of the images in Figs. 3.10 and 3.11 span just over one revolution ( $\Delta\psi = 396^\circ$ ). The opposing blue and red lobes arise from the asymmetric vertical velocity field produced by the vortices (in this case which have counter-clockwise rotation). Because of this flow asymmetry, the younger (inboard) vortex induces an upwash velocity on its older (outboard) neighbor, while the older vortex induces a downwash velocity upon the younger vortex. These mutually-induced velocities results in a pairing of two adjacent vortices, causing them to roll up and then to merge, in this case by a downstream distance of  $x/R = 2$ . It was observed that this phenomenon was aperiodic, in that it did not occur at the same spatial location for every pair of adjacent vortices.

In addition to causing the flow to be aperiodic, another key consequence of the roll-up and merging of vortices was the creation of a secondary vortical flow region, which formed radially on the ground outside the periphery of the rotor disk—see Fig. 3.11. This





(a) Adjacent vortices approach one another:  $\psi = 103^\circ$ .



(b) Adjacent vortices roll up:  $\psi = 283^\circ$ .

**Fig. 3.10: Sequence of TR-PIV images showing the roll-up of two adjacent vortices**

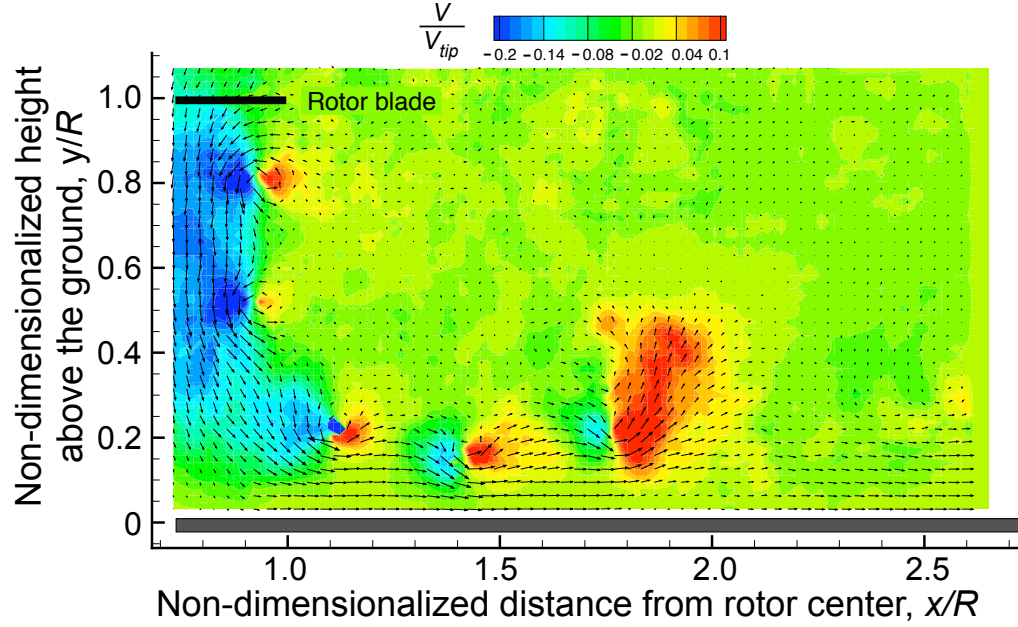


**Fig. 3.11: TR-PIV image showing the strong upwash field generated by the merging of adjacent tip vortices:  $\psi = 139^\circ$ .**

vortical region continues to expand radially, and eventually dissipates as the next vortical zone forms with a new pair of vortices. Because the resulting vortical flow contains the combined circulation from the two original blade tip vortices, the induced velocity field was noted to affect a considerably larger region of the flow compared to that produced by a single tip vortex. Figure 3.11 also shows the formation of a pronounced region of upwash in the resulting vortical flow. The combined circulation also served to locally increase the surface groundwash velocities, which are key for the determination of the wall shear and sediment entrainment levels. Specifically, this merging process proved to be a fundamental mechanism in the vertical transport of bedload sediment (see Chapter 4).

### 3.4 Summary

Single-phase measurements of the flow field produced by a hovering rotor were presented in this chapter, with emphasis on the near-wall flow and the interaction between the blade tip vortices and the boundary layer flow. It was shown that the impingement of the vortices caused significant excursions in the boundary layer profiles, and even regions of local flow separation. The main challenge in quantifying the shear stress produced by the vortices resulted from the highly aperiodic flow near the ground, which caused a large spatial variance in the phase-resolved locations of the vortices. Time-resolved PIV measurements revealed the cause of this aperiodicity to be the unsteady roll-up and merging of adjacent wake vortices near the ground. This merging process additionally served to strengthen the surface velocities and upwash field near the ground.

## Chapter 4

### Dual-Phase Flow Measurements

The following chapter presents experimental results and analysis of the dual-phase flow environment created by a hovering rotor near the ground. Emphasis was placed on examining the mechanisms of sediment entrainment by the rotor flow, and also on the mechanisms of suspension and vertical transport of sediment. While different sediment particle groups were observed to have different transport characteristics, the entrainment and transport mechanisms observed in the present work contrasted significantly against those typically seen in more uniform turbulent flows.

#### 4.1 Sediment Entrainment

A knowledge of how sediment is picked up, or entrained, by the rotor flow is critical in eventually modeling the mass flux rates of sediment introduced into the external flow field. In the present experiments, there were three primary observed mechanisms of sediment entrainment:

1. Direct aerodynamic entrainment
2. Saltation bombardment
3. Bombardment from suspended particles reingested into the vortical rotor flow (referred to as *reingestion bombardment*)

While the aerodynamic entrainment of particles is dependent upon the shear stress imparted to the sediment bed by the flow (as was discussed in Chapter 3), the latter two mechanisms depend upon collision dynamics between individual particles.

## 4.2 Saltation and Bombardment

The classical particle transport mechanism of saltation (see Chapter 1) was observed in the present experiments, and was observed to initiate on the periphery of the rotor disk at approximately  $x/R = 1.25$ . Inboard of this radial station, little particle flux occurred because of the smaller groundwash velocities (i.e., the aerodynamic threshold needed for particle mobilization was not met).

Figure 4.1 shows a representative schematic of the initiation of the saltation process in terms of the rotor coordinates. As the groundwash velocities increased past the

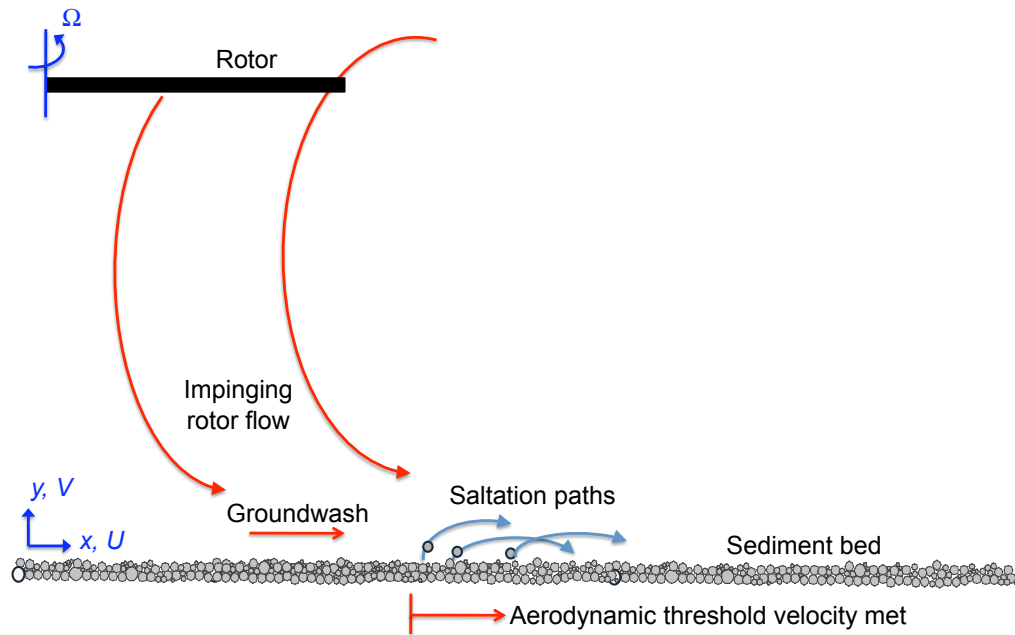
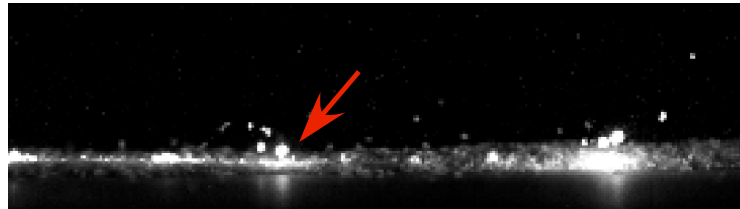


**Fig. 4.1: Schematic of representative saltation paths below the rotor.**



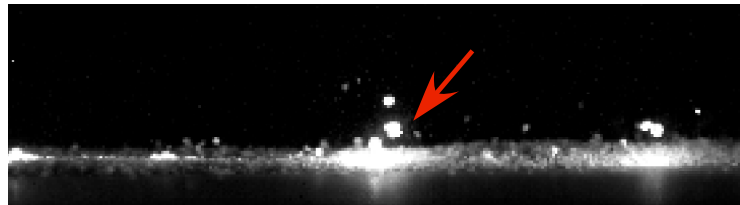
(a) Sediment particle in saltation



(b) Particle descent



(c) Saltation bombardment



(d) Ejection of new particles



(e) New particles continue in saltation

**Fig. 4.2: Time-sequence of images showing the process of saltation and saltation bombardment.**

threshold criterion, the particles were observed to be aerodynamically entrained into the flow. Many of the larger particles (mainly those in particle Group B), however, were too heavy and incapable of being suspended in the flow, and thus fell back to the bed, ejecting new particles through saltation bombardment. Figure 4.2 shows this latter process, as a descending particle (of Group B) collides with the sediment bed and allows new particles to be entrained into the flow through the bombardment process. The time-scale of the sequence in Fig. 4.2 is 22 milliseconds, corresponding to  $396^\circ$  of blade rotation.

For sediment transport in rotor wake flows, however, another form of bombardment was also observed. In this case, small sediment particles that were lofted upwards and suspended (see next section) were sometimes observed to be recirculated into the vortical rotor wake. A representative schematic of the possible trajectories of these reingested particles is given in Fig. 4.3. As the sediment is accelerated vertically downward in the

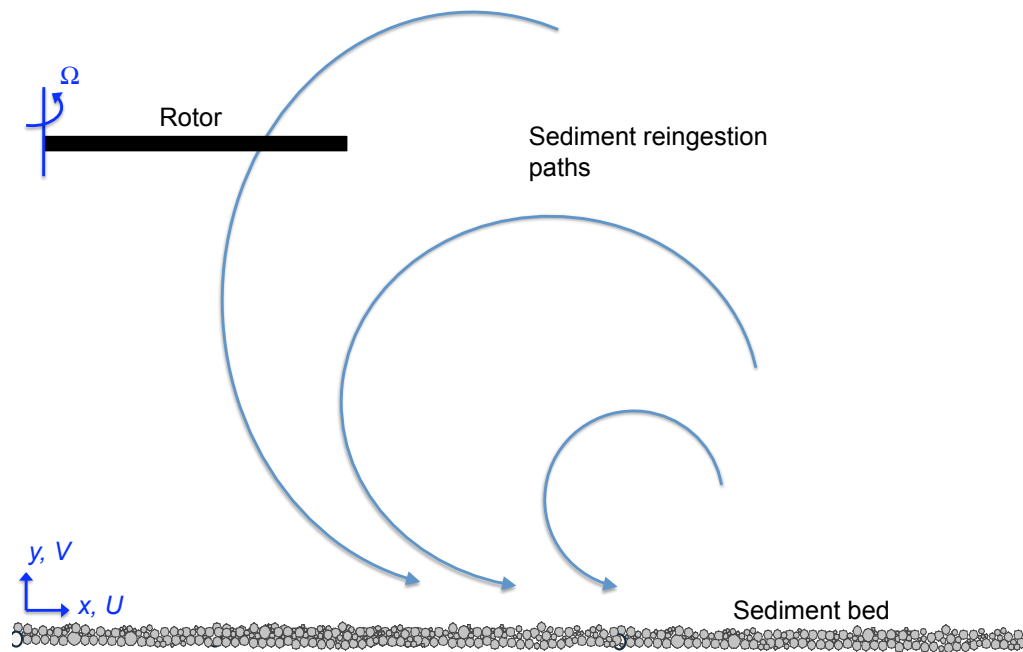
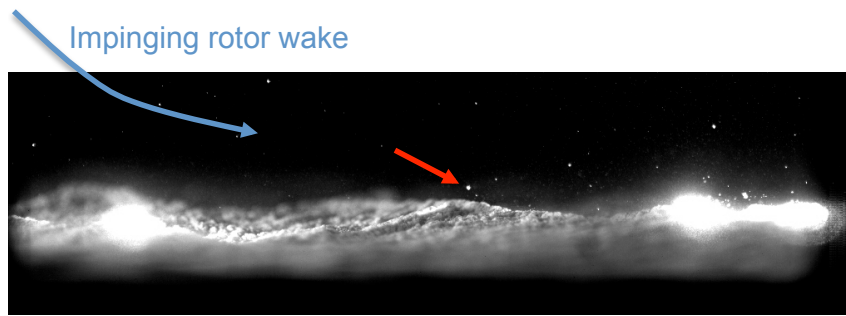
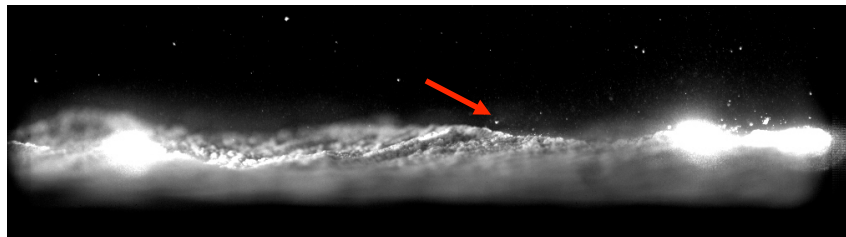


**Fig. 4.3: Schematic of representative reingestion paths taken by suspended particles**



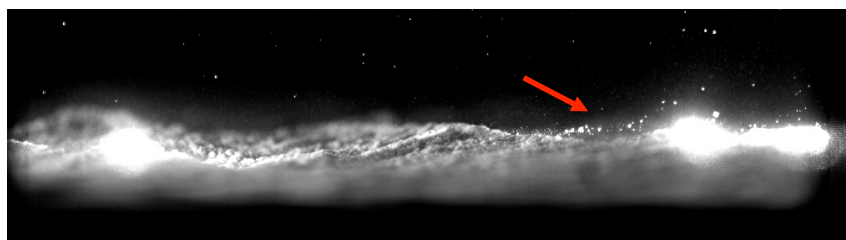
(a) Recirculated particle



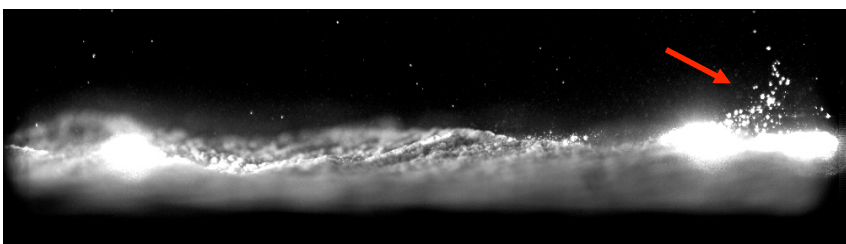
(b) Descent of recirculated particle



(c) Reingestion bombardment



(d) Initial ejection of new sediment



(e) Secondary ejection of new sediment

**Fig. 4.4: Time-sequence of images showing the process of reingestion bombardment.**



rotor wake, it impacts the sediment bed at a steep angle and at a relatively high velocity. This process is shown in Fig. 4.4, in which a recirculated particle (in this case from the smallest particles of Group A) sets off a cascading process of more sediment ejection. The first ejection from bombardment is seen at the point of impact of the recirculated particle, and then a further ejection of particles is produced on the lee side of a dune formed on the sediment bed. The time-scale of the sequence in Fig. 4.4 is 11 milliseconds, corresponding to  $198^\circ$  of blade rotation.

In general, bombardment or “splash” from reingested particles was seen to lead to sporadic bursts of smaller particles from the sediment bed. This process may contribute to the development of brownout conditions because small dust particles often require some form of bombardment to occur for disintegration of the aggregate material from which they inevitably originate.

### 4.3 Sediment Transport in the Rotor Flow

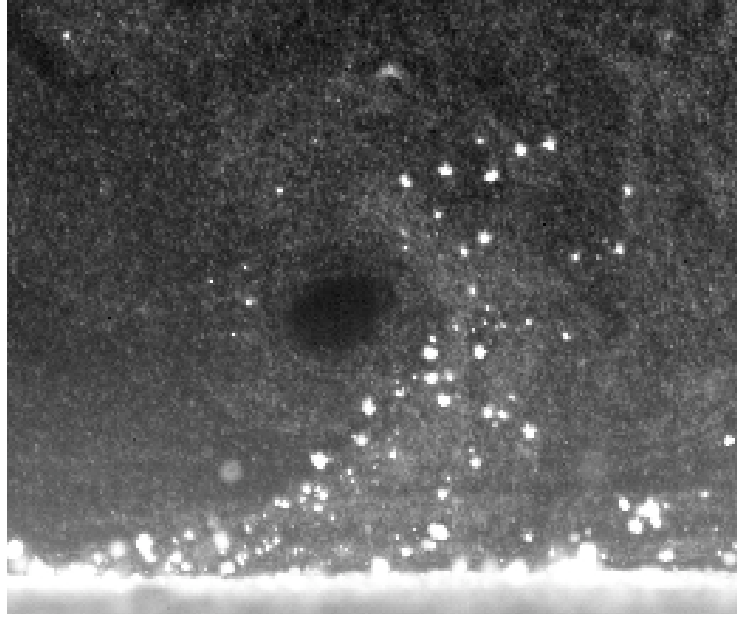
Once entrained, either through aerodynamic forces or the process of bombardment, airborne sediment is subject to the external velocity field induced by the rotor. For the problem of brownout, however, the key issue is the suspension and vertical transport of sediment to heights that could impede the pilot’s visibility. The time-scale of this process is also of importance, and will dictate the rapidity at which the brownout dust cloud develops. Dual-phase flow visualization and PIV allowed for a detailed study of the mechanisms of vertical transport of entrained sediment, which was observed to correlate well with the upwash fields induced by the blade tip vortices.

### 4.3.1 Sediment Trapping in Vortices

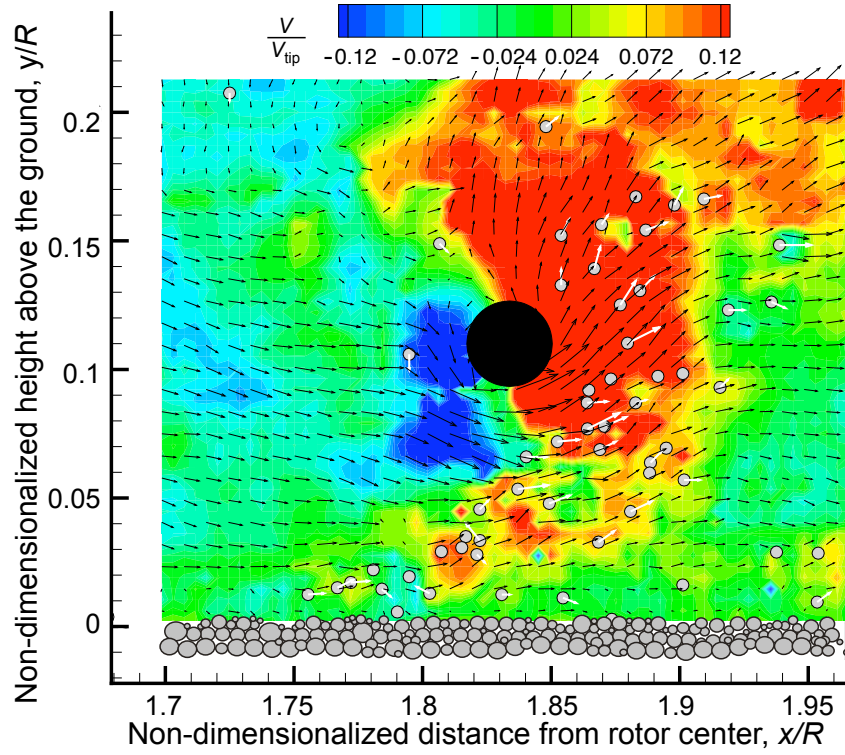
The primary mechanism responsible for the vertical transport of entrained sediment was observed to be the intermittent suspension or “trapping” of sediment within the strong upwash fields produced by the convecting blade tip vortices. Figure 4.5(a) clearly shows the dynamics of this process, where a significant concentration of sediment can be traced from the bedload region directly into the vortex core region (recognizable by the black seed void at its center). Figure 4.5(b) shows the corresponding dual-phase velocity field associated with this image, the color contours and vectors representing the normalized vertical flow velocity  $V/V_{\text{tip}}$ , and the grey circles and vectors representing the sediment particle locations and their corresponding velocities.

A clear correlation was seen between the sediment locations and the vortex induced velocity field, as almost all of the concentration of sediment is located within the upwash field (denoted by the red region in Fig. 4.5(b)). As a consequence of centrifugal and Coriolis acceleration effects, some particles have already spun out of the vortex flow, while many other particles have acquired noticeable radial velocities that are directed outwards from the vortex core.

Sediment trapping in vortices is a consequence of the powerful vertical component of the velocity field induced by a tip vortex as it reaches the ground. This effect increases the relative vertical velocity of the sediment well in excess of the normal settling velocity that would be associated with the weight and size of the particles. The sediment particles with small enough response times to respond to the sudden change in flow velocity caused by a convecting vortex can then become suspended or “trapped” in the vortex flow.



(a) Flow visualization of sediment trapping effect



(b) Dual-phase PIV image of sediment trapping

**Fig. 4.5: The upwash induced by convecting wake vortices is an important a mechanism for trapping sediment and uplifting it into the rotor flow.**

Sediment trapping in vortices is a well-known mechanism that influences the transport of coastal sediment (Refs. 25, 57–59). In an ideal case, assuming an isotropic vortex and ignoring particle accelerations, sediment trapping will occur if the maximum swirl velocity induced by the vortex,  $V_\theta$ , is greater than the settling velocity of the particle (Ref. 25, 58, and 59). For an airborne particle in equilibrium to be trapped in a vortex of maximum swirl velocity  $V_\theta$  then

$$V_\theta \geq V_s \quad (4.1)$$

This result is equivalent to that used in wind-erosion theory, which states that sediment will become suspended when the vertical component of velocity from turbulence is greater than or equal to the particle settling velocity (Eq. 1.13). In this case, the rotor wake vortices simply serve as flow elements that induce high enough vertical velocities to keep the sediment suspended in the flow rather than allowing it to fall back down to the bed under gravity.

By inserting Eq. 1.13 into Eq. 4.1, the sediment trapping effectiveness of a vortex flow can be directly related to the characteristics of the sediment particle and to the characteristics of the vortex. The criteria that must be satisfied for a particle in equilibrium with properties  $D_p$  and  $\rho_p$  to be trapped within a isotropic vortex of peak vertical swirl velocity  $V_\theta$  and fluid density  $\rho$  is then

$$V_\theta \geq \sqrt{\frac{4\rho_p g D_p}{3\rho C_D}} \quad (4.2)$$

Therefore, it can be seen that it is the strength of the vortices that will dictate the size distribution of the sediment that can be suspended by means of this trapping mechanism. It is apparent that with a full-scale helicopter (in which  $V_\theta$  will be an order of magnitude

higher than what it has been achieved in the present experiments), sediment will be much more prone to be suspended by the wake vortices. Furthermore, Eq. 4.2 provides some insight into the scaling relationships that must be considered in the study of brownout at laboratory scales (discussed more in Chapter 5).

It should be noted, however, that Eq. 4.1 is based on equilibrium assumptions, and do not account for the particle response time (given Eq. 1.11). For the case of rotor flow, the particle response time will play a key role in determining whether a given sediment

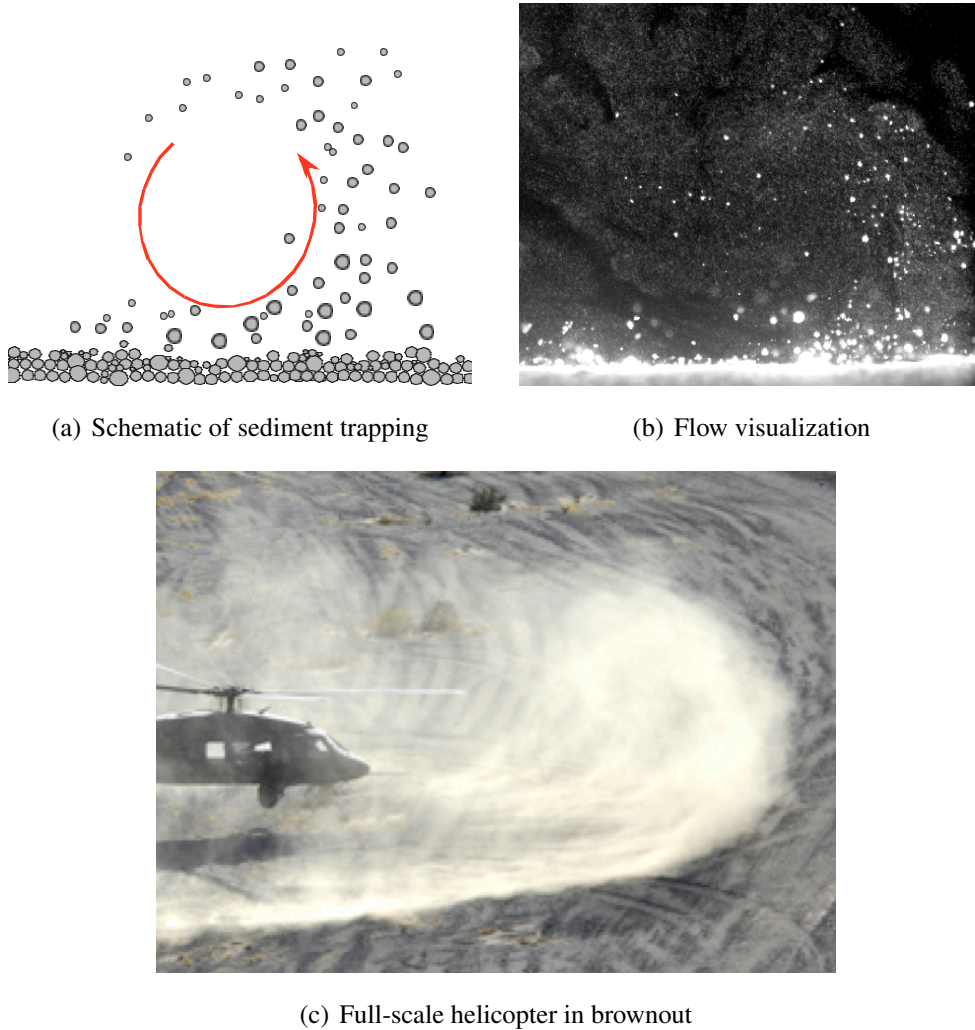


**Fig. 4.6: The upwash induced by the wake vorticity is an important mechanism for vertically transporting and suspending sediment.**

particle can be trapped and vertically transported by the vortical flow (discussed more in Section 4.3.2).

Despite the discrepancies in geometric scales, the sudden emission of zones of trapped sediment in the blade tip vortices was noted to correlate well with observations of the brownout phenomenon produced by full-scale helicopters. Specifically, the two-dimensional wave-crest profile observed during sediment trapping in the wake vortices (see Figs. 4.6(a) and 4.6(b)) is qualitatively very similar with the radially expanding wave profile seen at the front of the helicopter in Fig. 4.6(c).

#### 4.3.2 Sediment Transport by Merging Vortices

While individual blade tip vortices (like those shown in Fig. 4.3.1) were observed to trap significant quantities of sediment, the previously noted tendency of adjacent vortices in the rotor wake to roll-up and merge also played an important role in this trapping mechanism.

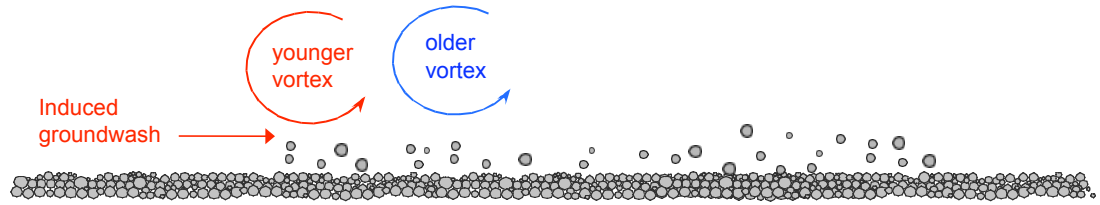
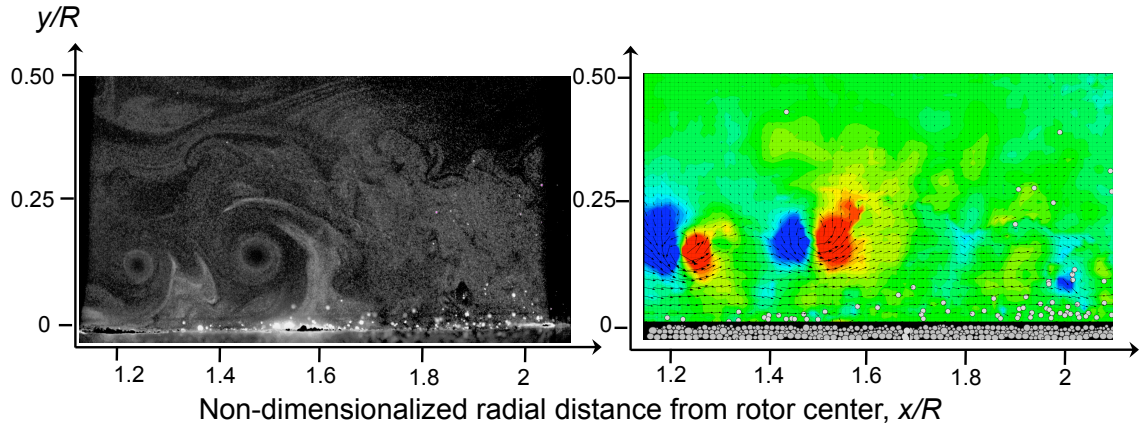
Figures 4.7(a) through 4.7(f) show the dynamics of this process, which depict a time-sequence of dual-phase flow visualization and corresponding dual-phase PIV images over a time scale of just under one full rotor revolution ( $\Delta\psi = 324^\circ$ ). The azimuthal position of the blade is given in each figure. Each dual-phase PIV image has contours of normalized vertical velocity  $V/V_{\text{tip}}$  (red regions denoting an upwash region, blue regions denoting a downwash region). The sediment particle locations are shown as grey circles. The sediment velocity vectors have been omitted in this case to avoid congesting the image. For clarity, schematics of the processes are given under each image. The sediment

bed in this case was formed using particles from Group A. The correlation between the vortex flow and the vertical transport of the sediment is evident.

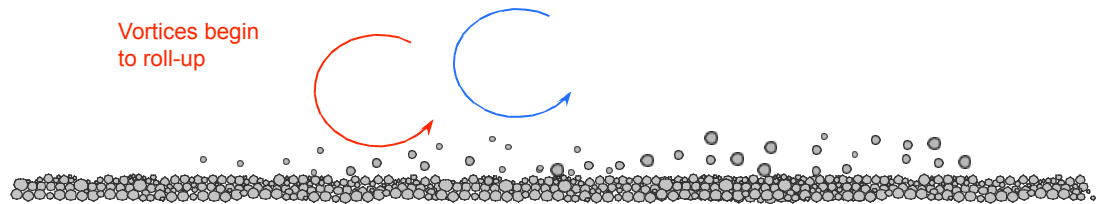
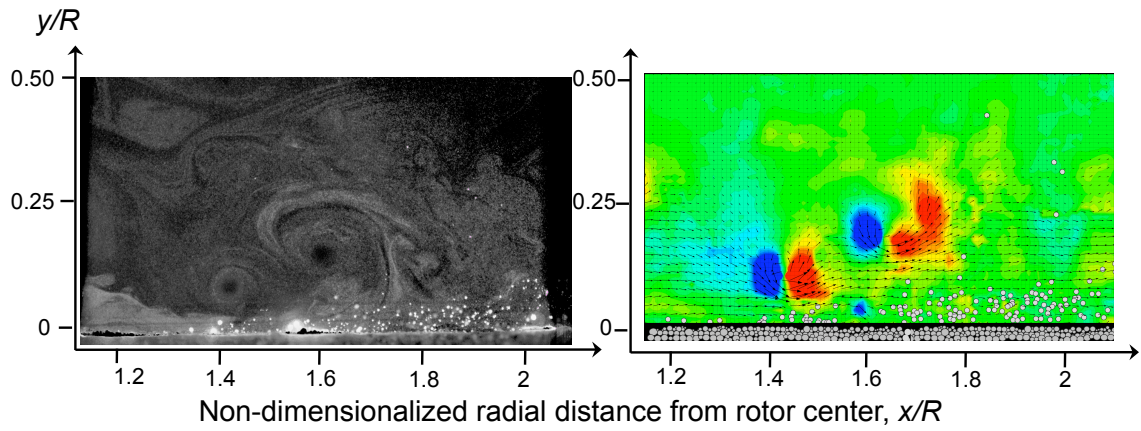
Figures 4.7(a) and 4.7(b) show the first two image sets in this sequence, and show the presence of two coherent vortices (labeled as younger and older based on their time in the flow after which they were generated at the rotor). These figures also show the presence of several uplifted sediment particles below the vortices, which have been aerodynamically entrained by the high groundwash induced by the vortices. At this point, the majority of these particles were still observed to be transported through bedload processes (i.e., saltation and creep).

Because of the relatively low helical pitch of the rotor wake, adjacent blade tip vortices pair with each other relatively easily (which is essentially an inviscid process), and soon merge (which is a viscous process) into a single vortical disturbance—as explained previously with the aid of Figs. 3.10 and 3.11. During the vortex merging, the younger vortex passes beneath the older vortex, causing its induced flow to penetrate the developing saltation layer with the bedload particles—see Figs. 4.7(b) and 4.7(c). This process served to trap significant quantities of airborne sediment, and also entrain new sediment particles directly from the bed.

The trapping process can specifically be visualized in Fig. 4.7(d), which shows an increased concentration of sediment at the crest of the upwash field. Figures 4.7(e) and 4.7(f) show the final two image sets in the sequence, and depict the sudden uplift of the trapped sediment in the upwash field induced by the merging vortices. Although this phenomena was not periodic, it was observed to be rather repetitive in nature, and it led to a high level of intermittency in the vertical transport of sediment from the bedload region.



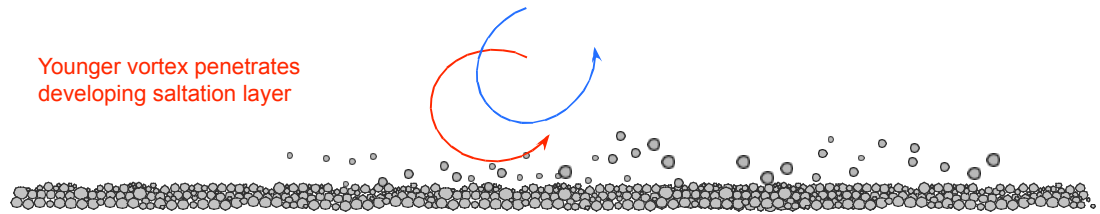
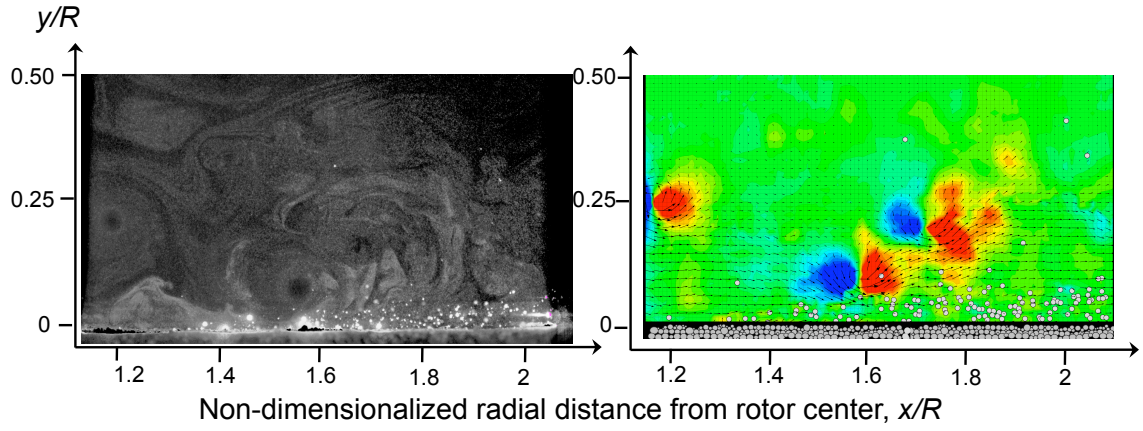
(a) Two vortices convecting across the ground:  $\psi = 152^\circ$



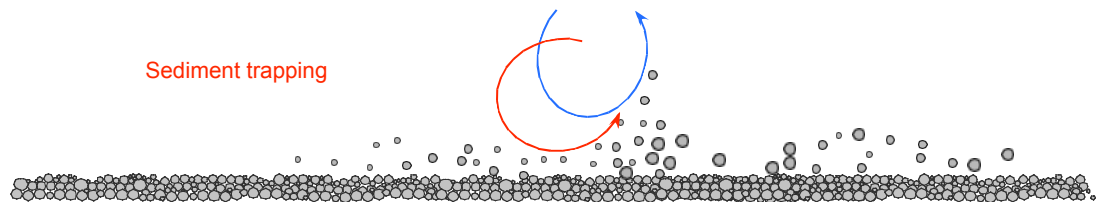
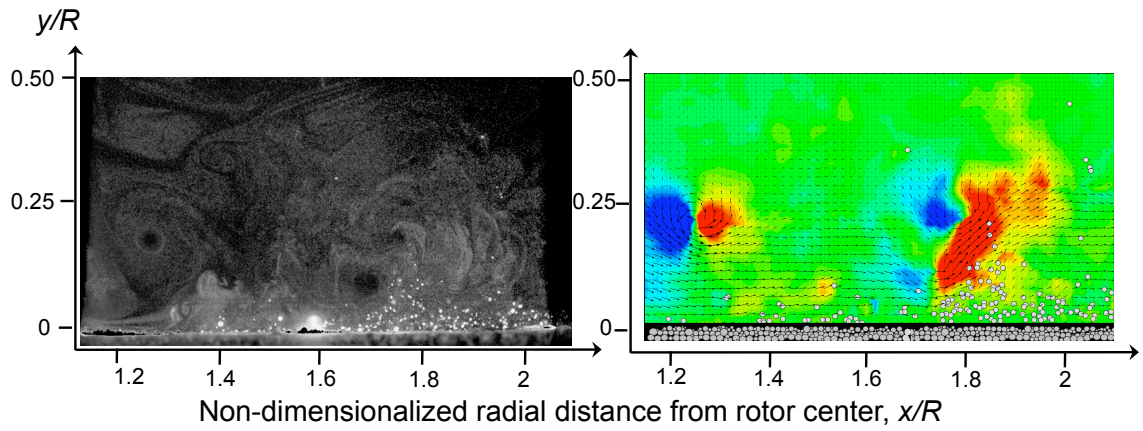
(b) Vortices begin to roll up:  $\psi = 242^\circ$

**Fig. 4.7: Two adjacent blade tip vortices begin to roll-up**



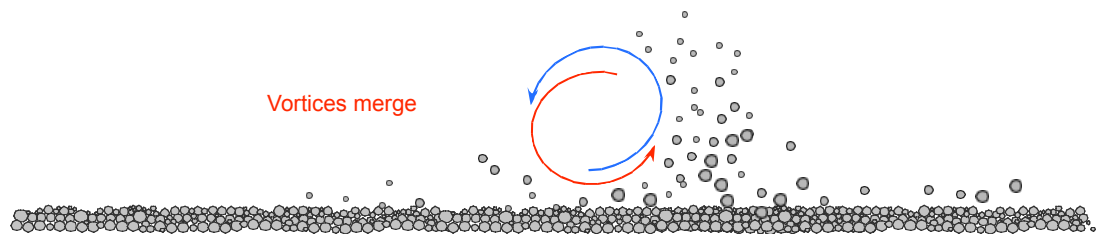
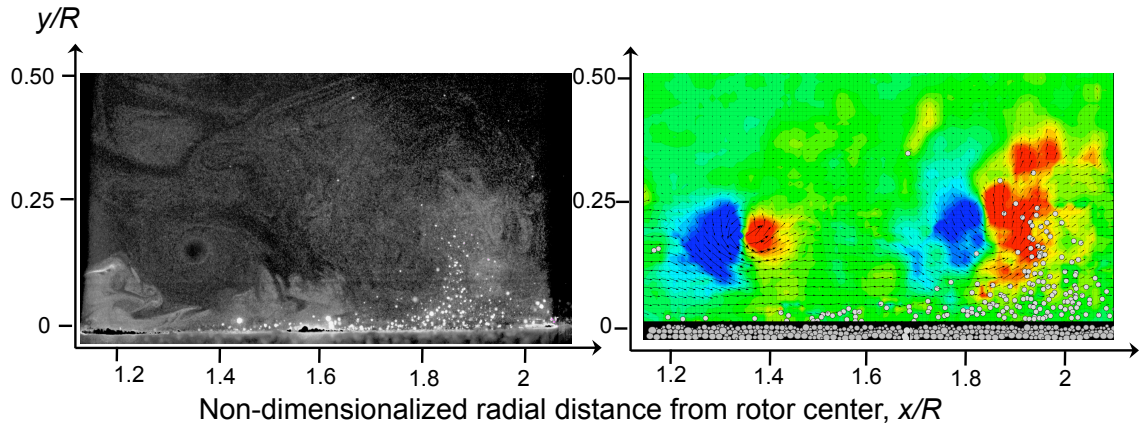


(c) Younger vortex penetrates the bedload region:  $\psi = 296^\circ$

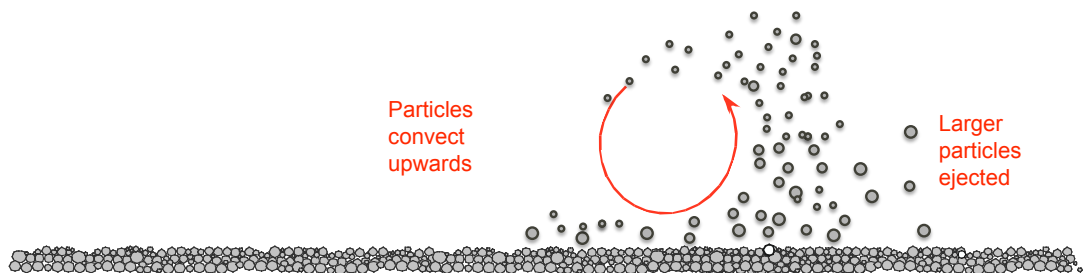
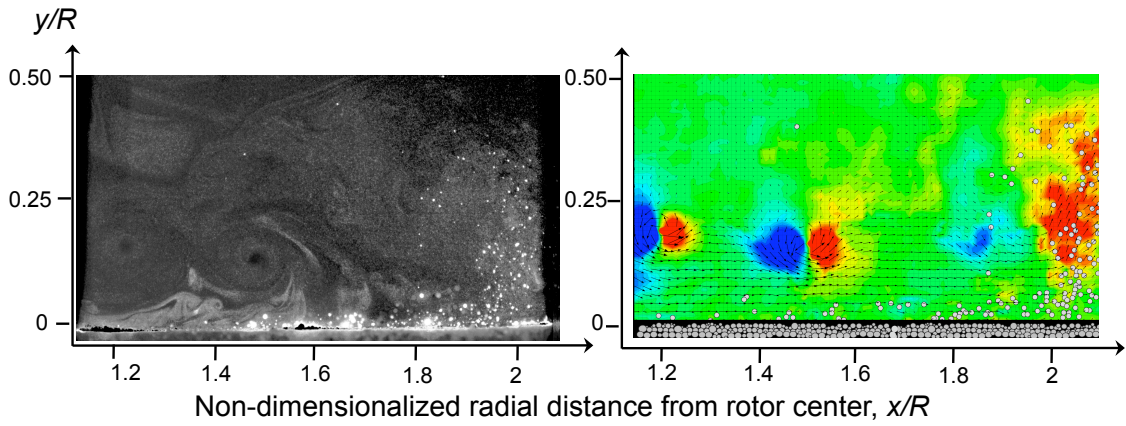


(d) Most airborne sediment trapped in the upwash region of younger vortex:  $\psi = 350^\circ$

**Fig. 4.7: (Continued): Roll-up of adjacent vortices, causing sediment trapping**



(e) Vortices merge into one coherent (larger) vortex:  $\psi = 44^\circ$



(f) Sediment convects vertically upwards in combined upwash region:  $\psi = 116^\circ$

**Fig. 4.7: (Concluded): Vertical transport of trapped sediment.**

Comparing the results in Fig. 4.7(f) (i.e., sediment trapping by a pair of merging vortices) with those in Fig. 4.5(b) (i.e., sediment trapping by a single tip vortex), it can be seen that the concentration of uplifted sediment particles was observed to be greater if and when vortex merging occurs. It can also be seen that the maximum height of the sediment particles in Fig. 4.7(f) was approximately double than those shown in Fig. 4.5(b), and is a direct result of the larger upwash region formed during vortex merging.

The results using particle Group B showed somewhat similar characteristics, although because of the larger particle inertia and particle response times, such particles were often observed to be centrifuged out away from the vortex before they could reach equilibrium with the vortex flow. Figure 4.8 shows a dual-phase flow visualization image, and identifies the general trend observed for Group B particles. Particle entrainment be-

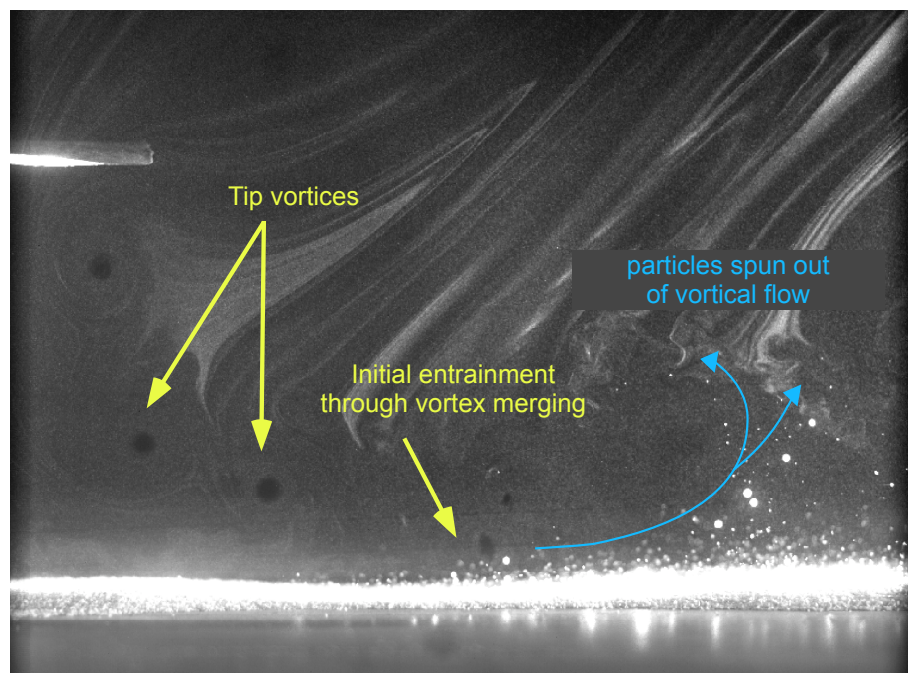


**Fig. 4.8: Larger particles were incapable of reaching equilibrium with the unsteady, vortical flow, causing them to spin out of the vortices.**

gan through the process of saltation at the periphery of the rotor disk. The strong upwash of the impinging vortices, however, served to interrupt this process and transport many bedload particles out of the developing saltation layer. Still, because of the high response times of Group B particles, they could not be fully trapped within the upwash field of the vortex, and instead fell back to the bed under gravity. The initial momentum gained from the vortex flow, however, served to change the trajectory of the particles greatly (shown in Fig. 4.8).

Specifically, the merging process was observed to occur over a time-scale of approximately one rotor revolution (which corresponds to 20 milliseconds). Because all particles in Group A possessed response times greater significantly higher than 20 milliseconds (the smallest response time for the range of Group A particles was 400 milliseconds), they could not be fully entrained by the vortex. On the contrary, the finest particles of Group A did possess response times under 20 milliseconds, allowing them to be trapped in the vortex flow and vertically transported in the upwash field.

#### 4.4 Consequences for Modeling

A significant consequence of sediment entrainment and trapping by the rotor wake vortices is the failure to develop an equilibrium saltation layer above the ground. Such saltation layers possess a constant (or equilibrium) mass flux,  $Q$ , of particles above the surface for a given value of bed shear stress (see Eq. 1.12). For brownout conditions, however, the distribution of shear stress is both nonuniform and unsteady as a result of the rotor wake and its embedded tip vortices, as shown previously in Figs. 3.3 and 3.5(a).

The corresponding unsteady momentum flux produced by the convecting vortices led to intermittent bursts of entrained sediment particles from the surface, this process being different to the more homogeneous particle fluxes that are typical of an equilibrium saltation layer.

In addition to the consequences the vortices have on the wall shear, sediment trapping in vortex induced upwash field was also observed to affect normal patterns of saltation. Specifically, the upwash served to increase the relative vertical velocities of the sediment well above what could be created in a one-dimensional flow. This led to sediment becoming intermittently suspended, or trapped, in the vortices, instead of proceeding in saltation. Even though the larger sediment particles possessed too large of response times to reach equilibrium with the highly unsteady vortical flow, often the subsequent increases in their momentum dramatically changed their subsequent saltation trajectories, as shown in Fig. 4.8.

Even for a steady uniform flow the cascading process of saltation and the subsequent emission of dust particles into the flow takes time to reach an equilibrium with the flow (Refs. 60 and 61). However, with the continual disruption of the saltation process and the boundary layer by the rotor wake and its vortex flow, the conditions needed for equilibrium are prevented. This fact is important because non-equilibrium particle mass fluxes have been measured to be different than equilibrium particle mass fluxes (Refs. 60 and 61). This brings into question the validity of using equilibrium saltation flux models (i.e., models for  $Q$ ) to simulate particle fluxes in brownout. Particle ejection through processes other than just saltation bombardment (such as that caused by the bombardment of recirculated particles seen in Fig. 4.4) will also affect the mass flux of sediment that is

produced above the sediment bed.

The disruption of normal saltation by the rotor wake also brings into question the validity of dust flux models (i.e., the quantity  $F$ ) for brownout problems, given that  $F$  is typically derived in terms of  $Q$ . Furthermore, such models for  $F$  have been derived from experiments in which homogenous (i.e., spatially invariant) turbulence is the only mechanism responsible for the vertical transport of dust from the saltation layer (Ref. 60). For a rotor flow, however, the dominant source of vertical flow velocities is produced by the convecting blade tip vortices, not by turbulence. This results in a spatially varying upwash field. The magnitude of this upwash field is also significantly larger than what could be produced by turbulence, the consequence being that more sediment is likely to be suspended in this case. Furthermore, the time-scales of the vertical transport of sediment by the rotor wake will be much shorter because the process of sediment trapping in blade tip vortices is predominately a convective mode of transport, not a diffusive one like turbulence. Because of this, sediment can be transported much more quickly and possibly to much greater heights than could normally be reached in more uniform turbulent flows, i.e., this process affects the rapidity at which the brownout cloud develops.

## 4.5 Summary

This chapter has shown experimental results analyzing the mechanisms of sediment entrainment and transport below a hovering rotor. In addition to the aerodynamic entrainment of particles through shear stress, some sediment were entrained through processes of bombardment, either from particles in saltation or from particles reingested into the rotor

wake. Once entrained, significant quantities of sediment were shown to be intermittently suspended (or trapped) by the vortex induced upwash field, which served as the dominant mechanism that was responsible for the vertical transport of sediment from the surface. This vertical transport of sediment was observed to be highly aperiodic and intermittent, leading to localized bursts of sediment into the flow. The observations made here in the small-scale experiments correlate qualitatively well with full-scale observations of sediment concentration levels in brownout conditions. A simple scaling relationship based on vortex strength and particle characteristics was also presented based on the concept of sediment trapping in vortices.

## Chapter 5

### Conclusions

The fundamental physics of sediment entrainment and transport below a small-scale rotor operating in ground effect were studied. Improved experimental methods and advanced particle image velocimetry (PIV) interrogation techniques allowed for high-resolution phase-resolved PIV measurements to be made in the unsteady boundary layer flow at the ground. Time-resolved PIV, combined with dual-phase flow visualization and dual-phase PIV, were used to clearly identify both the mechanisms responsible for sediment entrainment and the mechanisms responsible for the vertical transport and suspension of sediment by the rotor flow.

#### 5.1 Mechanisms of Sediment Entrainment

The process of sediment pickup or entrainment in brownout was observed to be dependent upon both the forces imparted to the sediment bed by rotor flow, and the forces imparted by the process of bombardment. Both processes required a close examination of the flow induced by the rotor near the ground using single-phase and dual-phase flow visualization, as well as PIV. The following conclusions were derived from the work.

1. The maximum groundwash velocities were observed beneath the convecting rotor wake vortices. The high level of groundwash beneath the vortices was often observed to increase the wall-normal velocity gradient approaching the ground.



The highest bed erosion rates were additionally observed in the region of vortex impingement on the ground. These observations suggest the wall shear increases because of the additional velocities induced by the wake vortices.

2. High-resolution flow measurements revealed significant spatial and temporal excursions in the surface boundary layer profiles that developed beneath the wake vortices as they impinged upon the ground. Regions of localized flow separation downstream of the vortices were observed to accompany this process. This has been attributed to the formation of an adverse pressure gradient in the boundary layer.
3. High levels of aperiodicity were observed in the flow near the ground, mainly because of the mutual interaction between adjacent blade tip vortices. Time-resolved flow visualization and PIV revealed the main cause of this was tendency of adjacent vortices to roll-up and merge. While this process continually repeated itself, it was not a periodic phenomena. This led to a large deviation in the phase-resolved locations of the blade tip vortices with respect to the mean vortex trajectory. The high level of aperiodicity specifically served to make the quantitative measurement of the wall shear and Reynolds stresses in the boundary layer impractical for the current experimental setup.
4. Multiple forms of bombardment by sediment particles was observed in the dual-phase experiments. Larger particles, which were not so easily suspended in the flow, were observed to eject new particles through the classical mechanism of saltation bombardment. Smaller particles that became trapped and suspended in the vortical

rotor flow were sometimes observed to be recirculated into the wake. Recirculated sediment particles were convected toward the ground at relatively high speeds, subsequently ejecting new particles through the process of reingestion bombardment.

## 5.2 Sediment Transport and Suspension

Time-resolved dual-phase flow visualization and PIV results allowed for a fundamental understanding of the transport of entrained sediment by the rotor flow. A clear correlation was observed between the vertical transport of sediment and the non-uniform upwash fields induced by the wake vortices. The following specific conclusions were derived based on the observations of the flow:

1. The transport of entrained sediment in the rotor flow was observed to occur both through the classical process of saltation and through the intermittent suspension (or trapping) of sediment in the non-uniform upwash fields induced by the convecting wake vortices. The blade tip vortices were specifically observed to be the dominant mechanism responsible for the vertical transport of sediment. Larger sediment particles were often spun out of the vortical flow, or completely resist trapping because of their higher inertia and particle response times. The momentum gained from the induced flow of the vortices, however, served to affect significantly the height and length scales of the saltation trajectories.
2. The aperiodic roll-up and merging of adjacent wake vortices was seen to strengthen the local upwash field significantly, and also to rapidly increase the concentration of airborne sediment through the trapping mechanism. The roll-up phenomena had

the effect of bringing the vortex induced velocity field into the region of bedload transport, increasing both the groundwash and upwash velocities. Compared to sediment trapping by a single vortex, however, trapping through the roll-up and merging of vortices was observed to rapidly increase the concentration of airborne sediment particles, as well as the maximum height above the ground to which the sediment was transported.

### 5.3 Suggestions for Future Work

From the results obtained, a good qualitative understanding of many of the processes associated with sediment entrainment and transport in rotor flows was obtained. From an experimental standpoint, the main effort in going forward is to produce more controllable, repeatable experiments, such that better quantitative measures can be obtained of these processes. Three key areas of improvement to future experimental studies include: 1) Controlling aperiodicity in the flow, 2) improved dual-phase measurement techniques, and 3) addressing possible scaling issues. A discussion of each of these issues is given in the following sections.

#### 5.3.1 Controlling Flow Aperiodicity

The main challenge in trying to extract shear stress measurements near the ground was reducing and/or controlling aperiodicity in the flow, as discussed in Chapter 3. Ultimately, the interaction between adjacent vortices is a key factor in determining the aperiodicity levels in the flow. For the present work, a two-bladed rotor setup was used for

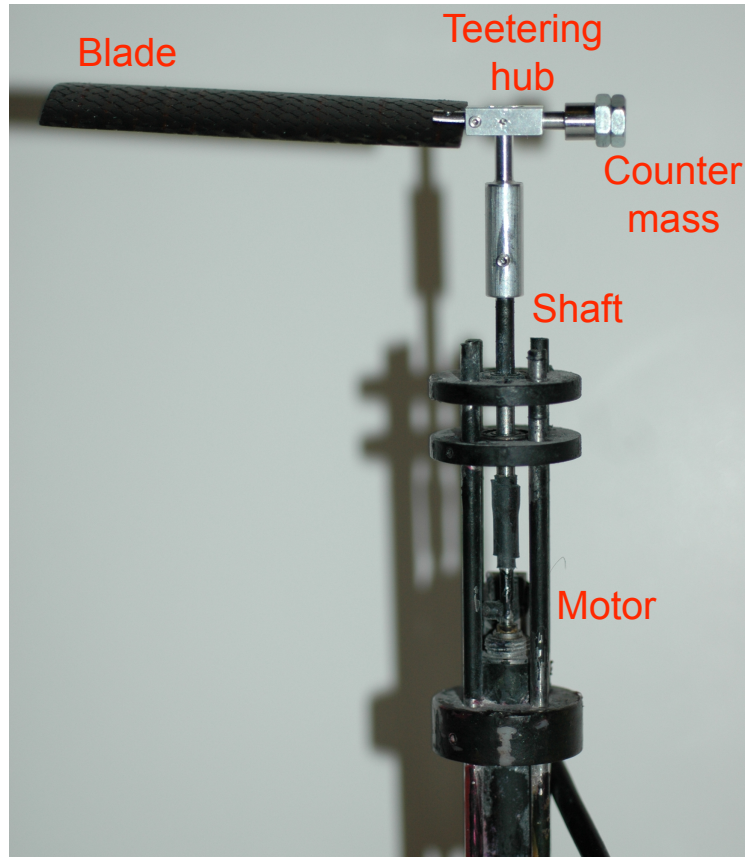


**Fig. 5.1: One-bladed rotor setup proposed for future work.**

all of the experiments. One possible way to produce more periodic flows is to reduce the number of blades on the rotor, so as to give a single helicoidal vortex filament in the wake.

For this reason, a teetering one-bladed rotor system has been developed (see Fig. 5.1), and will be used in future tests. The rotor itself employs a counterweight opposite the blade to balance the rotor, and a teetering hinge such that the blade can naturally flap during its rotation. From a flow measurements perspective, the one-bladed rotor design also is advantageous over multiple-bladed rotor designs because multiple blades do not need to be tracked. It is known that even small discrepancies in the pitch angle between the blades can be a source of some of the aperiodic flow (Ref. 48).

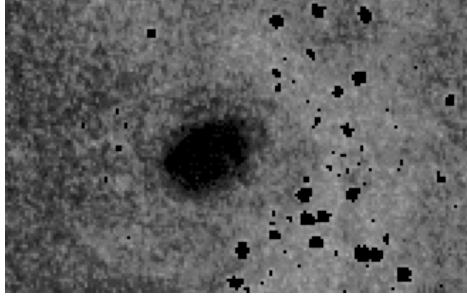
### 5.3.2 Improved Dual-Phase Techniques

While the thresholding technique used in the present work has the advantage of being relatively simple compared to other phase discrimination techniques, the current methodology has its limitations. One significant improvement that should be made for future measurements is in the cross-correlation of the carrier phase images (e.g., see Fig. 5.2(a)), specifically around the void spaces left by the removed sediment particle images. Currently, the phase-discrimination software used inserts pixels of zero intensity into these spaces, which produces a bias that is not ideal for typical cross-correlation.

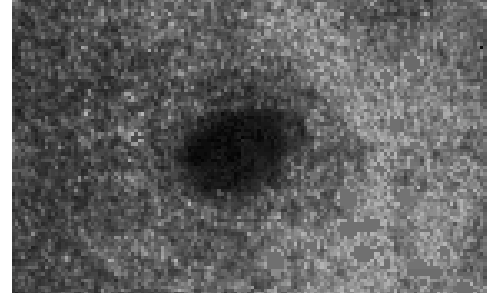
Examining the cross-correlation function in the spatial domain for an  $N$  by  $N$  correlation window size, the cross-correlation coefficient  $\phi$  for an integer displacement  $(m, n)$  between the intensity distributions  $I_a$  and  $I_b$  of the two PIV images will be given by

$$\phi(m, n) = \frac{\sum_{i=0, j=0}^{NxN} (I_a(i, j) - \bar{I}_a)(I_b(i + m, j + n) - \bar{I}_b)}{\sqrt{\sum_{i=0, j=0}^{NxN} (I_a(i, j) - \bar{I}_a)^2 \sum_{i=0, j=0}^{NxN} (I_b(i + m, j + n) - \bar{I}_b)^2}} \quad (5.1)$$

where  $\bar{I}_a$  and  $\bar{I}_b$  are the mean intensities in the reference and displaced windows, respectively. Understandably, if multiple pixels within the correlation window have greyscale intensities of zero, the overall mean intensity within the window will be biased towards zero. Therefore, there will be some level of bias in the final cross-correlation coefficient. In addition to that, multiple zero exposure pixels within an interrogation window can result in a correlation of holes, reducing the probability of peak detection (Ref. 62). Possible ways to alleviate this are to fill in the sediment particle images with a local mean greyscale value instead of filling in the removed sediment particle images with zero intensity pixels (see Fig. 5.2). Completely removing pixels with zero intensity from the cross-correlation calculation will also eliminate this bias.



(a) Zero intensity masking



(b) Local mean intensity masking

**Fig. 5.2: Comparison of masking techniques for carrier phase image processing.**

### 5.3.3 Scaling Issues

While the simulation of full-scale brownout conditions in a small-scale experiment is certainly important, the proper scaling of every possible dimensional parameter governing brownout is unrealistic. Not only do the aerodynamic scaling parameters (i.e., the flow Reynolds, Mach, etc.) come into play, but proper scaling of the forces on the individual sediment particles must also be considered. Greeley & Iversen (Ref. 11), for example, showed that up to 12 different scaling parameters should be examined for a proper experimental simulation of sediment entrainment and transport. Some assumptions, however, are always required to simplify the problem for practical experiments to be conducted.

One key contribution of the present work was the observation that the wake vortices were the primary mechanism of vertical transport and suspension by the rotor flow. This led to the simple parameter in Eq. 4.2, which can help to scale the suspension process. While Eq. 4.2 can be used as a reference for scaling forces on particles after they are airborne, the scaling of the entrainment process should also be considered. This latter process depends upon the threshold condition for the sediment bed and the shear stress imparted by the flow. For the current work, the determination of the shear stress imparted

by the flow was difficult, in part given the relatively high aperiodicity in the flow.

Ultimately, more controlled experiments may help in the determination of additional scaling parameters. The main contribution of the present work, however, was the visualization of the actual fluid dynamic processes associated with the development of rotorcraft brownout. The understanding of these processes have formed a baseline for future experimental brownout studies.

## Appendix A

### PIV Measurements Near Interfaces

The challenges in establishing reliable cross-correlations from PIV images made near an interface are summarized in Ref. 46 and include: 1) The presence of non-uniform laser reflections; 2) Signal truncation; 3) A high wall-normal velocity gradient; 4) Vector relocation when correlation windows overlap the interface.

#### A.1 Techniques to Reduce Laser Reflections

Because PIV cross-correlation procedures match patterns in pixel intensities to determine particle displacements, the presence of non-uniform intensity patterns from laser reflections can adversely contaminate the correlation process. This results in poor signal-to-noise ratios and erroneous velocity estimates. For example, Fig. A.1(a) shows a raw PIV image sample that overlaps the interface region. In this case, the interface is contaminated with pixels of much higher greyscale values than those of the tracer particles.

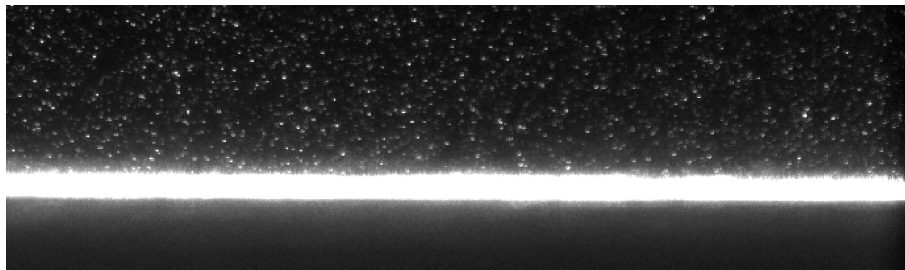
When standard cross correlation methods are used, each high intensity pixel at the interface will correlate well with every other high intensity pixel. Consequently, a completely biased correlation map will be produced, with correlation peaks running parallel to the direction of the interface—see Fig. A.2. Instead of providing one distinct correlation peak at the true particle displacement, this effect leads to spurious velocity vectors.

Even in regions where the reflections are less intense (see Fig. A.1(b)) the flow

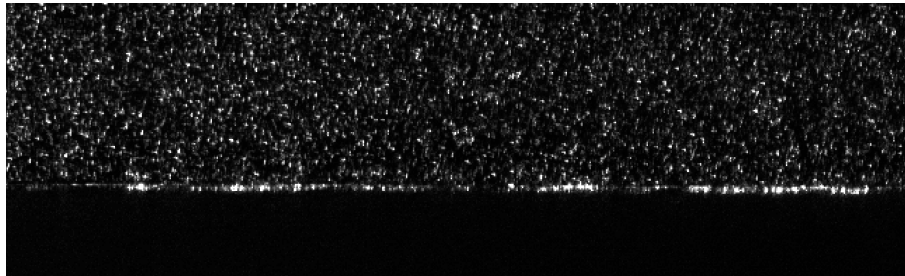


measurements made there will still be biased toward zero velocity. This is because cross-correlation algorithms cannot differentiate between the signals produced from tracer particles or from laser reflections. Because the pixel regions affected by laser reflections generally do not change much from the first PIV frame to the second, they are essentially registered as tracer particles with zero displacements.

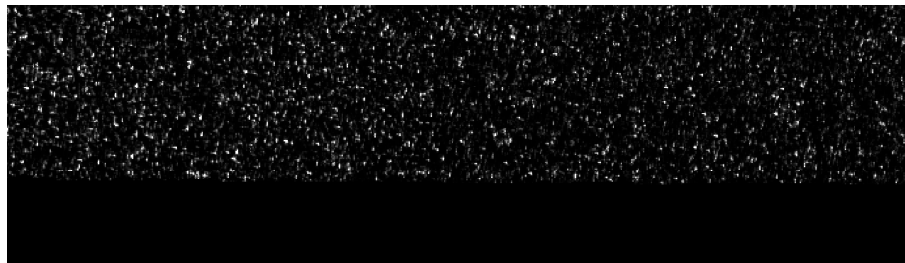
To reduce the intensity of laser reflections in the present work, a Rhodamine 6G



(a) Unaltered experiment



(b) Improvement through experimental techniques



(c) Improvement through background subtraction and masking

**Fig. A.1: Improvement in near-ground PIV interrogation through experimental and image pre-processing techniques.**

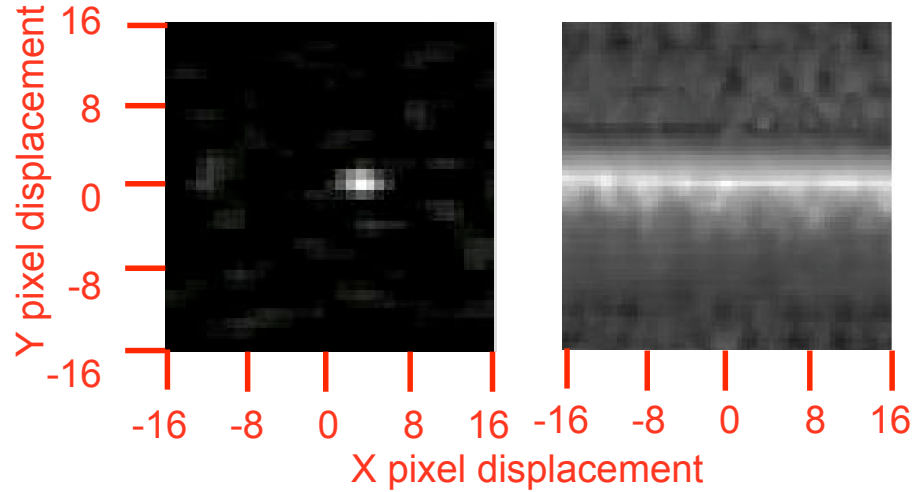


**Fig. A.2: Example of a normal correlation map, and one contaminated by laser reflections.**

fluorescent paint was applied to the ground plane. This paint shifted the wavelength of the reflected laser light from 532 nm to 590 nm. A 532 nm notch filter was then placed in front of the camera such that the high intensity reflected light (now mostly at 590 nm) was filtered out. A second approach used to reduce surface reflections was to simply align the laser sheet so that the incident light rays were more parallel to the interface.

After acquisition, the images were pre-processed with a background subtraction technique—see Ref. 63. A binary mask image was created in which each pixel was assigned a "0" or "1" based on its spatial location; all pixels in the flow area were given a value of 1, and all pixels in the interface were given a value of 0. This binary mask was then multiplied with each instantaneous PIV image such that all pixels in the interface ended up with zero intensity.

The overall improvement in the raw images after Rhodamine treatment, background subtraction, and binary mask generation is shown in Fig. A.1(c). These techniques al-

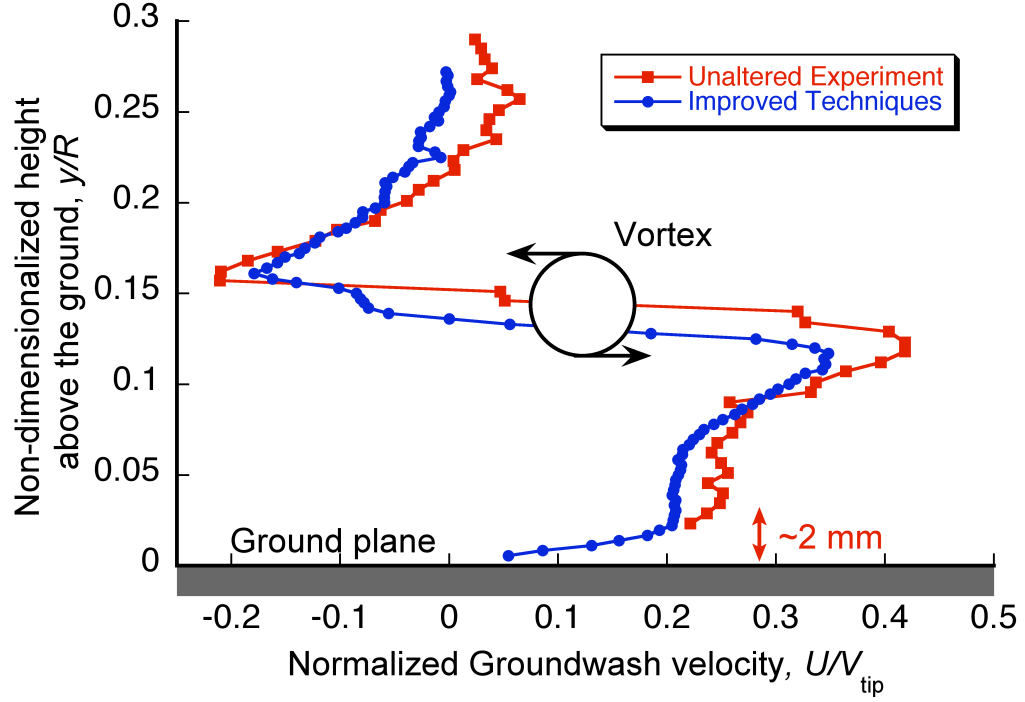


**Fig. A.3: Improved experimental technique and refined image processing allowed the flow to be successfully measured well into the boundary layer region.**

lowed velocity measurements to be made approximately 2 mm closer to the surface compared to what was possible by not using these methods—see the velocity profiles in Fig. A.3. The differences in the velocities away from the wall arise because the two instantaneous measurements shown are not temporally correlated, and not because of any artificial contamination of the raw images because of the implementation of these methods.

## A.2 Image Processing

To obtain the flow velocities from two PIV image pairs, the image must be divided into thousands of small interrogation windows. Intensity patterns in corresponding cor-

relation windows are then matched to measure the average particle displacements within each set of windows.

In the present work, challenges arise in determining the optimal cross-correlation algorithms and grids to measure the particle displacements. Specifically, the flows generated by a rotor operating near the ground interface produces high shear within the vortex cores and also inside the boundary layer that develops on the interface.

To help improve the measurement resolution and fidelity in these two regions, two separate processing grids were used for each PIV image pair: one for the boundary layer flow, and one for the remainder of the flow where the dominant coherent structures were the wake vortices.

The first processing grid was used to improve the fidelity of the flow measurements near the ground, which was based on suggestions given by Theunissen et al. (Ref. 46). In the boundary layer, the largest gradient exists in the wall-normal direction, so measurements with good spatial resolution are needed to resolve these gradients. A simple approach is to decrease the size of the individual correlation windows, and so to derive a larger number of independent measurement points. This process, however, limits the number of tracer particles present in each window and may deteriorate the cross-correlation procedure.

To compensate for this effect, the aspect ratio of the interrogation windows can be increased such that their dimensions parallel to the interface are extended, while their dimensions normal to the interface are reduced—see Fig. A.4. This allows the boundary layer to be sampled at a higher spatial resolution in the wall-normal direction, while still maintaining a sufficient number of tracer particles in the individual windows. Ad-

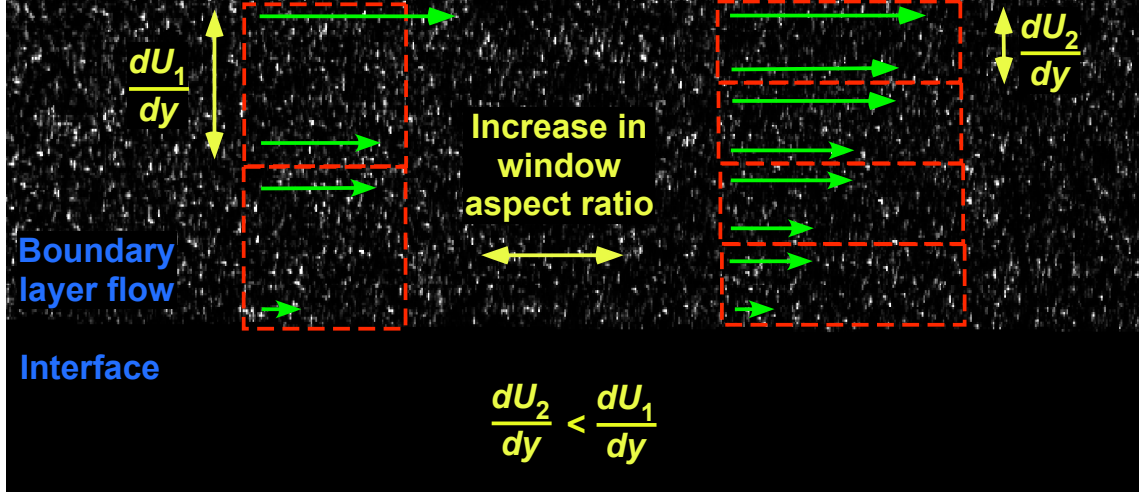


**Fig. A.4: Increasing the aspect ratio of the PIV interrogation window reduces velocity gradient bias errors in the wall-normal direction.**

ditionally, correlation windows with the smaller wall-normal dimensions will decrease the velocity gradient bias errors. This is because the variations of individual tracer particle displacements decrease within the windows when using smaller windows. Figure A.4 shows this approach for both standard square interrogation windows and for the deformed rectangular windows. Because the dimension of the rectangular windows in the wall-normal direction has been decreased, the discrepancies in the flow velocity (shown by the green velocity vectors) from the top of the window to the bottom window are also decreased.

The final dimension of the windows chosen for the boundary layer grid was 48-by-8 pixels. This grid allowed for over 97% of the vectors to pass with a signal-to-noise ratio of 1.5, while also giving the maximum spatial resolution in the wall-normal direction. The cross-correlation was then performed using a two-step recursive technique in which the integer pixel displacement  $(m, n)$  was estimated in the first processing pass.

The correlation windows were then offset about their geometric center by values  $m/2$  and  $n/2$  before starting a second processing pass. This two-pass technique has been shown to significantly improve the signal-to-noise ratio of the measurements (Ref. 64). This grid was extended to 1.5 mm above the surface (below which the most substantial values of  $dU/dy$  were measured), and then combined with a deformation grid above for the remaining flow, the latter which is optimal for velocity measurements within the wake vortices (see Appendix B).

Even if the effects of non-uniform laser reflections are removed by experimental techniques or by suitable pre-processing, a signal truncation issue still exists at the interface. As discussed by Theunissen and Ronneberger (Refs. 46 and 65), this discontinuity in pixel intensity is non-optimal for the preferred Fast-Fourier Transform (FFT) processing techniques because the signal resulting from the image pattern is no longer periodic. Additionally, when the correlation window overlaps the interface, the final vector placement

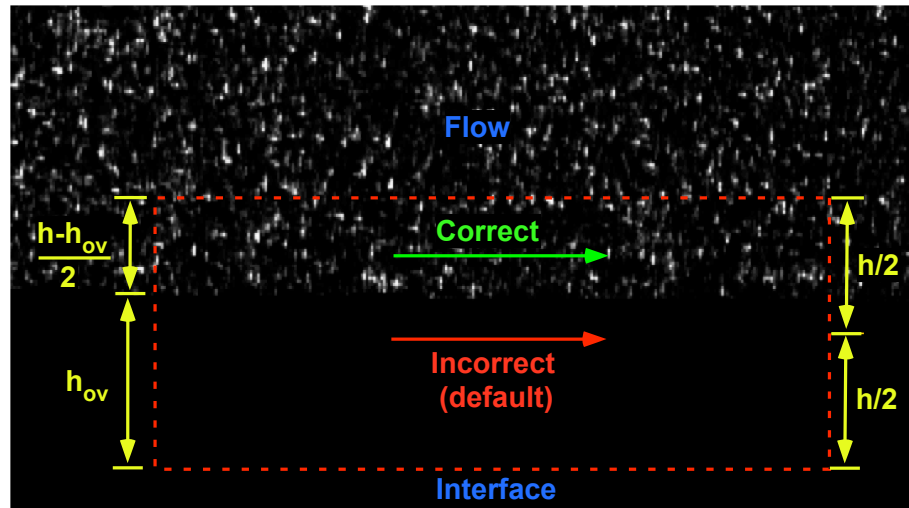


**Fig. A.5: Vector relocation is required whenever the interrogation windows overlap the interface.**

is spatially incorrect. By default, PIV processing algorithms generally place vectors at the center of the interrogation window. For a window overlapping the interface, however, the center of the correlation window will not coincide with the center of the truncated seeded region (see Fig. A.5). Therefore, any vector estimated from a correlation window with overlap must be mathematically adjusted such that its final location coincides with the center of the seeded region (Refs. 46 and 66). To eliminate such problems, the grid was defined such that the bottom of the first correlation windows were anchored at the interface, and arranged such that no windows mutually overlapped this interface.

## Appendix B

### Deformation Grid Algorithm

For TR-PIV processing in general, and for PR-PIV processing above the boundary layer region, the images were processed with a multi-step deformation grid cross-correlation procedure (Ref. 67), as also described in Ref. 44. This procedure is optimized to measure vortical flows and other flows with steep velocity gradients.

The first step in the process is similar to that of a simple recursive technique, however, at the second step the second window is deformed (i.e., it is both sheared and translated instead of just the simple translation)—see Fig. B.1. The procedure starts with the correlation of an interrogation window of a defined size (say, 64-by-64), which serves

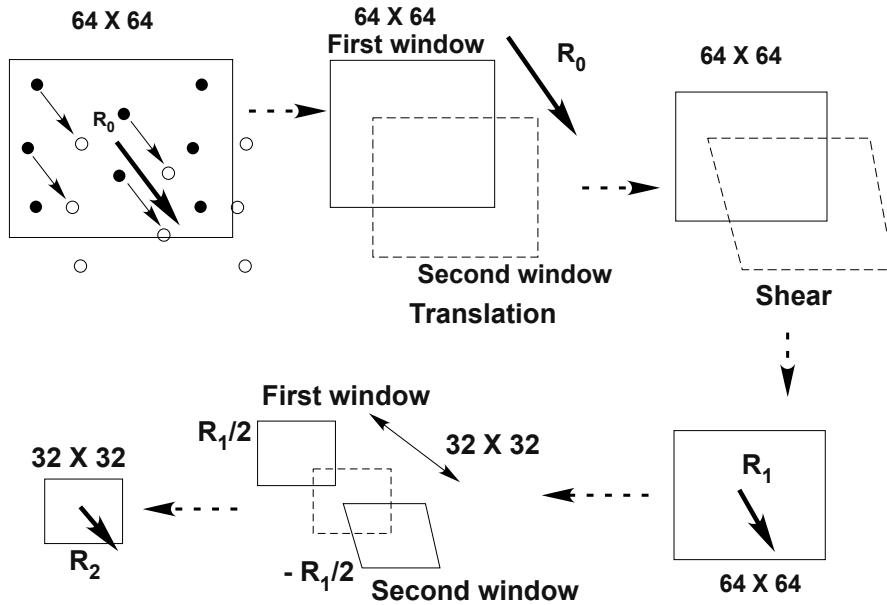


**Fig. B.1:** Schematic showing the basis of the deformation grid technique.



as the first iteration. Once the mean displacement of that region is estimated, the interrogation window of the displaced image is displaced by integer pixel values for better correlation in the second iteration. This third iteration starts by moving the interrogation window of the displaced image by sub-pixel values based on the displacement estimated from second iteration. Following this, the interrogation window is sheared twice (for integer and sub-pixel values) based on the velocity magnitudes from the neighboring nodes before performing fourth and fifth iteration, respectively.

Once the velocity is estimated after these five iterations, the window is split into four equal windows. These windows are moved by the average displacement estimated from the final iteration before starting the first iteration at this resolution. This procedure can be continued until the resolution required to resolve the flow field is reached. The second interrogation window is deformed until the particles remain at the same location after correlation.

## Bibliography

- [1] Mapes, P., Kent, R., and Wood, R., “DoD Helicopter Mishaps FY85–05: Findings and Recommendations,” USAF, DoD, Documents: AFRL-WS 06-2221, AFRL-WS 07-0731, AFRL-WS 07-1099, AFRL-WS 07-1100, SAM-GE-BR-JA-2008-0009.
- [2] Jansen, C., Wennemers, A., and Groen, E., “FlyTact: A Tactile Display Improves a Helicopter Pilots Landing Performance in Degraded Visual Environments,” *Haptics: Perception, Devices and Scenarios*, Vol. 5024, 2008, pp. 867–875
- [3] Brennen, C. E., *Fundamentals of Multiphase Flow*, Cambridge University Press, New York, NY, 2005, Ch. 1.
- [4] Wenren, Y., Walter, J., Fan, M., and Steinhoff, J., “Vorticity Confinement and Advanced Rendering to Compute and Visualize Complex Flows,” AIAA Paper 2006-945, 44th AIAA Aerospace Sciences Meeting and Exhibit Reno, Nevada, January 9–12, 2006.
- [5] Ryerson, C. C., Haehnel, R. B., Koenig, G. G., and Moulton, M. A., “Visibility Enhancement in Rotorwash Clouds,” AIAA Paper 2005-263, 43rd AIAA Aerospace Sciences Meeting and Exhibit, Reno, NV, January 10–13, 2005.
- [6] Haehnel, R. B., Moulton, M. A., Wenren, W., and Steinhoff, J., “A Model to Simulate Rotorcraft-Induced Brownout,” Proceedings of the 64th Annual Forum of the American Helicopter Society, Montréal, Canada, April 29–May 1, 2008.
- [7] Phillips, C., and Brown, R., “Eulerian Simulation of the Fluid Dynamics of Helicopter Brownout,” Proceedings of the 64th Annual Forum of the American Helicopter Society, Montréal, Canada, April 29–May 1, 2008.
- [8] Nathan, N. D., and Green R. B., “Measurements of a Rotor Flow in Ground Effect and Visualisation of the Brown-out Phenomenon,” Proceedings of the 64th Annual Forum of the American Helicopter Society, Montréal, Canada, April 29-May 1, 2008.
- [9] Bagnold, R. A., “Direct Numerical Simulation of Particle-Laden Rotating Turbulent Channel Flow,” *Physics of Fluids*, Vol. 13, No. 8, August, 2001, pp. 2320–2337.
- [10] Bagnold, R. A., *The Physics of Blown Sand and Desert Dunes*, Dover Publications, Inc., Mineola, NY, 1941.

- [11] Greeley, R., and Iversen, J. D., *Wind as a Geological Process on Earth, Mars, Venus, and Titan*, Cambridge University Press, New York, NY, 1985, Ch. 3.
- [12] Greeley, R., Iversen, J. D., Marshall, J. R., and Pollack, J. B., “Aeolian Saltation Threshold: the Effect of Density Ratio,” *Sedimentology*, Vol. 34, (4), 1987, pp. 699–706.
- [13] Shao Y., and Lu, H., “A Simple Expression for Wind Erosion Threshold Friction Velocity,” *Journal of Geophysical Research*, Vol. 105, (D17), 2001, pp. 22,437–22,443.
- [14] Iversen, J. D., Pollack, J. B., Greeley, R., and White, R. B., “Saltation Threshold on Mars: The Effect of Interparticle Force, Surface Roughness, and Low Atmospheric Density,” *Icarus*, Vol. 29, (3), 1976, pp. 381–393.
- [15] Iversen, J. D., Pollack, J. B., Greeley, R., and White, R. B., “Saltation Threshold on Earth, Mars, and Venus,” *Sedimentology*, Vol. 29, 1982, pp. 111–119.
- [16] Gillette, D. A., “Tests With a Portable Wind Tunnel for Determining Wind Erosion Threshold Velocities,” *Atmospheric Environment*, Vol. 12, (12), 1978, pp. 2309–2313.
- [17] Gillette, D. A., Adams, J., Endo, A., Smith, D., and Kihl, R., “Threshold Velocities for Input of Soil Particles into the Air by Desert Soils,” *Journal of Geophysical Research*, Vol. 85, (C10), October, 1980, pp. 5621–5630.
- [18] Gillette, D. A., Adams, J., Muhs, and Kihl, R., “Threshold Friction Velocities and Rupture Moduli for Crusted Desert Soil for the Input of Solid Particles Into the Air,” *Journal of Geophysical Research*, Vol. 87, (C11), 1982, pp. 9003–9015.
- [19] Gillette, D. A., “Threshold Friction Velocities for Dust Production for Agricultural Soils,” *Journal of Geophysical Research*, Vol. 93, (D10), 1988, pp. 12,645–12,662.
- [20] Saffman, P. G., “The Lift on a Small Sphere in a Shear Flow,” *Journal of Fluid Mechanics*, Vol. 22, No. 2, June, 1965, pp. 385–400.
- [21] Crowe, C., Sommerfeld, M., Tsuji, Y., *Multiphase Flow Handbook*, CRC Press, Boca Raton, FL, 1998, Ch. 2–4.

- [22] Owen, P. R., “Saltation of Uniform Grains in Air,” *Journal of Fluid Mechanics*, Vol. 20, (2), 1964, pp. 225–242.
- [23] Shao, Y., Raupach, M. R., and Findlater, P. A., “Effect of Saltation Bombardment on the Entrainment of Dust by Wind,” *Transactions of the American Society of Agricultural Engineers*, Vol. 98, (D7), 1993, pp. 12,719–12,726.
- [24] Gillette, D. A., “Production of Dust That May Be Carried Great Distances,” Geological Society of America, Special Publication No. 186, 1981, pp. 11–26.
- [25] Nielsen, P., *Coastal Bottom Boundary Layers and Sediment Transport*, Vol. 4, World Scientific, Hackensack, NJ, 1992, Ch. 4–5.
- [26] Marticorena, B., and Bergametti, G., “Modeling the Atmospheric Dust Cycle: 1. Design of a Soil-Derived Dust Emission Scheme,” *Journal of Geophysical Research*, Vol. 100, (D8), 1988, pp. 16,415–16,430.
- [27] Lu, H., and Shao, Y., “A New Model for Dust Emission by Saltation Bombardment,” *Journal of Geophysical Research*, Vol. 104, (D14), 1999, pp. 16,827–16,842.
- [28] Shao, Y., “Simplification of a Dust Emission Scheme and Comparison with Data,” *Journal of Geophysical Research*, Vol. 109, (D10202), 2004, pp. 1–6.
- [29] Alfaro, S. C., Gaudichet, A., Gomes, L., and Maille, M., “Modeling the Size Distribution of a Soil Aerosol Produced by Sandblasting,” *Journal of Geophysical Research*, Vol. 102, (D10), 1997, pp. 11,239–11,249.
- [30] Alfaro, S. C., and Gomes, L., “Modeling Mineral Aerosol Production by Wind Erosion: Emission Intensities and Aerosol Size Distributions in Source Areas,” *Journal of Geophysical Research*, Vol. 106, (D16), 2001, pp. 18,075–18,084.
- [31] Leishman, J. G., *Principles of Helicopter Aerodynamics*, Cambridge University Press, 2006, Cambridge, UK, Ch. 5.
- [32] Lee, T. E., Leishman, J. G., and Ramasamy, M. “Fluid Dynamics of Interacting Blade Tip Vortices With a Ground Plane,” Proceedings of the 64th Annual Forum of the American Helicopter Society, Montréal, Canada, April 29–May 1, 2008.

- [33] Ananthan, S., Leishman, J. G., “Role of Filament Strain in the Free-Vortex Modeling of Rotor Wakes,” *Journal of the American Helicopter Society*, Vol. 49, (2), April, 2009, pp. 176–191.
- [34] Ramasamy, M., and Leishman, J. G., “The Interdependence of Straining and Viscous Diffusion Effects on Vorticity in Rotor Flow Fields,” American Helicopter Society 59th Annual National Forum Phoenix, Arizona, May 6–8, 2003.
- [35] Ramasamy, M., Johnson, B., and Leishman, J. G., “Understanding the Aerodynamic Efficiency of a Hovering Micro-Rotor,” *Journal of American Helicopter Society*, Vol. 53, (4), October, 2008, pp. 412–428.
- [36] Ramasamy, M., Leishman, J. G., and Lee, T. E., “Flow Field of a Rotating Wing MAV,” *Journal of Aircraft*, Vol. 44, (4), pp. 1236–1244, July 2007.
- [37] Willert, C. E., and Gharib, M., “Digital Particle Image Velocimetry,” *Experiments in Fluids*, Vol. 10, (4), January, 1991, pp. 181–193.
- [38] Huang, H., Dabiri, D., and Gharib, M., “On Errors of Digital Particle Image Velocimetry,” *Measurement Science and Technology*, Vol. 8, (12), December, 1997, pp. 1427–1440.
- [39] Adrian, R. J., “Particle-Imaging Techniques For Experimental Fluid Mechanics,” *Annual Review of Fluid Mechanics*, Vol. 23, 1991, pp. 261–304.
- [40] Keane, R. D., and Adrian, R. J., “Optimization of Particle Image Velocimeters. Part I: Double Pulsed Systems,” *Measurement Science and Technology*, Vol. 1, (11), November, 1990, pp. 1202–1215.
- [41] Keane R. D., and Adrian, R. J., “Theory of Cross-correlation Analysis of PIV images,” *Applied Scientific Research*, Vol. 49, (3), July, 1992, pp. 191–215.
- [42] Westerweel, J., “Fundamentals of Digital Particle Image Velocimetry,” *Measurement Science and Technology*, Vol. 8, (12), December, 1997, pp. 1379–1392.
- [43] Leishman, J. G., “Seed Particle Dynamics in Tip Vortex Flows,” *Journal of Aircraft*, Vol. 33, (4), pp. 823–825.

- [44] Ramasamy, M., and Leishman, J. G., “Benchmarking Particle Image Velocimetry with Laser Doppler Velocimetry for Rotor Wake Measurements,” *AIAA Journal*, Vol. 45, (11), November, 2007, pp. 2622–2633.
- [45] Ramasamy, M., Johnson, B., Huismann, T., and Leishman, J. G., “DPIV Measurements of Tip Vortex Characteristics Using an Improved Aperiodicity Correction,” *Journal of American Helicopter Society*, Vol. 54, (1), January, 2009, 012004.
- [46] Theunissen, R., Scarano, F., Riethmuller, M. L., “On Improvement of PIV Image Interrogation Near Stationary Interfaces,” *Experiments in Fluids*, Vol. 45, (4), October, 2008, pp. 557–572.
- [47] Leishman, J. G., “Measurements of the Aperiodic Wake of a Hovering Rotor,” *Experiments in Fluids*, Vol. 25, (4), September, 1998, pp. 352–361.
- [48] Bhagwat, M., and Leishman, J.G., “Stability Analysis of Helicopter Rotor Wakes in Axial Flight,” *Journal of the American Helicopter Society*, Vol. 45, (3), July, 2000, pp. 165–178.
- [49] Tangler, J. L., Wohlfeld, R. M., and Miley, S. J., “An Experimental Investigation of Vortex Stability, Tip Shapes, Compressibility, and Noise for Hovering Model Rotors,” NASA CR-2305, 1973.
- [50] Kiger, K., and Pan, C., “PIV Technique for the Simultaneous Measurement of Dilute Two-Phase Flows,” *Journal of Fluids Engineering*, Vol. 122, December, 2000, pp 811–818.
- [51] Anderson, S., and Longmire, E., “Interpretation of Autocorrelation PIV Measurements in Complex Particle-Laden Flows,” *Experiments in Fluids*, Vol. 20, (4), pp. 314–317.
- [52] Paris, A., and Eaton, J., “Measuring Velocity Gradients in a Particle-Laden Channel Flow” Proceedings of the Third International Workshop on Particle Image Velocimetry, September 16–18, 2000, Santa Barbara, CA, pp. 513–518.
- [53] Gui, L., Lindken, R., and Merzkirch, W., “Phase-Separated PIV Measurements of the Flow Around Systems of Bubbles Rising in Water,” Proceedings of the ASME Fluids Engineering Division Summer Conference, June 22–26, 1997, Vancouver, Canada.

- [54] Khalitov, D. A., Longmire, E. K., “Simultaneous Two-phase PIV by Two-parameter Phase Discrimination,” *Experiments in Fluids*, Vol. 32, (2), February, 2002, pp. 252–268.
- [55] Lindken, R., and Merzkirch, W., “A Novel PIV Technique for Measurements in Multi-Phase Flows and its Application to Two-Phase Bubbly Flows,” 4th International Symposium on Particle Image Velocimetry, Göttingen, Germany, September 17–19, 2001.
- [56] Harvey, J. K., and Perry, F. J., “Flowfield Produced by Trailing Vortices in the Vicinity of the Ground,” *AIAA Journal*, Vol. 9, (8), August 1971, pp. 1659–1660.
- [57] Tooby, P. F., Wick, G. L., and Isaacs, J. D., “The Motion of a Small Sphere in a Rotating Velocity Field: A Possible Mechanism for Suspending Particles in Turbulence,” *Journal of Geophysical Research*, Vol. 82, (15), May, 1977, pp. 2096–2100.
- [58] Nielsen, P., “On the Motion of Suspended Sand Particles,” *Journal of Geophysical Research*, Vol. 89, (C1), January, 1984, pp. 616–626.
- [59] Nielsen, P., “Turbulence Effects on the Settling of Suspended Particles,” *Journal of Sedimentary Petrology*, Vol. 63, (5), September, 1993, pp. 835–838.
- [60] Butterfield, G. R., “Transitional Behaviour of Saltation: Wind Tunnel Observations of Unsteady Winds,” *Journal of Arid Environments*, Vol. 39, (3), July 1998, pp. 377–394.
- [61] Shao, Y., and Raupach, M. R., “The Overshoot and Equilibrium of Saltation,” *Journal of Geophysical Research*, Vol. 97, (D18), pp. 20,559–20,564.
- [62] Jakobsen, M. L., Easson, W. J., Greated, C. A., and Glass, D. H., “Particle Image Velocimetry: Simultaneous Two-Phase Flow Measurements,” *Measurement Science and Technology*, Vol. 7, (9), pp. 1270–1280.
- [63] Wereley, S. T., Gui, L., and Meinhart, C. D., “Advanced Algorithms for Microscale Particle Image Velocimetry,” *AIAA Journal*, Vol. 40, (6), pp. 1047–1055, June, 2002.
- [64] Westerweel, J., Dabiri, D., and Gharib, M., “The Effect of a Discrete Window Offset on the Accuracy of Cross-correlation Analysis of Digital PIV Recordings,” *Experiments in Fluids*, Vol. 23, 1997, pp. 20–28.

- [65] Ronneberger, O., Raffal, M., and Kompenhans, J., “Advanced Evaluation Algorithm for Standard and Dual Plane Particle Image Velocimetry,” Proceedings of the 9th International Symposium on Applications of Laser Techniques to Fluid Mechanics, Lisbon, Portugal, July 13–16, 1998.
- [66] Usera, G., Vernet, A., and Ferré, J. A., “Considerations and Improvements of the Analyzing Algorithms Used for Time Resolved PIV of Wall Bounded Flows,” Proceedings of the 12th International Symposium on Applications of Laser Techniques to Fluid Mechanics, Lisbon, Portugal, July 11–15, 2004.
- [67] Scarano, F., “Iterative Image Deformation Methods in PIV,” *Measurement Science and Technology*, Vol. 13, 2002, pp. R1–R19.